Two-Dimensional Materials and their Biomedical Applications

By

Yuchen Zhang

Dissertation
Submitted to the Faculty of the
Graduate School of Vanderbilt University
in partial fulfillment of the requirements
for the degree of

DOCTOR OF PHILOSOPHY

in

Electrical Engineering

June 30, 2021

Nashville, Tennessee

Committee Members:

Yaqiong Xu, Ph.D.

Daniel M. Fleetwood, Ph.D.

Ronald D. Schrimpf, Ph.D.

Deyu Li, Ph.D.

Sharon Weiss, Ph.D.

To my beloved family

ACKNOWLEDGEMENTS

I would like to express my deepest appreciation to my advisor Dr. Yaqiong Xu for her continuous guidance through my Ph.D. studies. Her skills, thinking, and creative ideas have always inspired me in my research and also life. I would also like to express my sincere gratitude to Dr. Deyu Li, Dr. Rebecca M. Sappington, Dr. Chengwen Zhou, who instructed me to complete many interdisciplinary projects. Further, I would like to thank my Ph.D. committee: Dr. Daniel Fleetwood, Dr. Ronald Schrimpf, Dr. Sharon Weiss for taking the time on advising me on my research, dissertation, and career.

I also like to thank my fellow and past group members of Dr. Xu's Lab, who contributed to my experimental work, engaged in inspiring discussions, and brought joy to our lab. Dr. Tu Hong, thanks for your patience to teach me various skills in lab and life here. Dr. Rui Wang, thank you for your great food and all kinds of suggestions. Dr. Tianjiao Wang, thanks for the time spending in the lab and traveling together. Thayer S. Walmsley, thanks for your continuous help and your wife's wonderful cookies. Xuyi Luo, Xiaosi Zhang, Christian D. Ornelas, Xuanyang Ge, whose friendship I enjoyed very much.

I would also like to thank my collaborators. Dr. Kirsten H. Dodson, Dr. Rachel Fischer, Dr. Michael L. Risner, who teamed together on retina projects. Dr. Lijie Yang, Dr. Mingjian Shi, who worked with me on the neuron project. In addition, I would like to express my gratitude to the staff members of Vanderbilt Institute of Nanoscale Science and Engineering: Dr. Bo Choi, Dr. Ben Schemidt, Dr. Dmitry Koktysh, Dr. Anthony Hmelo, Dr. Alice Leach, Dr. William Martinez, and Kurt Heinrich.

Finally, great thanks to my family and friends. My mom and dad always stand by my side and encourage me to chase my dream. My friend Chenbo Feng helped me a lot in my life here. Mengya Li, Lin Yang, Yang Zhao were very supportive of my studies here. Thanks to many other friends here at Vanderbilt, from college, or met on other occasions.

Table of Contents

Page

LIST OF TABLES

Page

LIST OF FIGURES

Chapter 1 Introduction to Two-Dimensional Materials

1.1 Two-Dimensional Materials

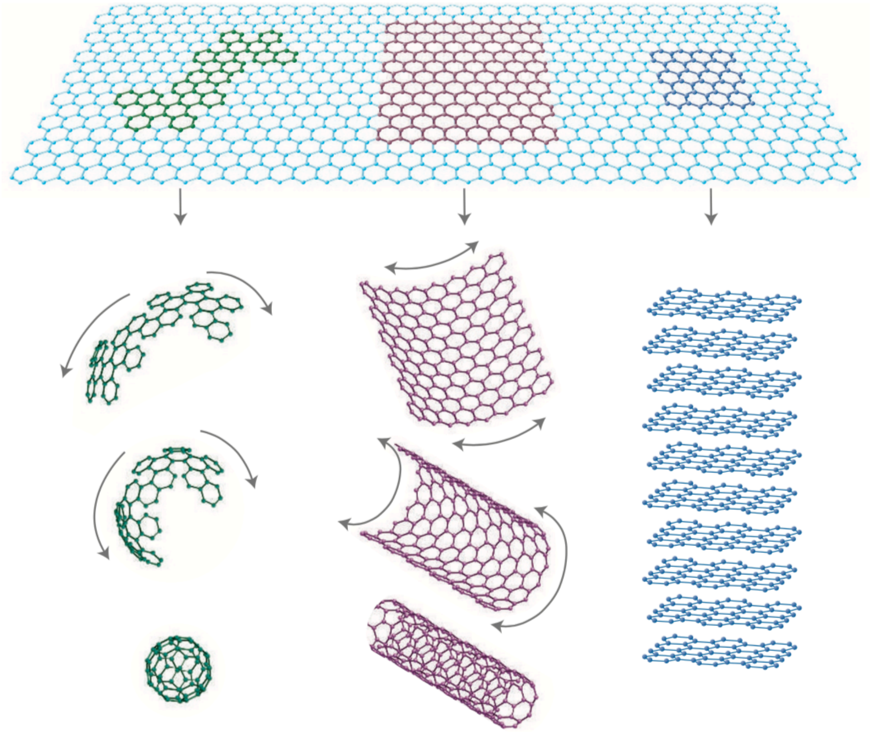

Figure 1.1 Mother of all graphitic forms. Graphene is a 2D building material for carbon materials of all other dimensionalities. It can be wrapped up into 0D buckyballs, rolled into 1D nanotubes or stacked into 3D graphite.[1]

Two-dimensional (2D) materials are a group of materials with thickness down to atomic scale. The successful exfoliation of graphene in 2004 started the era of 2D materials.[1] Studies of graphene demonstrated amounts of unique properties, and researchers have verified its unique properties and potentials in mechanical, thermal, electronics, and optoelectronics application.

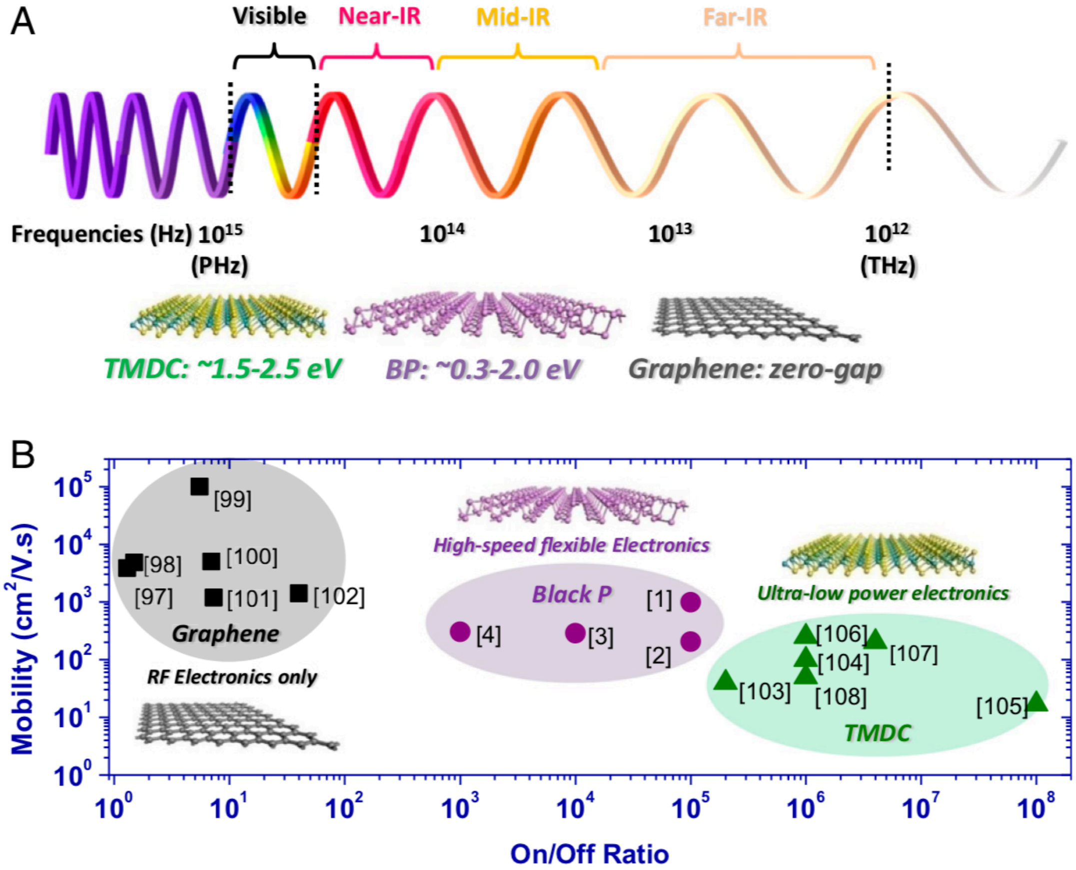

Figure 1.2 Electromagnetic wave spectrum and mobility/on–off ratio spectrum. (A) The electromagnetic wave spectrum and the band gap ranges of various types of 2D materials. The frequency ranges corresponding to the band gaps of 2D materials and their applications in optoelectronics are also indicated. (B) the "electronics spectrum," i.e., the mobility/on–off ratio spectrum, of nanomaterials with corresponding performance regions indicated for graphene (black squares and gray shaded area), black P (purple dots and light purple shaded area), and TMD [MoS_2, WSe_2, and WS_2] (green triangles and light green shaded area) transistors. The dots correspond to data from specific references indicated next to them. The shaded regions are the approximate possible ranges of performance reported for the respective materials in the literature.[2]

Graphene, as a representative material of them, is one atom thick sp^2 hybridized carbon sheet, with extremely strong mechanical strength and excellent conductivity, which can be regarded as the building block of many carbon materials, such as carbon nanotubes, fullerenes, and graphite (Figure 1.1). The extraordinary properties (carrier mobility: 2×10^5 cm^2/Vs, tensile strength: 125 GPa, elastic modulus: 1.1 TPa, thermal conductivity: up to 5000 W/mK) and stability make it applicable in widely extreme conditions for application in but not limited to electronics, biosensor, drug delivery, energy, water treatment, and advanced polymer composite.[3] Monolayer graphene has zero bandgap with six highly symmetrical K points in the corner of the Brillion zone. The energy and momentum have a linear relation at the Dirac point where is the contact point of the conduction band and valence band, which indicates zero effective mass of carriers. Under strain, extremely high pressure, or doping, researchers can adjust the bandgap of graphene.[4, 5] Recently, the magic angle of the moiré pattern has made graphene a wonder material again. Stacking two monolayer graphene with a twisted angle of 1.1^o, researchers observed tunable zero-resistance states with a critical temperature T_c up to 1.7 K, which initiated the study of twisted bilayer 2D materials.[6]

From these prominent discoveries of graphene, researchers are encouraged to restudy other 2D materials[7-12]. One of the most popular 2D materials group is transition metal dichalcogenides (TMD) with a bandgap around 2 eV, e.g., MoS_2, WSe_2. The various configuration of the TMDs brings a wide range of electrical and optical properties[13, 14]. With reduced layers, some TMDs tend to transform from indirect to direct bandgap materials with increased band gaps.[15] For instance, WSe_2 has a direct bandgap (~1.7 eV) in the monolayer form, and gradually decreases with increased thickness.[16, 17] Moreover, recent studies have shown that the strong spin-orbit interactions in TMDs lead to a giant split of the valence band that in turn allows for valley-selective excitation at the K and K’ points,[18-20] which are located at the corners of the hexagonal Brillouin zone. For single- and bi-layer WSe_2, the optical transition at the K and K’ points can only be excited by the right-handed circularly-polarized light $\sigma +$ and left-handed circularly-polarized light $\sigma -$, respectively. Furthermore, the valley-induced emission peaks in TMDs can be modulated by either an external electric field or environment temperature.[21-23] The former is likely due to the quantum-confined Stark effect, a fundamental phenomenon for low-dimensional materials.[24] The latter may result from the temperature-dependent nature of TMDs bandgap. Black phosphorus (black P) is another rediscovered material, which bridges the gap between graphene and TMDs. Monolayer black P has a direct bandgap of ~2 eV, and gradually decreases to ~0.3 eV with increased layer number.[25]

1.2 Materials synthesis

Top-down and bottom-up are two groups of methods to obtain graphene. Micromechanical exfoliation is widely used for the fabrication of high-quality devices for proof of concept in a laboratory with low yield.[26] It’s also the first time how researchers obtained graphene with a simple scotch tape. However, the size of the resulted material is normally tens of micrometers and sparse. Liquid-phase exfoliation of graphite produces single to few layers of graphene of nano- to micrometer-sized sheets, however, the quality of the resulting graphene is hindered during the process.[27] Although different surfactants or ions were added to the exfoliation, removing those chemicals is quite challenging. Chemical vapor deposition (CVD) is a typical bottom-up method for 2D materials growth. Using methane as the carbon source, with sophisticated operation setup and parameter control, wafer-scale monolayer graphene can be synthesized with high quality and low defects. Copper is a typical substrate for graphene CVD. The solubility of C in Cu is extremely low, and Cu acts as a catalyst for decomposing of C containing gas, such as methane. This method is ideal for large-scale synthesis. The drawback is the resulted materials are on metal surfaces, which will need further procedures to transfer on target substrates in the application and may affect the graphene quality.

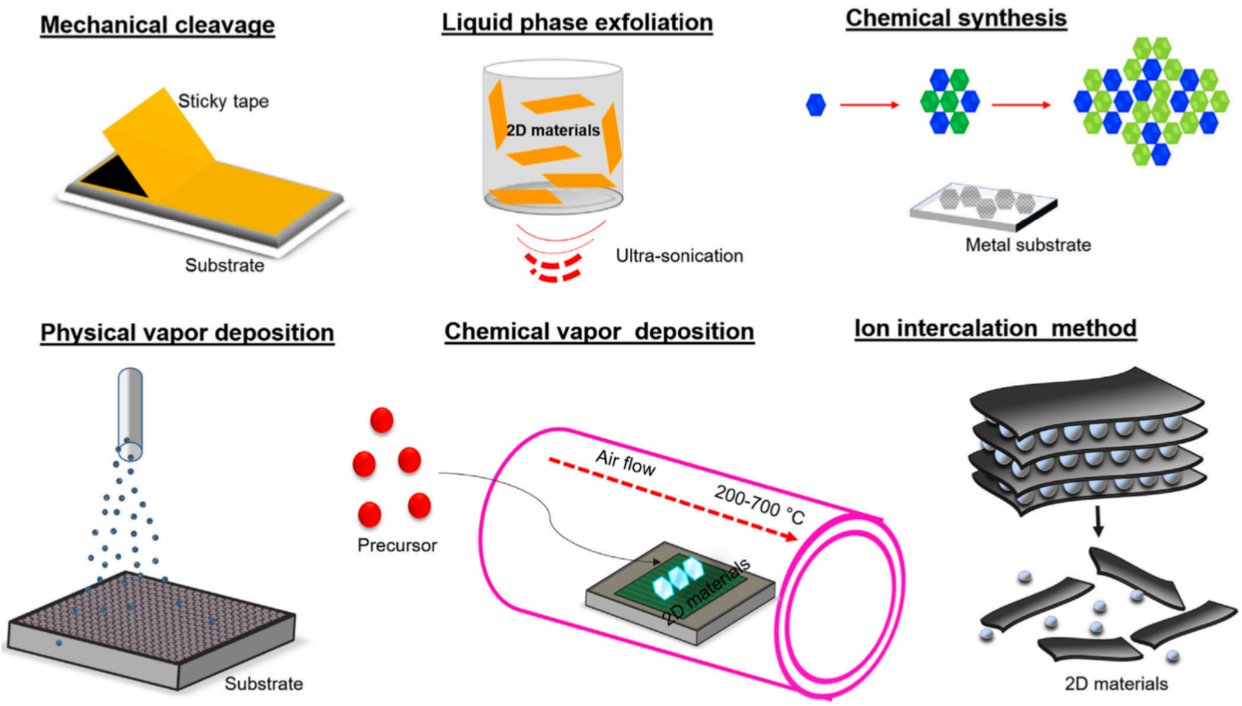

Figure 1.3 Various top-down and bottom-up approaches used for the synthesis of 2D materials.[28]

Similar to graphene, for top-down methods, micro-mechanical exfoliation of atomic thick TMDCs from the bulk material is the most common method for high-quality electronic property device fabrication for proof of concept with a low yield. Liquid-phase exfoliation is a high yield production of thin nanosheets of TMDs via ultrasonication of a liquid sample with the bulk crystals. However, the electrical properties are lower than micro-mechanical exfoliation. Intercalation-assisted exfoliation is an effective method with chemicals insertion into the interlayer for expanding the interlayer distance.[29] Destructive thinning and etching methods are using laser or other tools for thinning the thick flakes to target thickness, which are also capable of a designed pattern for functional devices. Bottom-up methods, such as CVD or physical vapor transport (PVT) techniques, require very precise control on the growth parameters for scalable size demand, which has a relatively high yield comparing to micro-mechanical exfoliation, but the electrical properties are lower.

1.3 Application of 2D materials

As the zero-bandgap nature of graphene makes it difficult for transistor application on the digital switch, various fields have seen graphene as promising candidate material. For electronics, the excellent carrier mobility and conductivity make graphene a great material for fast analog electronics, radio-frequency (RF) transistors. Completely switch off is not vital for these devices. The cut-off frequency f_T is the key metric for RF transistors, which is the frequency at which the current gain becomes one when the drain is short-circuited to the source. For an ideal RF device, $f_T = \frac{g_m}{2\pi C}$, where $g_m \left(g_m = \frac{dI}{dV_g}\right)$ and C are the dc transconductance and capacitance of the device, respectively. SiC-based graphene field-effect transistors (FET) have reached f_T more than 300 GHz with 40 nm channel lengths. Studies have shown the constant performance of graphene FETs on diamond-like carbon substrate from 300 K down to 4 K, which demonstrates the potential application in extreme environments. Without bandgap, graphene is ideal for broadband photon detection but has an apparent dark current. With the presence of a field gradient, the photoexcited electron-hole pairs will produce photocurrent under light excitation, which is a basic idea for its optoelectronic applications.

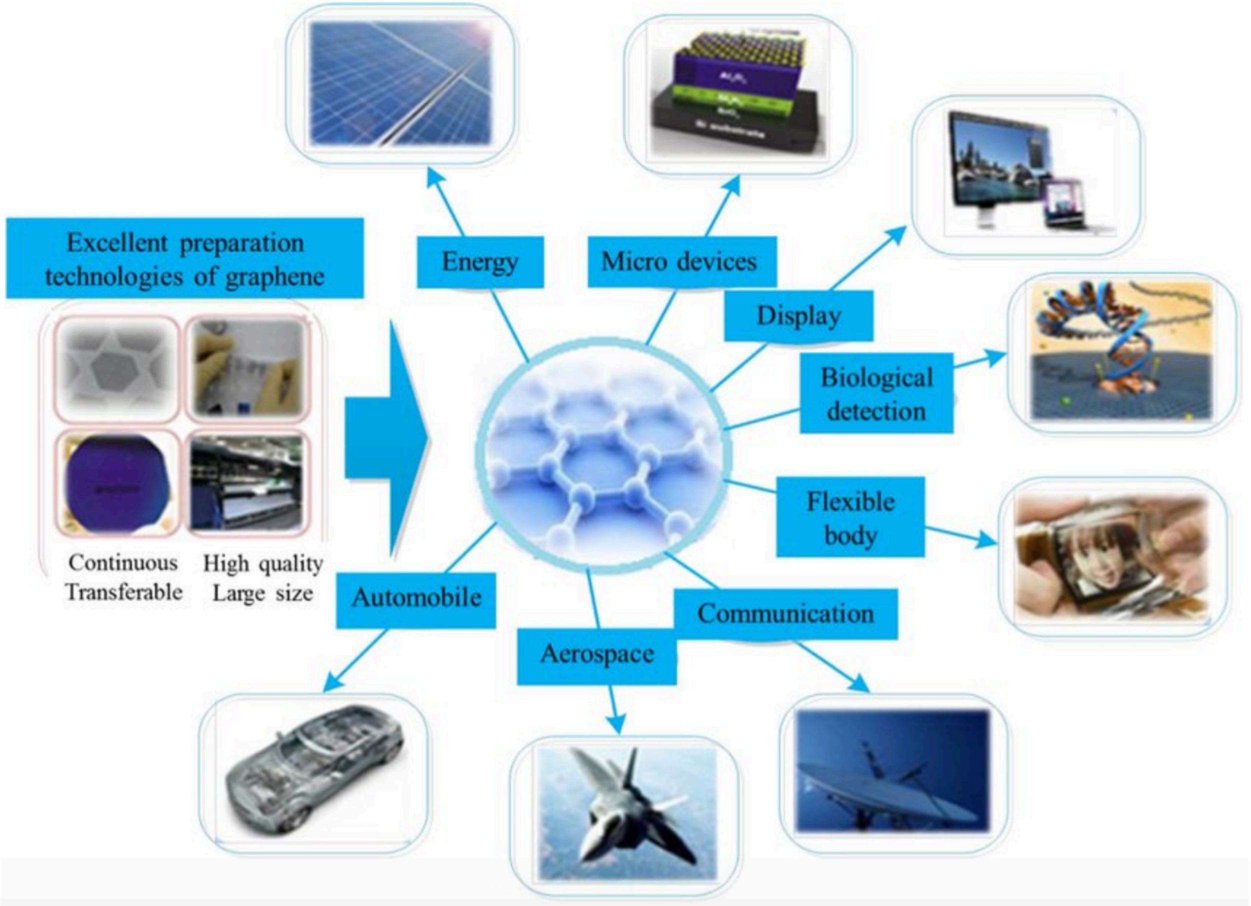

Figure 1.4 Applications of graphene in industrial production.[30]

For mechanical application, researchers demonstrated that graphene-based thermophones are able to generate audible and ultrasound sound frequencies via thermoacoustic effect. As the AC current is applied to the device, a temperature oscillation in graphene causes density and pressure oscillation in the air.[31] Various piezoresistive sensors were developed to detect strain and pressure with suspended graphene or graphene composite.[32, 33] Many groups also make filters with graphene for desalination or gas separation.[34, 35] To adjust the pores on graphene for different selectivity, surface assisted coating, electron beam irradiation or ion bombardment can be applied.[36-38]

Extremely high surface-to-volume ratio, electron mobility, flexibility make it ideal materials for biomedical applications.[39] Inspired by carbon nanotube, graphene was also explored for drug delivery, as its planar sp^2 hybridized carbon and physiological solubility and stability.[40] Drugs can be loaded via chemical conjugation or physisorption approaches. Graphene FET can be used for biosensing charged molecules based on the biorecognition events between molecules at the gate of FET, which will modulate the carrier density at the locations of the events and change the conductivity between the source and drain. Alternatively, combining with scanning photocurrent microscopy, the local photocurrent response can show spatiotemporal information of biological events, which changed the local graphene band structure, as I will demonstrate in Chapter 4. Researchers also demonstrate graphene FET for DNA hybridization and ssDNA detection.[41, 42] Graphene, served as cell culture substrate, showed potential for tissue engineering to repair tissue function and promote cell growth as I will show in chapter 4.[43]

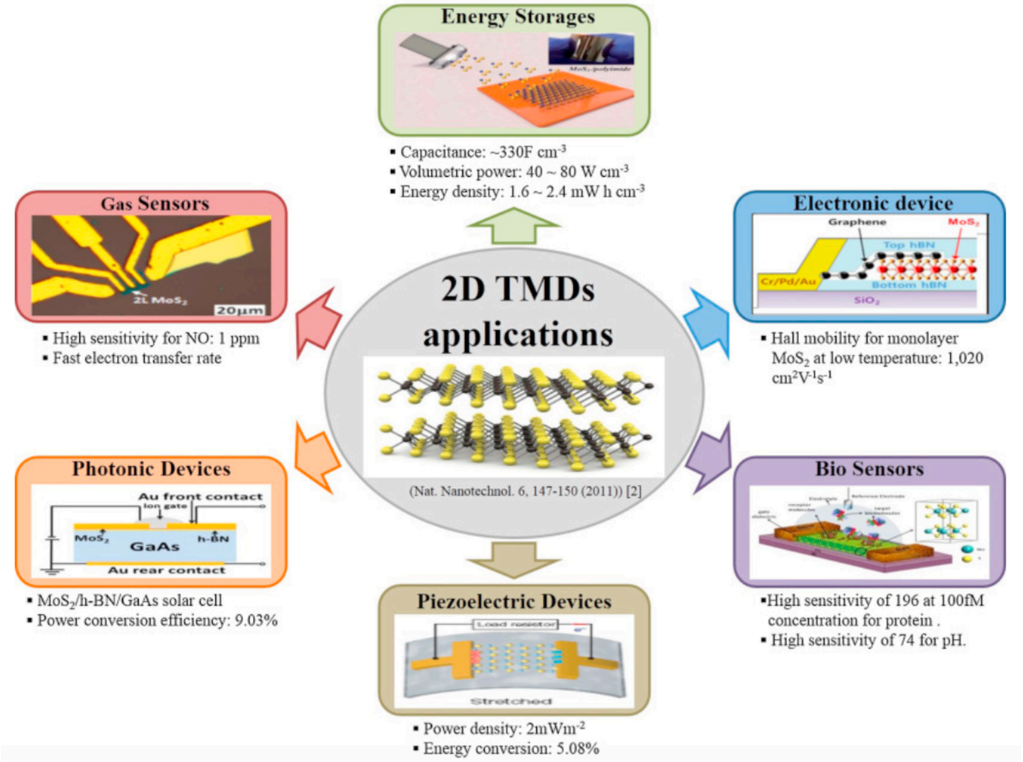

Figure 1.5 Electronic, opto-electronic and energy devices based on 2D TMDs.[44]

TMDs with a bandgap around 2 eV, for example, MoS_2 with a direct bandgap (~ 1.8 eV), high on/off ratio of ~10^8, have shown excellent performance in FET and photodetectors.[45, 46] For energy application, TMDs was studied on the potential as Dye-sensitized solar cells, which are renewable energy devices, with a power conversion efficiency 7.35%, comparable to conventional Pt-based devices.[47] Due to their similar structure with graphite, TMDs attract extensive attention in the field of supercapacitors.[48] With a flexible structure of the few-layer TMDs, flexible electronics based on piezoelectric effect have been demonstrated for energy harvesting and motion/strain sensor.[48, 49] In biomedical applications, TMDs are studied on drug delivery carriers. Some TMDs are ideal materials for photothermal treatment, combing with drug delivery, researchers can control the release with NIR radiation.[50] Using as contrast agents for X-ray computed tomographic imaging, they show better performance than graphene-based agents.[51, 52]

TMDs can also be applied for biosensors, such as DNA or protein detections, in a FET configuration.[53] When the decorated antigens on TMDs surface interact with the target molecules, real-time conductance change can be recorded with sub-picomolar sensitivity.[54]

Chapter 2 2D Materials Synthesis and Devices

2.1 Material synthesis

As introduced in chapter 1, graphene synthesis includes many approaches. Here, I will descript in detail about 2D materials synthesis in my research.

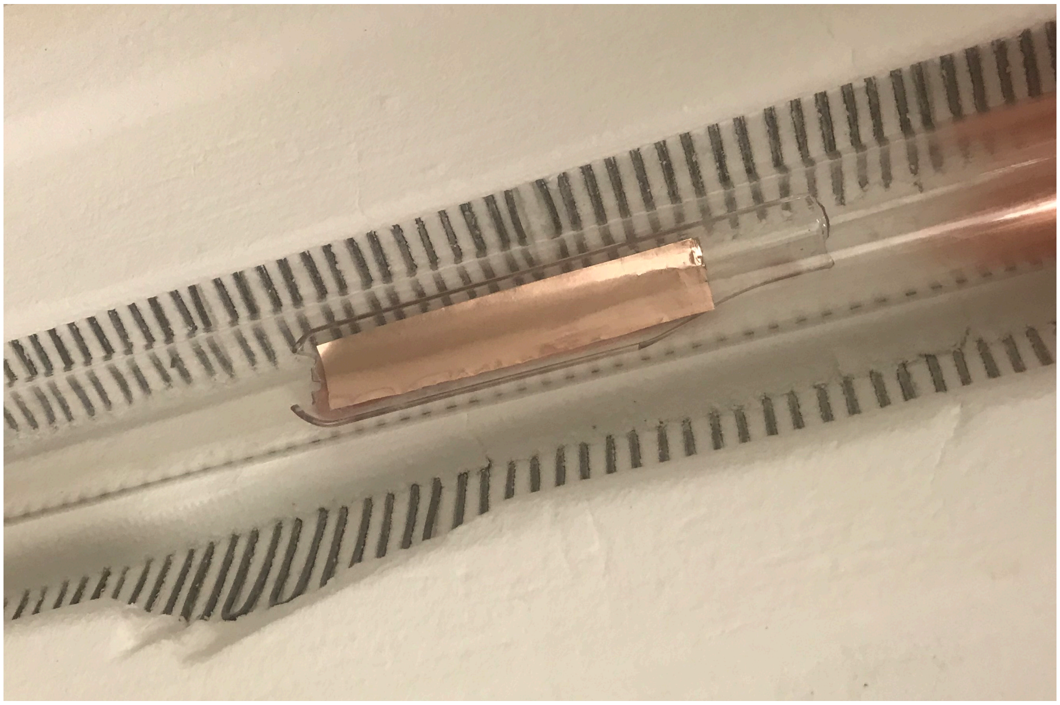

Figure 2.1 CVD graphene growth on Cu foil in a tube furnace.

I adopt a standard CVD approach with modification according to our lab and my experience.[55] A piece of copper foil (Alfa Aesar, 0.025mm, 99.8%) was pretreated in 5% nitric acid bath for 10 min and then cleaned by deionized water baths, followed with nitrogen blow dry. The copper foil was then loaded into a tube furnace. Safety is the top issue in the lab, always check the sealing of the tube furnace before start growth. After annealing with 100 sccm of hydrogen at

1000 °C for 1 h, the hydrogen flow was reduced to 80 sccm with 20 sccm of methane introduced. After 30 min, all the flammable gas and furnace are off, 200 sccm argon was introduced during cooling down. A successful synthesis can be seen from the uniform shining coating of graphene on copper comparing to the bare copper foil.

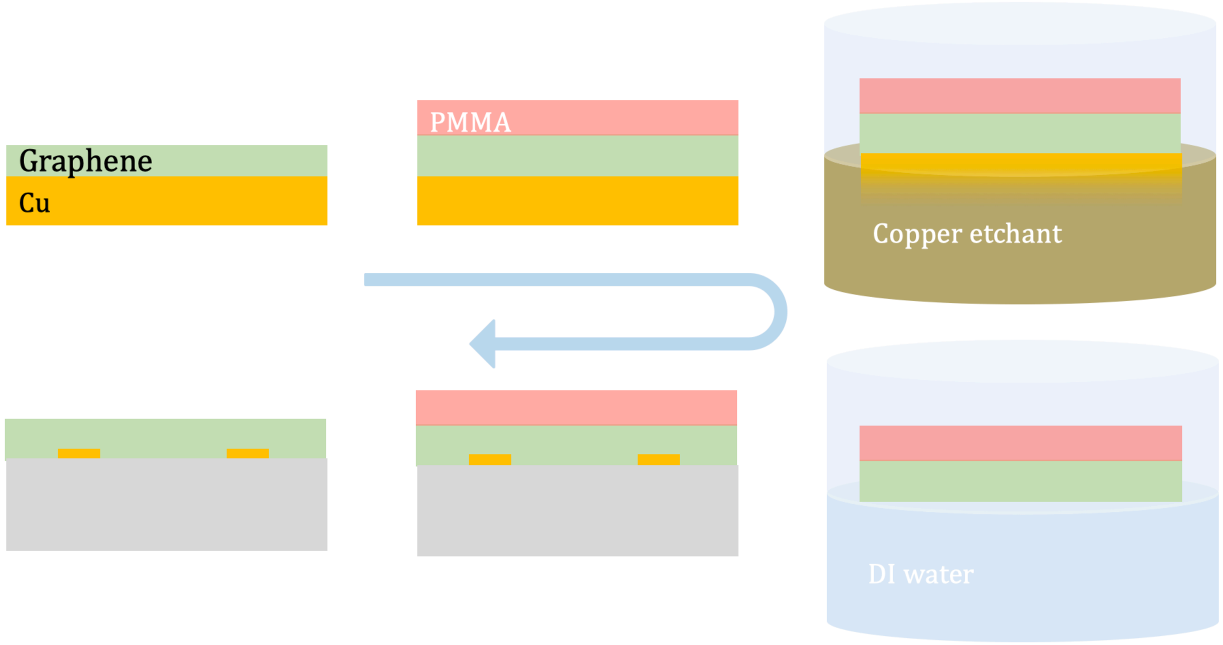

Figure 2.2 Schematic diagram of graphene transfer process.

After CVD, copper foil is coated with graphene, which will be transferred to a target substrate for characterization and measurement. The wet transfer method is the typical approach. A poly-methyl methacrylate (PMMA) layer was spin-coated on top of the copper foil to hold the graphene film. The PMMA-graphene film was separated from the copper foil through a wet etching process in copper etchant solution, and then fished onto a target substrate three times with DI water bath. Then, PMMA can be removed with Acetone after PMMA-graphene completely dry on the substrate. An alternative method to separate graphene from copper is using the electrolysis approach.[56] Generally, PMMA-graphene-copper acted as a cathode of an electrolytic cell with 0.25

M NaOH in deionized water and a platinum wire used as the anode. Supplying a small voltage of around 3.3V, the current will be a few milliamperes for a gentle reaction. Gradually dipping the PMMA-graphene-copper deeper into the solution, PMMA-graphene will be easily separated. Here, maintaining a low power is critical to get high-quality graphene. Otherwise, the H_2 bubbling will have a destructive impact on graphene structure and induce many defects.

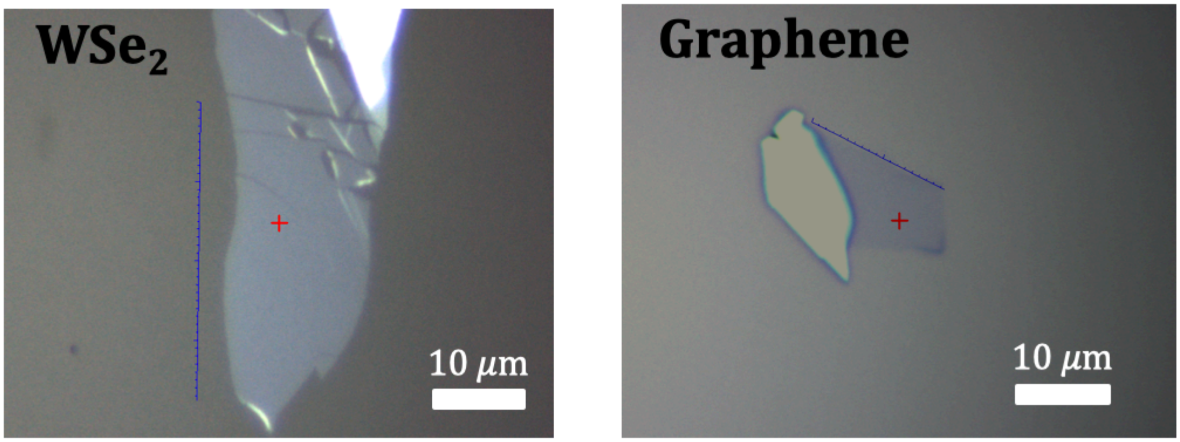

Figure 2.3 Optical micrograph of WSe_2 and graphene flakes from micro-mechanical exfoliation.

I also applied micro-mechanical exfoliation was used to get graphene and few-layer WSe_2 flakes. A degenerately-doped silicon substrate covered with a 300 nm thick thermally-grown SiO_2 layer was first treated by oxygen plasma for 10 min. Subsequently, the substrate was bath sonicated in acetone and then isopropyl alcohol for about 5 min. After that, the substrate was rinsed with deionized water. The typical procedure is first using a clean tape A to attach a piece of bulk material and gently cleave off, which will be the source tape for further cleavage. Take another tape B to attached to tape A and peel off. Fold and unfold tape B a few times and attach it to a cleaned wafer. Gently touch the tape to make the best contact between the wafer and tape. Then slowly peel the tape off from the wafer. The general procedure is similar in graphene or WSe_2 exfoliation. After exfoliation, it takes much time and patient to check the wafer very carefully under a microscope.

Practicing with graphene is better to get the feeling for exfoliation. Figure 2.3 shows the resulted flakes of WSe_2 and graphene.

I utilized liquid phase exfoliation for graphene synthesis for high yield synthesis. After putting graphite and N-methylpyrrolidone (NMP) in a glass vial and 60 h bath sonication, keep it still overnight and check if aggregation happens. Adjust the sonication process to avoid aggregation. A dark liquid can be obtained after mild centrifugation as shown in Figure 2.4.

Figure 2.4 Liquid exfoliated graphene in NMP.

2.2 Graphene characterization and device fabrication

Raman spectroscopy is a powerful tool for material characterization and is widely applied in 2D materials studies. A typical graphene spectrum was shown in Figure 2.5a after transfer on a coverslip. 2D peak has a symmetric shape and the 2D-to-G intensity ratio is about 2, indicating that the graphene has a monolayer structure.[57] To verify a uniform graphene coating, Raman mapping can provide spatially resolved information of material distribution. The equipment will automatically scan the selected area with desired step and exposure parameters. Figure 2.6 shows graphene transferred on transparent coverslips, which is difficult to judge the graphene region from an optical microscope only. At the zoomed-in region, corresponding Raman mapping of the 2D peak intensity distribution help to confirm a uniform graphene coating. If I transfer graphene on

SiO_2/Si wafer, the graphene region will show a light purple color and easier to check graphene coverage.

Graphene transistors were fabricated on 170 µm-thick transparent coverslips. Electrodes were first defined by photolithography and deposited with 5 nm Ti and 40 nm Au. A cylinder was placed on top of graphene transistors and filled with 1X phosphate-buffered saline (PBS) solution. A gold wire was inserted into the cylinder and used as an electrolyte gate to modulate the electrochemical environment of graphene. Gate-dependent source-drain current measurement of a typical graphene transistor exhibits the ambipolar behavior with the Dirac point close to 0.89 V, displaying p-type characteristics at zero gate bias (Figure).

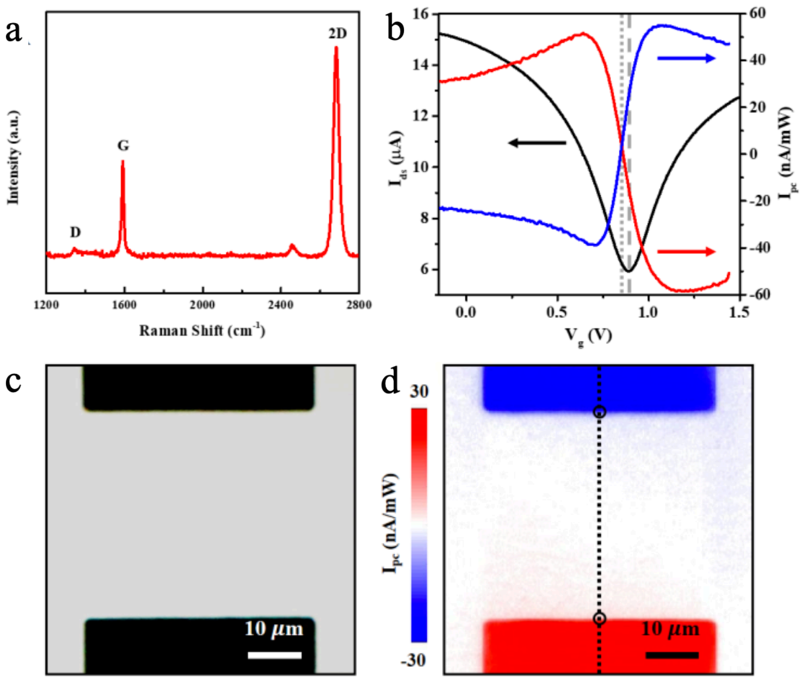

Figure 2.5 Characterization of a graphene device. (a) Raman spectrum of graphene on a transparent coverslip. (b) Electrical transport behavior (black curve, left) and photocurrent responses (red and blue curves, right) at the black circle regions of the graphene transistor in (d)

as a function of V_g. The grey dashed and dotted lines indicate $V_g = V_{Dirac}$ and $V_g = V_{FB}$, respectively. (c) Optical and (d) photocurrent images of a typical graphene transistor.

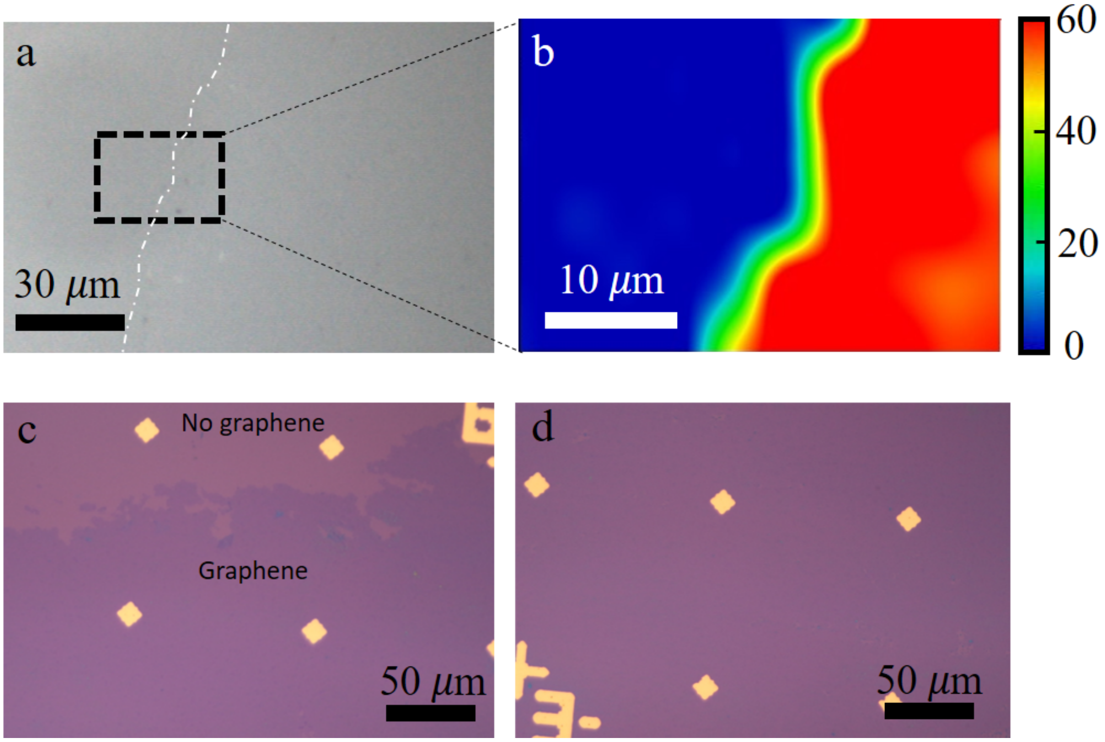

Figure 2.6 Optical images of graphene on top of (a) coverslip and (c, d) a SiO_2/Si wafer. (b) Raman mapping shows the 2D-peak intensity distribution in the black dashed line circled region in (a).

For studying the optoelectronic property, spatial-resolved scanning photocurrent microscopy is a powerful technique for exploring local electronic structures and charge transport in various devices. I build the setup with an Olympus microscope. A laser source (λ = 785 nm) was expanded and altered by nanometer-resolution scan mirrors. The laser beam was then focused by a 40 X objective (N.A. = 0.6) into a diffraction-limit spot (~ 1 μm) on a graphene transistor. Under 785 nm illumination, electron-hole pairs were generated in graphene and then separated by Schottky-like barriers at graphene-electrode junctions or by a local potential gradient along the graphene. Reflection images were simultaneously recorded by a silicon photodetector, which could be used to precisely locate the position of photocurrent responses. Figure 2.5c&d show typical optical and scanning photocurrent images of graphene transistor.

Since photocurrent signals are proportional to the local potential gradients, I can extract band diagrams ($E_F - E_{Dirac}$) of graphene through numerical integration of photocurrent profiles.[58, 59] Based on a simple capacitor model, the energetic difference has an expression $\Delta E = E_F - E_{Dirac} \approx \hbar v_F \sqrt{\pi n} = \hbar v_F \sqrt{\pi \frac{C}{e} \left| V_g - V_{Dirac} \right|}$, where $v_F \approx 10^6\ m/s$ is the Fermi velocity, n is the charge carrier concentration, and C is the electrostatic capacitance of graphene.[60] As shown in Figure 2.5b, the minimum current for the graphene transistor is observed to be $V_{Dirac} \sim 0.89\ V$, leading to $\Delta E\left(V_g = V_g^{Global} = 0\right) \approx 0.49\ eV$. Moreover, almost no photocurrent is observed for the flat band condition at $V_{FB} \sim 0.85\ V$. This allows us to estimate the constant energetic offset at the graphene-electrode contacts: $\phi_{FB} = \Delta E\left(V_g = V_{FB}\right) \approx 0.11\ eV$.

2.3 WSe$_2$ transistors fabrication and characterization

A schematic diagram of a WSe$_2$ transistor was shown in figure 2.7. To fabricate the WSe$_2$ transistors, WSe$_2$ flakes were mechanically exfoliated from WSe$_2$ crystals (from 2D Semiconductors) onto a Polydimethylsiloxane (PDMS) stamp. After carefully checking the stamps, I can locate the desired flakes and transfer them onto pre-cleaned SiO$_2$/Si substrates (Figure 2.8).

Optical microscopy, Raman spectroscopy, and atomic force microscopy (AFM) were utilized to characterize WSe$_2$ flakes. Figure 2.9 shows a typical Raman spectrum of monolayer WSe$_2$ flakes, where strong E_{2g}^{1} (251.2 cm^{-1}) and A_{1g} (263.5 cm^{-1}) modes of WSe$_2$ are detected. The peak near 308 cm^{-1} (B_{2g}^{1}) is not observed, which indicates this is a monolayer WSe$_2$ flake.[61] Finally, WSe$_2$ devices were fabricated via standard electron beam lithography (EBL) and subsequent electron beam deposition of 5/40 nm Cr/Au. Back-gate voltages can be applied through the 300 nm SiO_2 layer.

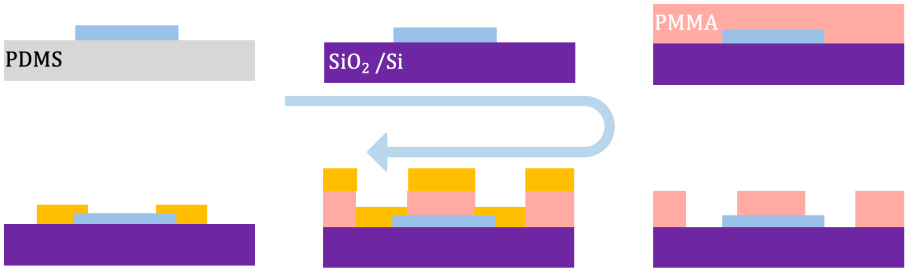

Figure 2.7 Schematic diagram of WSe_2 device fabrication process.

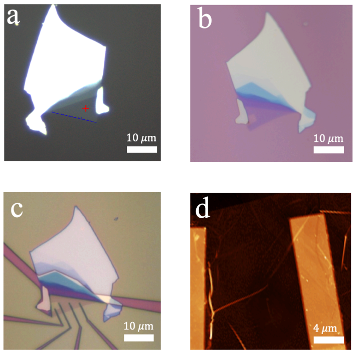

Figure 2.8 Optical micrograph of a WSe_2 flake (a) on PDMS, (b) transferred on SiO_2/Si wafer, (c) with EBL defined pattern and (d) AFM image.

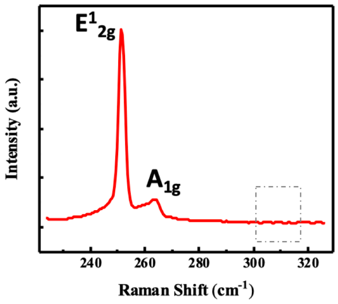

Figure 2.9 Raman spectrum of a monolayer WSe_2 flake on SiO_2/Si wafer.

Chapter 3 Anisotropic Photoresponse of WSe_2 Transistor

3.1 Introduction

As introduced in chapter 1, WSe_2 is a typical TMD material with a bandgap around 1.5 eV, which has shown unique electrical, optical and optoelectronic properties. Monolayer WSe_2 has a direct bandgap, with the band-edge located at the energy degenerate valleys (±K) at corners of the hexagonal Brillouin zone.[62] Considerable research has been devoted to the valley-dependent selection rule of single- and bi-layer TMDs in their photoluminescence studies, rather less attention has been paid to explore their polarized photocurrent generation mechanisms. Photocurrents generated by linearly-polarized light in conventional semiconductors have been studied for decades, where the optical momentum alignment effect is believed to play an important role in the polarization of photocurrent signals.[63, 64] For example, anisotropic momentum distribution of photo-induced carriers has been reported in GaAs under interband excitation measured by hot-electron photoluminescence, which mainly originates from the optical selection rules for heavy-hole and light-hole bands at the Γ point.[63] Recently, graphene and graphene-like gapped 2D Dirac materials are theoretically predicated to have a strongly anisotropic distribution of photo- excited carriers under linearly polarized excitation due to the pseudospin-induced optical transition selection rules. Therefore, it will be important to explore how linearly polarized excitation influences photocurrent generation in TMDs.

Here, I investigate the photocurrent generation mechanisms in WSe2 phototransistors under linearly polarized excitation.[65] When the photon energy is above the A exciton energy, the photocurrent signals at WSe2-metal junctions reach maximum if the incident light polarization is parallel to the metal electrode edge or perpendicular to the momentum direction of electrons. Such anisotropic distribution of photo-excited carriers is likely due to the pseudospin-induced optical transition selection rules. This is known as the optical momentum alignment effect in conventional semiconductors. When the photon energy is below the A exciton energy, the photocurrent intensity reduces significantly and reaches its maximum when the incident light polarization is perpendicular to the metal electrode edge, owing to hot electron injection induced by the surface plasmonic effect of gold electrodes. Moreover, I find that when an external electric field is applied, the photocurrent peak can be shifted due to the quantum con- fined Stark effect. I also demonstrate that the exciton energy can be modulated by the temperature since the band gap of WSe_2 depends on the temperature. To the best of our knowledge, it is the first time to demonstrate optical momentum alignment effect induced linearly polarized photocurrent response in WSe_2 phototransistors. These studies of the anisotropic photocurrent generation mechanisms help understanding the basic properties of TMDs and broaden the horizon for future TMD-based anisotropic optoelectronics.

3.2 WSe_2 transistors characterization

A schematic diagram of a WSe_2 transistors was shown in figure 3.1a. WSe_2 transistors were fabricated as descripted in chapter 2. Optical microscopy, Raman spectroscopy and AFM were used to characterize WSe_2 flakes. Figure 3.1b shows the Raman spectrum of few-layer WSe_2 flakes, where strong E_{2g}^1 (251.2 cm^{-1}) and A_{1g} (263.5 cm^{-1}) modes of WSe_2 are detected. A peak near 308 cm^{-1} (B_{2g}^1) is observed, which is a marker for multi-layer WSe_2.[61] Finally, WSe_2 devices were fabricated using standard EBL and subsequent electron beam deposition of 5/40 nm Cr/Au. The degenerately doped Si substrate was used as the back gate.

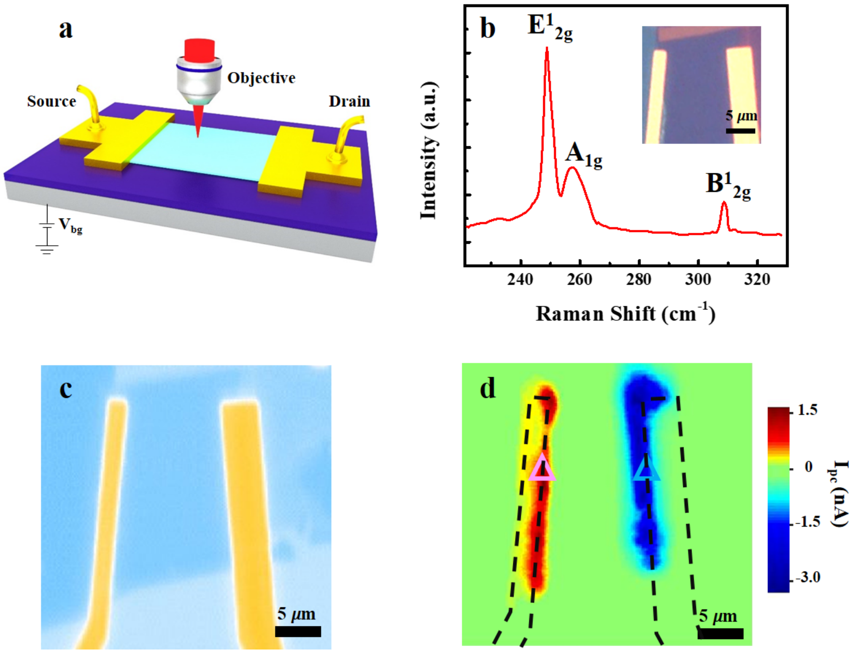

Figure 3.1 WSe_2 device measurement. (a) Schematic diagram of a scanning photocurrent measurement setup. (b) Raman spectrum of a few-layer WSe_2 flake on a SiO_2/Si substrate under 532 nm illumination. Inset: optical image of a WSe_2 phototransistor (c) Reflection and (d) photocurrent images of the few-layer WSe_2 transistor under 650 nm illumination with zero gate voltage. Black dashed lines outline the Au electrodes.

To explore the optoelectronic properties of WSe_2, I performed spatially resolved scanning photocurrent measurements in a Janis ST-500 microscopy cryostat under high vacuum (~10^{-6} Torr). A continuous-wave laser beam (NKT Photonics SuperK Supercontinuum Laser) was focused into a diffraction-limited spot (~1 μm) by a 40X Olympus objective (N.A. = 0.6). Its polarization direction was adjusted via a half-wave plate and the followed by a polarizer. A nanometer-resolution scan mirror was used to change its position. The photocurrent signals were collected by a preamplifier, while the reflection of the incident laser beam was measured by a Si photodetector to locate the position of the device. Figures 3.1c and 3.1d show the reflection and photocurrent images of a few-layer WSe_2 transistor at a zero drain-source bias under 650 nm illumination, respectively. Remarkable photocurrent responses are located at WSe_2-metal junctions, where the built-in electric field induced by Schottky barriers can separate photo-excited electron-hole pairs (EHPs) efficiently, leading to photocurrent signals.

3.3 Anisotropic photocurrent responses

To investigate photocurrent generation mechanisms, I performed wavelength-dependent photocurrent measurements. As shown in figure 3.2a, these is a photocurrent peak located around 755 nm (~1.64 eV), which is corresponding to the A exciton resonance for few-layer WSe_2.[66] I also find that when the photon energy is above the A exciton energy, the maximum photocurrent response appears when the light polarization direction is parallel to the metal electrode edge, suggesting that electrons in the valence band of WSe_2 prefer to absorb photons with the polarization direction perpendicular to their momentum direction. Such a linear polarization is similar to the optical momentum alignment effect in conventional semiconductors due to the spin-orbit interaction, where two twofold-degenerate subbands of heavy and light holes are in contact at the top of the valence band.[63] Photo-excited electrons from the heavy-hole subband show the momentum direction preferentially perpendicular to the light polarization direction, while those from the light-hole subband own the momentum direction mainly along the light polarization direction. Recently, graphene and graphene-like gapped 2D Dirac materials are theoretically predicted to exhibit similar behavior, owing to the pseudospin.[67] For WSe2, according to Fermi's Golden Rule, transition rate $W(\mathbf{k})$ for an electron with wave vector $\mathbf{k}$ with first-order time-dependent perturbation theory by

$$W(\mathbf{k}) = \frac{2\pi e^2 I_e}{chv^2} \left|\mathbf{P} \cdot \langle \Psi^c(\mathbf{k}) | \hat{\boldsymbol{v}} | \Psi^v(\mathbf{k}) \rangle\right|^2 \delta(E_c(\mathbf{k}) - E_v(\mathbf{k}) - hv),$$

where the Ψ^c and Ψ^v (E_c and E_v) are the wave functions (energies) of conduction and valence bands, respectively. **P** is the polarization vector of excitation light, which is parallel to the crystal's surface. $\hat{\boldsymbol{v}}$, I_e and v are the velocity operator, intensity and frequency of the incident light, respectively. Theoretical studies show that at low energy regime the angular generation density g is:

$$g = F_0(\varepsilon_0)\,[1 + \alpha_0 \cos(2\theta)\,],$$

where $\alpha_0 = \frac{E_g^2 - 4\varepsilon_0{}^2}{E_g^2 + 4\varepsilon_0{}^2}$ defines the degree of momentum alignment, θ is the angle between the momentum of the photoexcited electron and polarization of the incident light, $F_0(\varepsilon_0)$ is the total density of carriers created at energy ε_0 and subscript 0 means the no relaxation has occurred.[67] As illustrated in figure 3.2b, a linear polarized light is expected to generate an anisotropic distribution of photoexcited EHPs, where the momentum direction of carriers is preferentially perpendicular to the polarization direction of incident light. At WSe$_2$-metal junction the built-in electric field dissociating the generated exciton after excitation has the direction perpendicular to metal edge. When the excitation polarization parallel to the metal edge, the direction of the electron momentum is mostly perpendicular to the metal edge, which leads to stronger photocurrent response. Indeed, the pseudospin-related optical transition selection rules of WSe2 induce the optical momentum alignment effect. Therefore, when the incident light is polarized in the direction along the metal edge, the photo-excited EHPs have a momentum direction perpendicular to the metal edge, which can be dissociated by the built-in electric field at the WSe2-metal junction and thus induce photocurrent signals. In contrast, when the incident light direction is perpendicular to the metal edge, the momenta of photo-excited EHPs are along the metal edge or normal to the built-in electric field, leading to relatively weak photocurrent responses. I also fabricated monolayer WSe$_2$

transistors, as shown in figure 3.3. Typical Raman spectrum of WSe_2 shows no peak around 308 cm^{-1}, indicates the monolayer structure of the material. Apparent anisotropic photoresponse confirms the results from theoretical expectation.

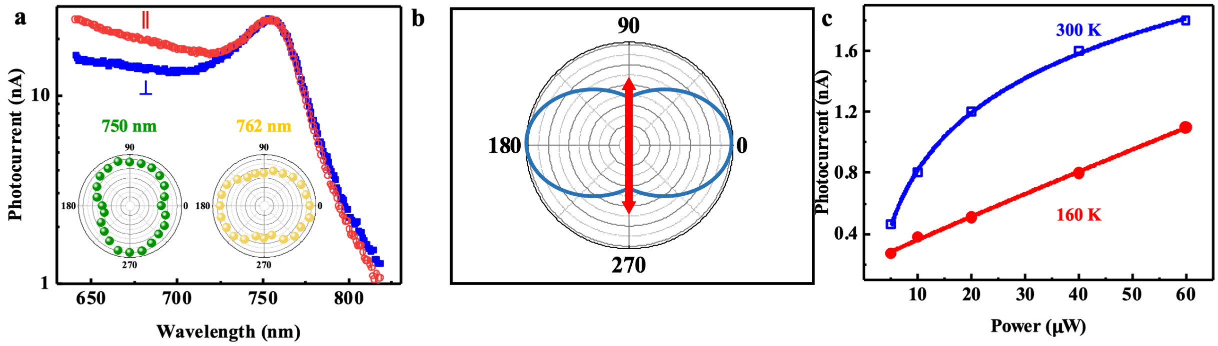

Figure 3.2 Anisotropic photoresponse of WSe_2. (a) Photocurrent spectra with linearly-polarized excitation at WSe_2-metal junctions under an out-of-plane voltage of 80 V. Inset: Normalized photocurrent intensity extracted from photocurrent images at WSe_2-metal junctions under 750 nm and 762 nm illumination, respectively. 0^o is perpendicular to electrodes. (b) Schematic diagram of the angular distribution function, Red arrow indicates the excitation light polarization direction. (c) The power dependence of the photocurrent response under 755 nm illumination at 160 K (red circle) and 300 K (blue square), respectively.

If the excitation photon energy is below the A exciton energy, the photocurrent signals are maximized when the incident light is polarized in the direction perpendicular to the electrode edge. These results suggest that a different photocurrent generation mechanism is involved for low energy photon excitation. When the photon energy is lower than the A exciton energy of WSe_2, the photon cannot provide enough energy to excite an electron from the valence band to the conduction band of WSe_2; therefore, the photocurrent signals are mainly attributed to the hot electron injection. Here, photons can be absorbed by gold electrodes to generate hot EHPs. The photo-excited hot electrons can cross over the Schottky barrier and be subsequently injected into the conduction band of WSe_2. The polarized photocurrent response primarily results from the anisotropic absorption of metal electrodes due to the surface plasmon resonance, which reaches its maximum when the polarization direction of the incident light is perpendicular to the metal edge.[68] I further study the power dependence of photocurrent response. As shown in figure 3.2c, a linear relationship with the incident light power is observed at low temperature ($I_{ph} \approx P^{\alpha}, \alpha = 1$), indicating that the number of photo-excited carriers is proportional to that of incident photons, whereas a sublinear behavior is displayed at room temperature ($I_{ph} \approx P^{\alpha}, \alpha < 1$). The sublinear relationship suggests the loss of photo-excited carriers by recombination, which may result from defects and charged impurities either in WSe_2 or at WSe_2-SiO_2 interfaces.[69, 70]

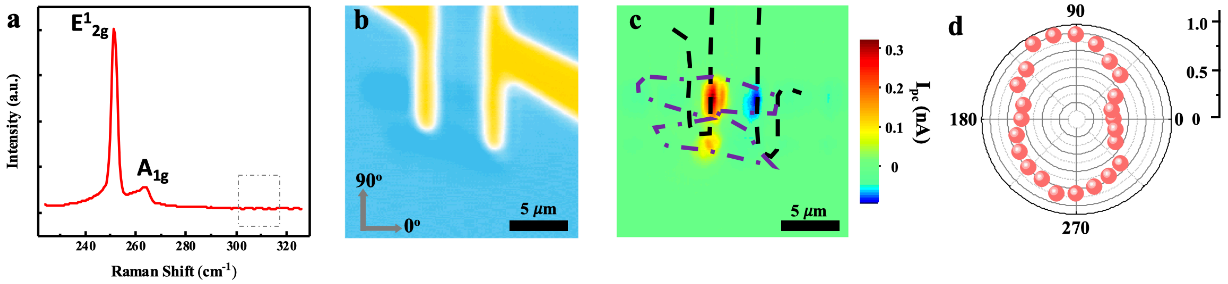

Figure 3.3 Measurement of a monolayer WSe_2 device. (a) Raman spectrum of a monolayer WSe_2 on SiO_2/Si with 532 nm laser illumination. (b) Reflection and corresponding (c) photocurrent images of the monolayer WSe_2 transistor under 650 nm laser illumination. Purple and black dashed lines outline the WSe_2 flake and Electrodes, respectively. (d) Normalized photocurrent intensity extracted from photocurrent images at WSe_2-metal junctions under 650 nm laser illumination at 0 gate voltage.

3.4 Tunable exciton peak via out-of-plane electrical field and temperature

Furthermore, the polarization dependence in WSe_2 may be electrically tunable since the A exciton peak can be shifted from 755 nm to 744 nm when an out-of-plane gate voltage is applied (Figure 3.4a). From the capacitor structure, I can estimate the electric field across the WSe_2 flakes by considering the WSe_2 as an insulator with relative dielectric constant $\varepsilon_w = 20$ and thickness $t_w = 3.2$ nm, lying on the silicon dioxide with relative dielectric constant $\varepsilon_{ox} = 3.9$ and thickness $t_{ox} = 300$ nm.[71, 72] The electric field across the WSe_2 flake is given by

$$F_w = \frac{V\varepsilon_{ox}}{t_{ox}\varepsilon_w + t_w\varepsilon_{ox}}$$

I contribute the observed shift to the quantum confined Stark effect which can modulate the interband optical transition for TMDs.[21-23] Considering the exciton as a polarizable bound EHP with a finite shift along the direction parallel to the basal plane of the crystal. The exciton recombination energy is given by:[21]

$$E(F) = E_0 - p \cdot F - \beta \cdot F^2$$

where E_0 is the exciton recombination energy at $F = 0$, p is the nonzero exciton dipole moment and β is the exciton polarizability. I extracted the polarizability $\beta \approx 3.90 \times 10^{-6}$ Dm/V (Figure 3b), which is two orders of magnitude larger than the out-of-plane value obtained for MoS_2 and is comparable to those characterized via in-plane electric fields.[21-23]

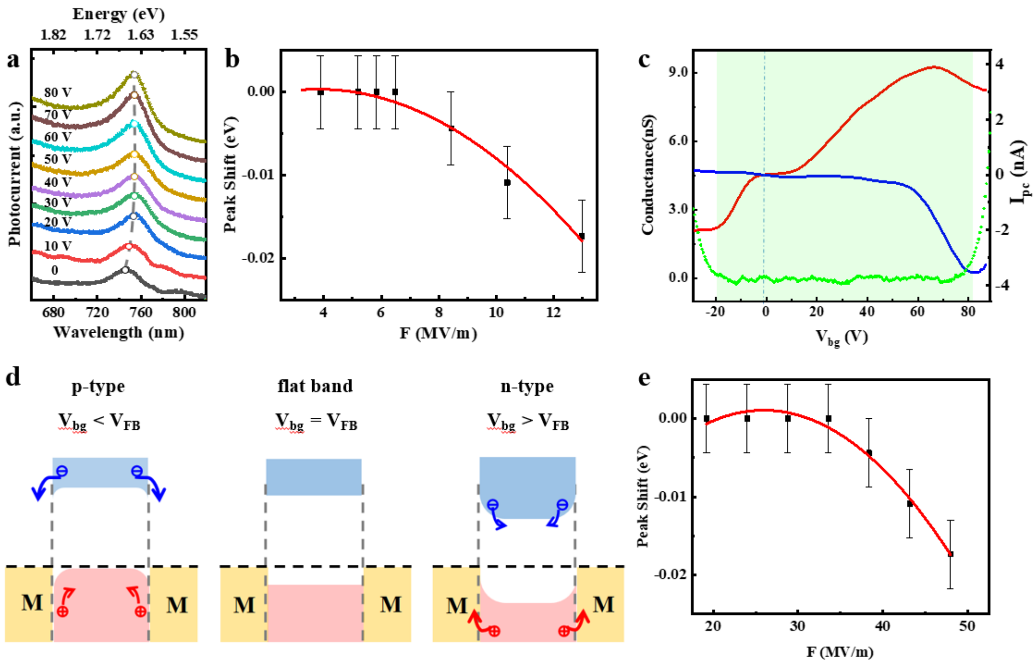

Figure 3.4 Tuning WSe2 photoresponse via electric field. (a) Photocurrent spectra of WSe$_2$-metal junctions under different gate voltages ranging from 0 to 80 V. (b) Photocurrent peak shift as a function of the out-of-plane electric field, extracted from the measurements in (a). The solid red line is a parabolic fit. (c) Gate-dependent photocurrent responses at red and blue triangle regions in figure 3.1d and the conductance measured as a function of the back-gate voltage. The green area illustrates the "off" state of the WSe$_2$ device and the dashed line indicates $V_{bg} = V_{FB}$. (d) Schematic diagrams of energy band diagrams illustrating the mechanisms of photocurrent generation under different gate voltages. (g) Photocurrent peak shift as a function of an in-plane electric field based on the estimate from (c). The solid red line is a parabolic fit.

Here, I added the out-of-plane electric field from heavily doped silicon which could modulate the band bending at the WSe$_2$-Metal junction, leading to an in-plane electric field across the junction. Therefore, both in-plane and out-of-plane electric fields could influence the optical transition in WSe$_2$. To estimate the in-plane electric field, I performed gate-dependent scanning photocurrent measurements. By scanning the gate voltage from -30 V to 90 V, the photocurrent response at the WSe_2–metal junction was recorded under 750 nm illumination (Figure 3.4c). When the Fermi level moves from the valence band to the conduction band, the band diagram varies linearly with a gate voltage: $\delta E_b = e\alpha V_g$, where E_b is the energy from the Fermi level to the valence band and α is a numerical constant that shows how effectively the gate can adjust the band energy.[73-75] The measured shut-off gate voltages for p-type and n-type conductance are -20 V and 80 V, respectively (Figure 3.4c, green area). I also know that the indirect band gap of WSe_2 is 1.20 eV; therefore, the calculated α is about 0.012. The potential across the depletion region at the WSe_2-metal junction can be estimated as $\delta\Phi = \alpha(V_\mathrm{g} - V_\mathrm{flat})$. Under laser excitation, photo-excited EHPs can be efficiently separated and then directed in opposite directions by built-in electric fields at WSe_2-metal junctions. For the p-type region (Figure 3.4d left), the electronic energies are higher in the middle of the WSe_2 device than near the contacts; therefore, electrons can be driven to the drain/source electrode, resulting in a positive/negative current. In addition, negligible photocurrent responses are observed in the center of the device due to the relatively flat band structure. As shown in figure 3.4d middle, when the gate voltage was set to -2 V, the lift of Fermi level flattened the band bending in the contact region, resulting in a flat band structure. Similarly, an opposite polarity of photocurrent signal is detected in the n-type region (Figure 3.4d right). Based on Schottky diode electrostatics,[76] the electric field at the WSe_2-metal interface is given by $F = \delta\Phi/2w$. The depletion width w is chosen as 10 nm, since previous theoretical studies have shown that 2D material-metal junctions have a depletion region with a width about a few tens of nanometer.[77] The polarizability is calculated to be $\beta \approx 1.83 \times 10^{-6}\ \mathrm{D}m/\mathrm{V}$ (Figure 3.4e), which is comparable to the in-plane polarizability previously reported in monolayer TMDs.[21-23] The maximum energetic shift $\Delta E_{max} \sim -25\ me\mathrm{V}$ is much smaller than the exciton binding energy of WSe_2,[78] since the electric field only weakly perturbs the oscillator strength of the transition.

I also notice that the photocurrent response peak can be shifted by environmental temperatures (Figure 3.5a). I extracted the peak position at each temperature (Figure 3.5b) and fit it to a modified Varshni's equation:[79]

$$E_g(T) = E_g(0) - S\langle\hbar\omega\rangle\left[coth\left(\frac{\langle\hbar\omega\rangle}{2k_BT}\right) - 1\right],$$

where $E_g(0)$ is the band gap at 0 K, S is a dimensionless electron-phonon coupling parameter, $\langle\hbar\omega\rangle$ is the average acoustic phonon energy involved in electron-phonon interactions. From the fitting in Figure 2.5b, $S \approx 1.67$ and $E_g(0) \approx 1.73\ eV$ are extracted for A exciton, respectively. I notice that $E_g(0)$ is comparable to that of monolayer WSe_2 (1.74 eV), while S is smaller than previous reports for monolayer WSe_2 (2.06 or 2.33).[79, 80] This indicates that the electron-phonon coupling in few-layer WSe_2 is weaker than that in its monolayer structure, likely due to the increased effective mass from monolayer to few-layer WSe_2.[80] As I increasing the temperature, the A exciton energy of WSe_2 becomes smaller, leading to the peak shift of photocurrent spectra at various temperatures. These studies may provide a new strategy to modulate the photocurrent polarization direction of WSe_2 by shifting its A exciton energy via temperature.

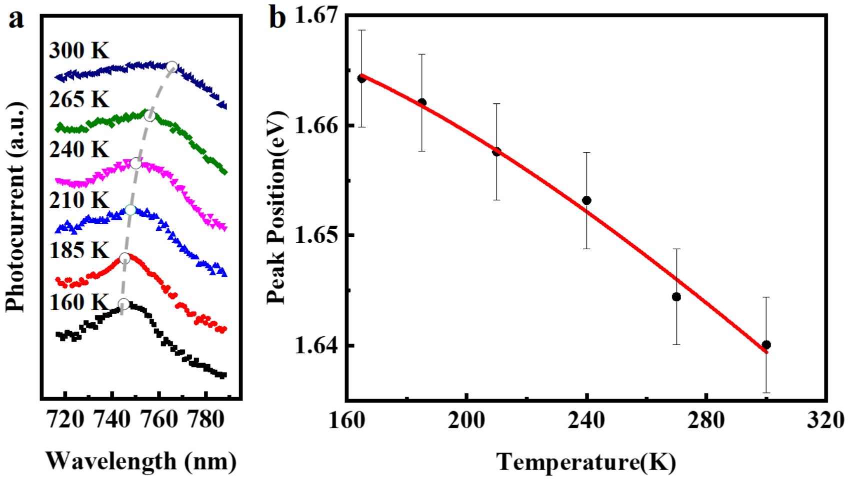

Figure 3.5 Tuning WSe_2 photoresponse via temperature. (a) Photocurrent spectra of WSe_2-metal junctions at various temperatures ranging from 160 K to 300 K. (b) Photocurrent peak shift as a function of temperature, extracted from the measurements in (a). The solid red line is a fit to the data using a modified Varshni's equation.

3.5 Conclusion

In conclusion, I systematically investigate the photocurrent generation mechanisms at the WSe_2-metal junctions via wave- length-, polarization-, gate-, and temperature-dependent scanning photocurrent measurements. I find that if the photon energy is above the A exciton energy, the maximum photo- current response appears for the light polarization direction along the metal electrode edge, suggesting that electrons in the valence band of WSe_2 tend to obtain photons with the polarization direction perpendicular to their momentum direction. Such a linear polarization behavior is known as the optical momentum alignment effect because of the pseudospin- induced optical selection rule. Similar behavior has been widely studied in conventional semiconductors. If the photon energy is lower than the A exciton energy, the photocurrent signals are maximized when the polarization direction of the incident light is perpendicular to the metal electrode edge, which mainly result from hot electrons generated by the polarized absorption of the gold electrodes due to surface plasmon resonances. More interestingly, the photocurrent peak can be modulated by either an external electric field or environmental temperature. These experimental studies provide an in-depth understanding of photocurrent generation mechanisms, offering new design rules for future 2D TMD-based anisotropic optoelectronics.

Chapter 4 Probing Neural Activities in Retina via Graphene Biosensor

4.1 Introduction

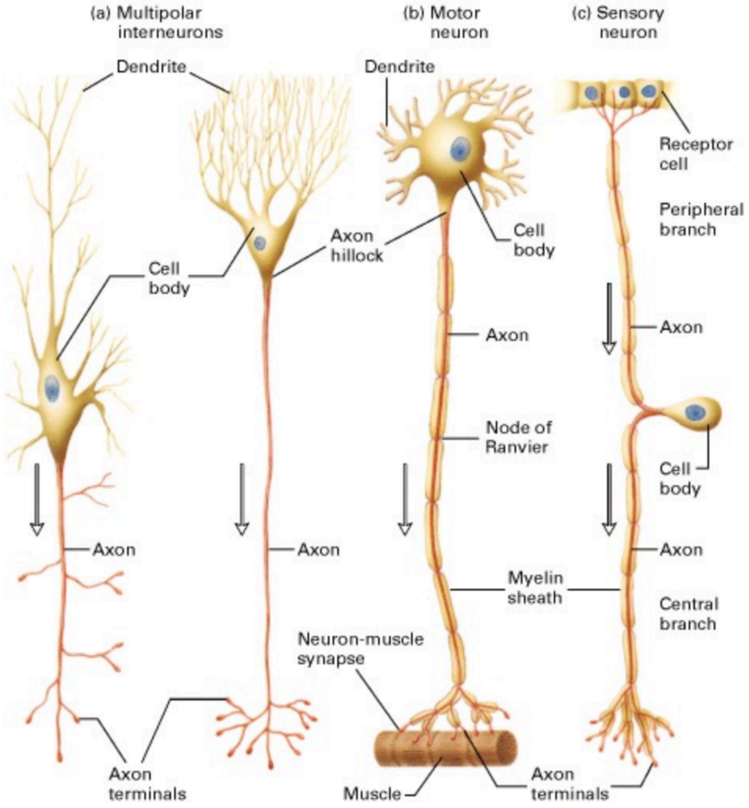

Figure 4.1 Basic types of neurons. Arrows indicate the direction of conduction of action potentials in axons (red). (a) Multipolar interneurons. Each has profusely branched dendrites, which receive signals at synapses with several hundred other neurons, and a single long axon that branches laterally and at its terminus. (b) A motor neuron that innervates a muscle cell. Typically, motor neurons have a single long axon extending from the cell body to the effector cell. In mammalian motor neurons an insulating sheath of myelin usually covers all parts of the axon except at the nodes of Ranvier and the axon terminals. (c) A sensory neuron in which the axon branches just

after it leaves the cell body. The peripheral branch carries the nerve impulse from the receptor cell to the cell body, which is located in the dorsal root ganglion near the spinal cord; the central branch carries the impulse from the cell body to the spinal cord or brain. Both branches are structurally and functionally axons, except at their terminal portions, even though the peripheral branch conducts impulses toward, rather than away from, the cell body.[81]

As an important building block of nervous system, the electrically excitable cell: neuron typically consists of a coma, dendrites and an axon, which communicating with others cells via synapses. Figure 4.1 shows typical types of neuron with signal transport direction. Signals are transported via dendrites to soma and out down through axon for most neurons. At resting, the voltage gradient across their membranes called membrane potential is at -70 mV (Figure 4.2). Under a large enough excitation, the neuron will generate an electrochemical pulse: action potential, which will change the membrane potential to 30 mV and travel rapidly along the axon, exciting the following neurons via synapses. In the human, hundreds of different types of neurons together with glial cells, which provides nutrition and support for neurons, boost and modulate for signal transmissions, established an extremely complex nervous system. It is still unclear how such complicated network cooperates and realize various functions such as sensory, integration and motor, which is critical for understanding and dressing the disorders of the nervous system, including Alzheimer’s disease, Parkinson’s disease, epilepsy.

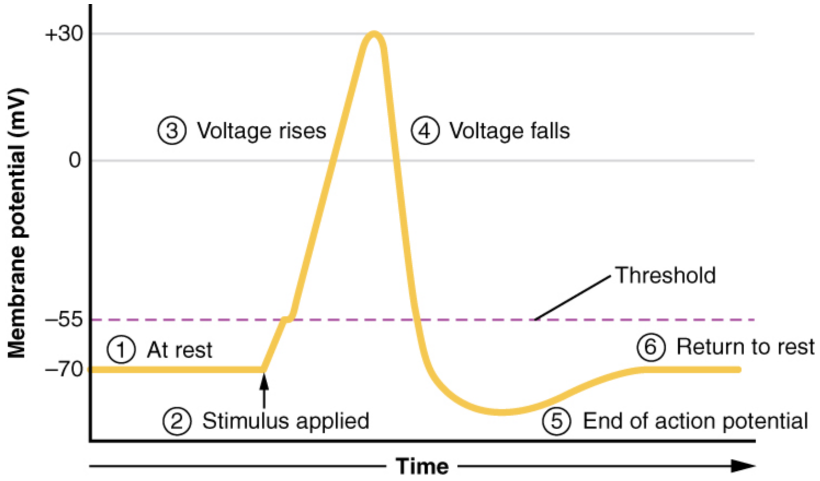

Figure 4.2 Stages of an Action Potential. Plotting voltage measured across the cell membrane against time, the events of the action potential can be related to specific changes in the membrane voltage. (1) At rest, the membrane voltage is -70 mV. (2) The membrane begins to depolarize when an external stimulus is applied. (3) The membrane voltage begins a rapid rise toward +30 mV. (4) The membrane voltage starts to return to a negative value. (5) Repolarization continues past the resting membrane voltage, resulting in hyperpolarization. (6) The membrane voltage returns to the resting value shortly after hyperpolarization.[82]

The retina is a window to the brain and as a part of the central nervous system (CNS), shares similar properties with the brain, making it an ideal candidate for studying physiological and pathological activities in the CNS.[83-86] Three cellular layers are connected by two layers of synapses formed by the axons and dendrites of neurons in the retina (Figure 4.3). The outer nuclear layer of the retina contains the cell bodies of light receptors, the rods and cones, which are responsible for dim light and precise color vision, respectively. Photoreceptor responses to light stimuli are transmitted as a grated potential through center layers to retinal ganglion cells (RGC). RGCs, in turn, transmit visual information to the brain via producing action potentials conducted along their axons in the optic nerve. The optic nerve head (ONH) is the region of the retina where

RGC axons are bundled together prior to exiting the globe of the eye. This area does not contain neuronal soma and is associated with the "blind spot" in visual perception. However, it is an area of concentrated electrical activity due to the tight bundling of unmyelinated RGC axons.

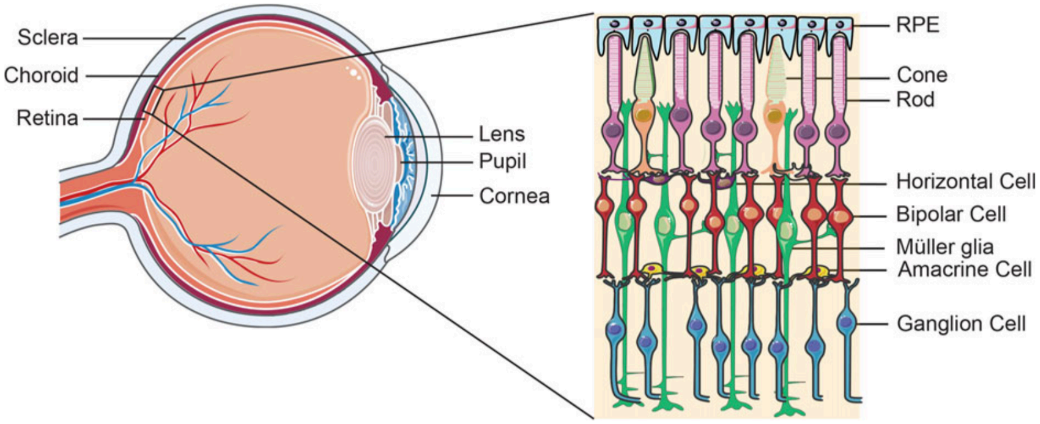

Figure 4.3 Schematic of the eye and retina structure. The magnified area represents different cell types in the retina.[87]

Various techniques have been developed to study the neural activity. Patch-clamp recording can record voltage or current signals of a single cell with high electrical sensitivity and has been widely used to investigate neural activity *in vitro* and *in vivo*.[88-91] Nevertheless, the sizeable probe tips and bulky micromanipulators involved in this technique make it challenging to investigate a large population of cells in an entire neural network. Recently, various kinds of fluorescence sensors, such as voltage sensitive dyes and calcium indicators, have been utilized to optically record electrical activities in neural networks with high throughput.[92, 93] However, the electrical sensitivity of optical imaging is significantly lower than that of patch-clamp recording.[94] With arrays of electrode, microelectrode arrays (MEAs) can stimulate and record a large population of neurons simultaneously, making it a powerful technique to study the functions and connections of neural networks.[95-97] Although field effect transistors (FETs) have been applied to improve the electrical sensitivity, electrode density and physical contact problems are still limiting the capability of MEAs in studying neural networks.[98, 99] The limitations of these currently available technology thus call for new approaches to further improve our capability to probe and understand complex nervous system.

Here, I combine graphene FETs with scanning photocurrent microscopy to detect the neural activity of mouse retina, which is placed on microfluidic platforms that can keep whole mouse retina healthy for multiple days.[100] Electrical activity in living retinal tissues can modulate the carrier concentration of graphene, resulting in potential gradients that can separate photo-excited electron-hole pairs (EHP) and produce photocurrent signals. In our experiments, strong photocurrent responses are detected from the graphene underneath ONH, suggesting that the electrical activity of the ONH is sufficient to alter the local electrical properties of graphene. I also find that no remarkable photocurrent response is detected from the graphene underneath both dehydrated and fixed retina, which further confirm that the photocurrent signals in graphene that I observe are indeed from the electrical activity in living tissues.

Significant research endeavors are ongoing to explore potential applications of graphene for imaging, biosensing, drug delivery, and tissue engineering.[101-104] While great progresses have been made on almost all fronts, many fundamental questions pertaining to biomedical applications of graphene still remain unanswered. One critical issue for biomedicine is how graphene influences the behavior of living cells or tissues, which is still not well understood despite the general acceptance that graphene is biocompatible.[105-112] A few groups have conducted studies to examine *in vitro* viability of primary neuronal cultures or human neuroblastoma cell lines on graphene substrates.[105-107, 109-112] Cell culture on bare graphene allows for direct interactions between the cells and graphene. However, graphene on bare glass substrates omits the supportive properties of matrix substrates, which increase in importance from neuroblastoma cell lines to primary neuronal cultures. The resultant studies suggest that neurons can be grown on bare graphene adhered to glass, but are conflicted on whether graphene influences cell viability and vitality.[105, 107, 108, 110, 113] Although the outcomes of these studies are also conflicting, most indicate that the graphene underneath organic matrix substrates does not adversely impact cell adhesion, viability or vitality.[105, 112] Thus, it is vital to clarify whether graphene impedes the ability of neurons to interact with biological elements in their environment that exist prior to applying graphene.

Here, a systematic study was performed to determine whether applying graphene on top of organic matrix substrates masks interactions between these matrix substrates and primary cultures of purified neurons. I fabricated six different platforms for primary cultures of retinal ganglion cells (RGCs) that were comprised of matrix substrates known to have low, medium and high efficacy for these neurons. Three of the culture platforms included a layer of graphene placed on top of the matrix substrate. Using these platforms, I determined whether graphene overlay and the resultant direct contact between RGCs and the graphene layer alters substrate efficacy, as measured by several important indices of cell viability and vitality, including receptor-mediated endocytosis and neurite outgrowth. I further assessed the specific potential for graphene to serve as a biosensor in electrophysiological assays by measuring substrate and graphene effects on cation channel activity. For all measures and culture substrates, direct contact between RGCs and graphene does not impede interactions between RGCs and underlying substrate matrix. That the positive and negative effects of the different substrates remained consistent with graphene overlay indicates that graphene is biocompatible. These findings support feasibility of graphene as a biosensing material for *in vitro* applications in neuroscience, such as electrophysiological assays.

Table 1 *In vitro* viability of cell culture on graphene substrates from previous researches.

Citation	Cell type	Substrates	Main results
[105] Veliev et al. 2016 Biomaterials	Primary hippocampal neurons (from embryonic E16.5 mice)	Poly-L-Lysine (PLL) coated glass, PLL coated graphene, bare graphene	Increased density of attached neurons on bare graphene; Decreased neurite number on bare graphene; Increased neurite outgrowth on coated graphene compared to bare graphene
[106] He et al. 2016 Biointerfaces	Primary hippocampal neurons (from postnatal P0 rats)	Graphene on glass, tissue culture polystyrene (TCPS) (both coated with poly-lysine)	Increased growth cone growth, neurite sprouting/outgrowth, & complexity of dendritic network on graphene; Higher frequency of spontaneous post synaptic currents (sPSC) on graphene; Neurons couldn't grow on graphene or TCPS without coating
[107] Lee et al. 2015 Biochem. & Biophys. Res. Comm.	Human neuroblastoma SH-SY5Y cells (neural differentiation with RA)	Glass, graphene on glass	Increased neurite outgrowth on graphene
[108] Fabbro et al. 2016 ACS Nano	Primary hippocampal neurons (from postnatal P2-P3 rats)	Graphene on glass, Control (glass or polyornithine-coated glass)	Normal morphology & cell density on all substrates; no effect on sPSC or induced PSC or synaptogenesis on all substrates
[109] Bendali et. al. 2013 Adv. Healthcare Mat.	Primary retinal ganglion cells (from adult rats)	Glass +/- Poly-D-Lysine (PDL)/laminin coating, graphene on sapphire +/- coating	Decreased cell survival, cell body area, & neurite outgrowth on graphene compared to glass (-coating); Decreased neurite outgrowth on graphene compared to glass (+coating); Decreased cell body area & neurite outgrowth on both substrates -coating compared to +coating
	Primary retinal ganglion cells (from postnatal P7 rats)	Glass +/- PDL/laminin coating, graphene on sapphire +/- coating, sapphire +/- coating	Decreased cell viability, neurite outgrowth, & total processes on all substrates -coating compared to +coating; Increased cell body area on all substrates -coating compared to +coating (cell aggregation)
[110] Sahni et al. 2013 J. Neurosurg. Ped.	Primary rat cortical neurons	Uncoated permanox dishes, PDL coated dishes, graphene	No deleterious effect of graphene on neuronal attachment, growth, or morphology; No evidence of cytotoxicity between substrates; Increased LDH activity on graphene compared to PDL coated; Decreased LDH activity on graphene compared to uncoated substrate
[111] Park et al. 2013 J. Microbio. Biotech.	Human nerve SH-SY5Y cells	Glass +/- graphene coating, SiO_2/Si +/- graphene coating	Normal percentage cell viability, cell survival, & morphology on all substrates
[112] Li et al. 2011 Biomaterials	Primary hippocampal neurons (from postnatal P1 mouse)	TCPS, graphene on TCPS (both coated with PLL)	Normal neuron growth, morphology, density, metabolic activity, & membrane integrity on both substrates; Increased neurite outgrowth on graphene

4.2 Graphene biocompatibility evaluation

To investigate whether graphene overlay impedes interactions of neurons with underlying biological elements, I performed studies with primary cultures of RGCs. RGCs are projection neurons, whose axons form the optic nerve. Like other projection neurons, establishing and maintaining RGCs as primary cell cultures can be challenging. Optimal establishment of these cultures requires precise culture conditions, including application of a substrate matrix and media enrichment with supplemental amino acids and an extensive panel of neurotrophic and growth factors. [114-117] The sensitive nature of these neurons *in vitro* improves applicability of our findings to other neuronal subtypes, many with less stringent culture requirements.

As demonstrated by significant previous literature, laminin is the preferred substrate for primary RGC cultures. [118-123] Anecdotally, bare glass and PDL are generally considered sub-optimal, with PDL being preferable to bare glass. While these substrates have not been formally compared for efficacy, field standards for primary RGC cultures indicate that these three substrates represent a continuum of efficacy for the establishment of viable and vital RGCs. As such, I designed six different culture schemes, using these three substrates. I produced three substrate-only platforms. The first was a bare glass coverslip with no matrix substrate. The second and third platforms were glass coverslips coated with either laminin or PDL. I then adopted three graphene-integrated versions of the substrate-only platforms. For one platform, I placed graphene on bare glass (Figure 4.4a, left panel). For the remaining two platforms, I coated glass coverslips with either laminin or PDL followed by graphene overlay (Figure 4.4a, middle and right panel). As depicted in Figure 4.4a, RGCs were in direct contact with graphene in the graphene-integrated platforms. All cultures, regardless of platform, were maintained in optimal growth media for RGCs, as previously described.[117, 124]

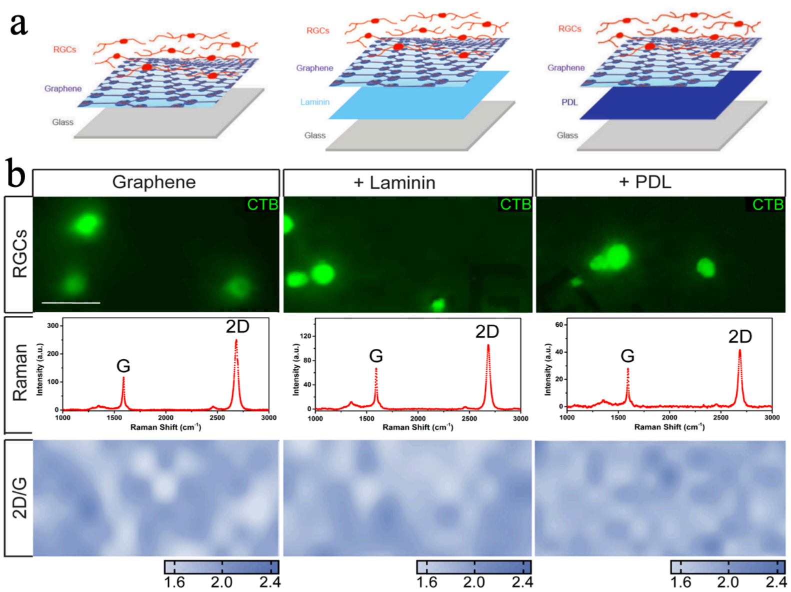

Figure 4.4 Culture substrates configuration. (a) Assembly schematics for graphene-integrated devices. Glass coverslips were coated with laminin or PDL. Graphene was then placed on top of laminin or PDL coating. RGCs were plated directly on top of graphene. (b; top panel) Representative fluorescent micrographs of RGCs cultured graphene alone (left), laminin (middle) or PDL (right) with graphene overlay. RGCs were labeled with CTB conjugated to Alexa Fluor-488 (green). (b; second panel) Quality of the graphene alone, or on laminin or PDL, was assessed by Raman spectra and intensity ratio mapping of 2D and G peaks (b; third panel). Scale bar = 10 μm; Images taken at 40x.

To view cells in our culture, RGCs were labeled with the neural tracer CTB conjugated to Alexa 488 fluorophore (Figure 4.4b; top panel). To make sure that these cells were cultured on graphene, I examined the graphene using Raman spectroscopy following cell plating and exposure to standard culture conditions for one week. As shown in the second panel of Figure 4.4b, the 2D (~2681 cm^{-1}) peak exhibited a symmetric shape and the 2D-to-G (~1583 cm^{-1}) intensity ratio was about 2, which indicates that the graphene had a monolayer structure. To characterize the continuity of the graphene, I extracted and plotted intensity ratio mapping of the characteristic graphene Raman 2D-G intensity ratio. This spatial mapping revealed continuous distribution of graphene underneath RGCs with glass, laminin and PDL substrates (Figure 4.4b; third panel). These data indicate that: 1) successful transfer of graphene on laminin and PDL matrix is feasible, 2) graphene remains intact following cell plating and after exposure to the environmental conditions of cell culture (i.e. 37°C and 5% CO_2) for at least one week, and 3) direct contact with neurons does not disrupt the graphene layer, regardless of underlying substrate.

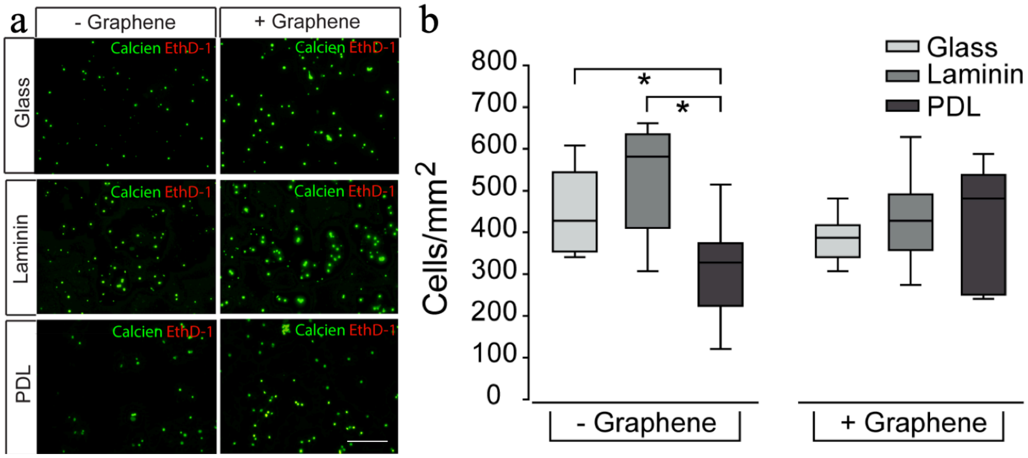

Figure 4.5 Matrix substrate, but not graphene overlay, impacts RGC density. (a) Representative fluorescent micrographs of RGCs cultured on glass (top), laminin (middle), or PDL (bottom) with (+) or without (-) graphene overlay. RGCs were labeled with calcein (green) and ethidium homodimer-1 (red). Scale bar = 100 µm. (b) Box plot of total cell density (y-axis; cells/mm^2) in each culture platform. Asterisks indicate $p < 0.05$.

Viability, the ability of a cell to survive or live in its conditions successfully, is a key parameter for *in vitro* cell culture. Therefore, I measured RGC survival as a function of culture substrate and determined the impact of graphene overlay on the survival baselines for each of these substrates. RGC survival was determined by plasma membrane integrity and the presence of intracellular enzyme activity, using a Viability/Cytotoxicity assay (LIVE/DEAD™ Kit, ThermoFisher). I labeled RGC cultures one week after plating with calcein-AM (green) and ethidium homodimer-1 (EthD-1, red) to measure intracellular enzyme activity and plasma membrane integrity, respectively. Calcein-AM is a cell-permeable dye that enters cells through passive diffusion. Once inside the cell, esterase enzymes remove the acetomethoxy (AM) group to produce a cell-impermeant, polar molecule that is highly fluorescent.[125] EthD-1 is a DNA/RNA stain that is impermeable to cells with an intact plasma membrane.[126] Cells that label calcein+ only are designated as "live" or "viable" cells, whereas cells that label EthD-1+ only are designated as "dead" cells.[127, 128] Cells that label positive for both calcein and EthD-1 are designated as "compromised" due to a disrupted plasma membrane that allowed EthD-1 to enter, but still retain active intracellular enzyme activity to convert calcein-AM to calcein.

For cultures plated on bare glass as well as both matrix substrates a majority of RGCs were calcein+ (green) with minimal co-labeling with EthD-1 (yellow), as shown in broad-field fluoromicrographs (Figure 4.5a). This baseline level of cell compromise was consistent with previous studies.[124] EthD-1+ only cells (red) were essentially not detected at this one-week time point in any of our culture platforms (Figure 4.5a). Quantification of calcein and EthD-1 labeling revealed that graphene overlay did not alter RGC density, as compared to their respective substrate-only platforms ($p > 0.05$; Figure 4.5b). Importantly, comparison between platforms with and without graphene overlay indicates that graphene does not alter cell viability and the overall health of the cells in these two groups is similar. While it is not our main concern here, I found that the density of RGCs was 31% and 41% lower in the PDL platform, as compared to bare glass and laminin platforms, respectively ($p < 0.05$ for both; Figure 4.5b). The reduced RGC density noted in the PDL and graphene-PDL platforms could be due to either a reduction in cell adherence at the time of plating or to increased cell attrition prior to the one-week time point.

In addition to cell viability, it is of critical importance that graphene overlay does not impede the ability of matrix substrate to improve RGC vitality, or activity. To determine whether graphene overlay altered the ability of RGCs to execute a more complex cellular function, I first assessed receptor-mediated endocytosis across our culture platforms, using the active uptake, active transport tracer CTB. This tracer is commonly used to measure axon transport and connectivity in RGCs.[129-133] CTB binds to the GM1 ganglioside receptor and enters RGCs via caveolin-1-mediated endocytosis.[132, 133] Following endocytosis, CTB is trafficked to RGC terminals via the microtubule network.[129, 131] The activity required for uptake and transport of CTB makes it an ideal marker of not only viability, but also cell vitality. It is important to distinguish between a cell that is technically "viable" as it is able to survive in its conditions, and a cell that is maintaining vital, activity-dependent intracellular processes.[128]

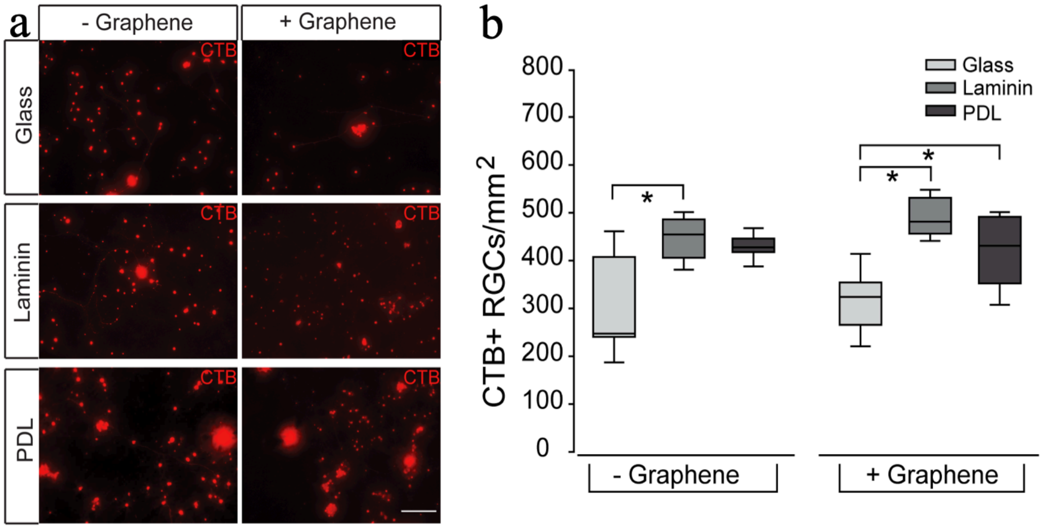

Figure 4.6 Receptor-mediated endocytosis of CTB in RGCs on culture substrates with graphene overlay. (a) Representative fluorescent micrographs of RGCs cultured on glass (top), laminin

(middle), or PDL (bottom) with (+) or without (-) graphene overlay. RGCs were labeled with CTB conjugated to Alexa Fluor-594 (red). Scale bar = 100 μm. (b) Box plot of CTB+ cell density (y-axis; cells/mm^2) in each culture platform. Asterisks indicate $p<0.05$.

In our studies, one week after plating in our six culture platforms, RGCs were treated with CTB conjugated to Alexa Fluor-594 (red) for 24 hours. CTB uptake and transport was visualized by live cell fluorescent imaging. All culture platforms contained CTB+ RGCs, which exhibited CTB in both the soma and along neurites (Figure 4.6a). Quantification of CTB+ RGC density shows that the density of CTB+ RGCs in graphene-integrated platforms did not differ statistically from their respective substrate-only platforms ($p > 0.05$ for all; Figure 4.6b). As such, I conclude that RGCs in the graphene-integrated platforms exhibited similar vitality to those in their respective substrate-only platforms, indicating that graphene overlay did not alter the measured efficacy of glass, laminin or PDL substrates.

As to the effects of different matrix substrates, I found that the laminin-only platform contained 32% more CTB+ RGCs than the bare glass platform ($p < 0.05$; Figure 4.6b). The PDL-only platform contained a median density of CTB+ RGCs that was between bare glass and laminin platforms ($p > 0.05$; Figure 4.6b). For the graphene-integrated platforms, graphene overlay on bare glass contained 35% and 25% lower density of CTB+ RGCs than graphene overlay on laminin and PDL, respectively ($p < 0.05$ for both; Figure 4.6b). These data suggest that while PDL substrate yields the lowest absolute density of RGCs (Figure 4.5), the vitality of these RGCs, as measured by receptor-mediated endocytosis, is higher than that achieved with a bare glass substrate.

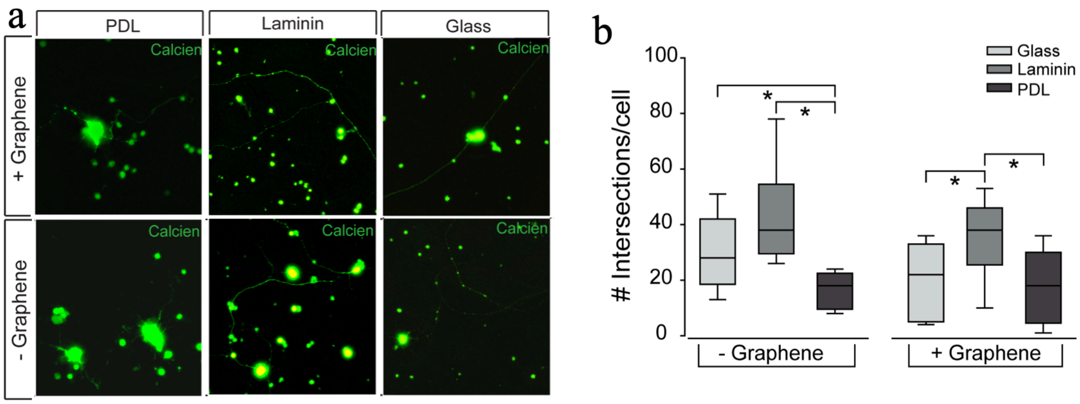

Figure 4.7 RGC neurite outgrowth on culture substrates with graphene overlay. (a) Representative fluorescent micrographs of RGCs cultured on glass (right), laminin (middle), or PDL (left) with (+) or without (-) graphene overlay. RGCs were labeled with calcein (green). (b) Box plot of the number of intersections per cell (y-axis) in each culture platform. Intersections were counted as the number of times any neurite crossed a line in the 25x25 μm grid that was overlaid on fluoromicrographs of 20x magnification. Asterisks indicate $p<0.05$.

In addition to receptor-mediated endocytosis, I adopted neurite outgrowth as another important indicator of neuronal vitality *in vitro* to assess whether graphene overlay affects the cell function. To measure neurite outgrowth in our six culture platforms, I quantified the complexity of RGC neurites with live cell imaging in cultures labeled with either calcein-AM or CTB (Figure 4.7a). Neurite complexity was measured by counting the number of times calcein+/CTB+ neurites intersected the lines of a 25 μm x 25 μm grid mask placed on each fluoromicrograph. This method of quantification accounts for changes in both the length and complexity of RGC neurites. The complexity of axonal branching is particularly important in establishing neural circuits; one of the primary reasons this method of quantification was chosen. [134]

The quantification results revealed that the number of intersections between the grid mask and RGC neurites was 2-fold higher in the laminin platform and 1.5-fold higher in bare glass platform than in the PDL platform ($p < 0.05$ for both; Figure 4.7b). Importantly, RGCs cultured on the graphene-integrated laminin platform also exhibited the most neurite outgrowth, with ~1.5-fold more intersections than graphene-integrated glass and PDL platforms ($p < 0.05$ for both; Figure 4.7b). Overall, there is no significant difference in neurite outgrowth, as measured by the number of intersections, between graphene-integrated platforms and their respective substrate-only platforms ($p > 0.05$; Figure 4.7b), indicating that graphene overlay does not alter efficacy of glass, laminin or PDL substrates.

As to the effects of different matrix substrates, Figure 4.7b suggests that PDL matrix impedes neurite outgrowth in RGCs, while laminin matrix promotes neurite outgrowth. Bare glass exhibits median efficacy as a substrate for neurite outgrowth that is similar to laminin in substrate-only devices and similar to PDL in graphene-integrated devices.

Ion channel activity is essential to neuronal function, particularly neurotransmission, and is the basis for electrophysiological assays. To more specifically assess the potential application of graphene as a biosensor for electrophysiological assays, which require direct contact between neuronal processes and graphene, I measured the effect of graphene overlay on cation channel activity in RGCs across our three culture substrates.

One week after plating cells in our six culture platforms, I performed real-time, thallium flux imaging.[135] In this assay, thallium acts as a surrogate for cations and a fluorescent signal is generated by thallium binding to a cell-permeable Thallos dye. Similar to traditional calcium imaging, increased fluorescent signal indicates opening of cation channels, which are promiscuously permeable to thallium. The representative images in Figure 4.8a depict baseline fluorescence of Thallos dye (left panels) and fluorescence after the addition of thallium (right panels). For illustration purposes, heat maps of the fluorescence signal for individual cells are depicted in panel insets (Figure 4.8a). For statistical comparison, I quantified cation channel activity as the change in fluorescent intensity of thallium between baseline and peak measurements (peak/baseline intensity) for individual RGCs (Figure 4.8b). RGCs cultured on bare glass and laminin matrix platforms exhibited similar levels of cation channel activity, as indicated by thallium flux ($p > 0.05$; Figure 4.8b). In contrast, RGCs cultured on the PDL matrix platform exhibited approximately 19-23% less cation channel activity than both glass and laminin substrates ($p < 0.05$; Figure 4.8b). Similarly, RGCs cultured on the graphene-integrated PDL platform exhibited 24% and 42% less thallium flux than RGCs cultured on graphene-integrated glass and laminin platforms, respectively ($p < 0.05$; Figure 4.8b). Like the substrate-only platforms, the graphene-integrated glass and laminin platforms exhibited similar levels of cation channel activity ($p > 0.05$; Figure 4.8b).

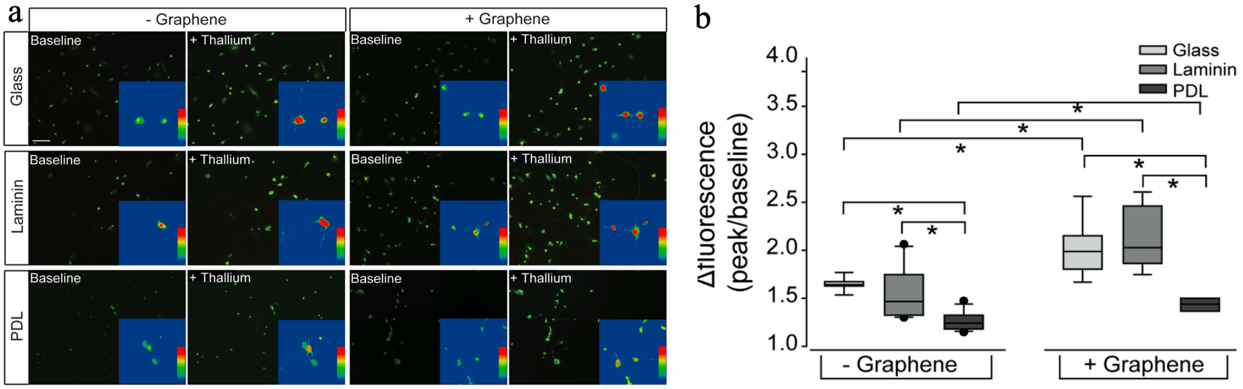

Figure 4.8 (a) Representative fluorescent micrographs of RGCs cultured on glass (top), laminin (middle), or PDL (bottom) platforms with (+) or without (-) graphene overlay. RGCs were loaded with the cell-permeable dye Thallos (green). Images were taken at baseline and after addition of thallium, which binds to and increases the fluorescent intensity of Thallos dye. Insert: zoom of an

individual cell within the larger image analyzed with a heat map showing the fluorescent signal of Thallos dye. (b) Box plot of the change in the fluorescent intensity of each cell (peak intensity/baseline intensity).

Importantly, RGCs cultured on each of the graphene-integrated platforms exhibited greater cation channel activity than their respective substrate-only platforms ($p < 0.05$ for all; Figure 4.8b). This increase in thallium flux ranged from 6% - 37% (Figure 4.8b). These data indicate that: 1) PDL matrix impairs cation channel activity in RGCs, 2) graphene overlay increases overall cation channel activity, regardless of substrate and 3) graphene overlay does not change the relative efficacy of glass, laminin and PDL, which suggests that despite overall enhancement of cation channel activity, graphene overlay does not obscure the cation channel phenotype induced by the culture substrate.

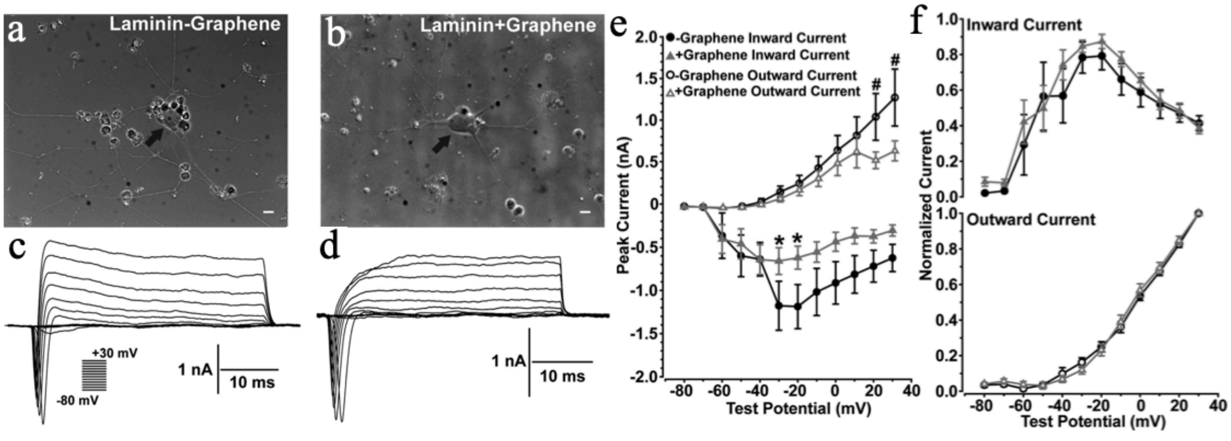

Figure 4.9 Graphene overlay does not alter the biophysical interaction between voltage-gated sodium and potassium channels in cultured RGCs. RGCs cultured on laminin platforms without (-), a) or with (+), b) graphene overlay showed large cell bodies (arrows) with widespread neurite processes. Scale bars = 20 µm. RGCs cultured on laminin platforms without (-), c) or with (+), d) graphene overlay produced transient inward currents followed by prolonged outward currents to

depolarizing test potentials. RGCs cultured on graphene-integrated platforms showed significantly reduced inward (*) and outward (#) currents (e). However, the reduction in inward and outward currents does not alter the biophysical interaction between inward and outward currents (f). (n = 7, -Graphene; n = 10, +Graphene; $*p \leq 0.025$; $\#p \leq 0.015$).

To further inform the changes in ion channel activity seen from the thallium flux studies, I performed whole-cell, patch-clamp recordings on RGCs on laminin and graphene-integrated laminin platforms to measure inward and outward current activity of the cells. In order to simplify the experiments, since the effect of graphene overlay on cation channel activity was similar regardless of substrate and cell integrity is paramount for whole-cell patch clamp, I chose to only culture and record from cells on the preferred cultured substrate for RGCs, laminin. RGCs cultured on both laminin and graphene-integrated laminin platforms showed large somas with neurites extending from the cell body (Figure 4.9a, b). RGCs were further identified physiologically by applying brief, 40 ms, depolarizing test potentials from -80 to 30 mV in 10 mV increments.

RGCs cultured on both laminin and graphene-integrated laminin platforms produced transient inward currents followed by prolonged outward currents to depolarizing test potentials (Figure 4.9c, d). RGC responses were quantified by measuring the peak of each transient inward current and outward current produced by each test potential. RGCs cultured on both laminin and graphene-integrated laminin platforms activated inward current statistically different from zero at -60 mV (Figure 4.9e). RGCs cultured on laminin platforms showed increased inward currents up to -20 mV followed by decreased inward currents from -10 to 30 mV, which is likely due to an interaction between inactivating voltage-gated sodium channels and activation of voltage-gated potassium channels at these higher test potentials. RGCs cultured on both laminin and graphene-integrated laminin platforms showed increased inward currents from -60 to -30 mV followed by a decrease in inward current for remaining test potentials. RGCs cultured on graphene-integrated laminin platforms showed a modest but statistically significant decrease in inward currents for test potentials between -30 to -20 mV as compared to laminin only substrate (*, $p \leqslant 0.025$). Both RGCs cultured on laminin and graphene-integrated laminin platforms showed outward current activation at -30 mV, and outward current generally increased as test potential increased. However, RGCs cultured on graphene-integrated laminin platforms showed a statistically significant decrease in peak outward current between 10 to 30 mV (#, $p \leqslant 0.015$). Reduced inward and outward currents for RGCs cultured on graphene-integrated platforms suggest a decrease in the number of functional voltage-gated sodium and potassium channels.

To understand if graphene impacts the biophysical characteristics of these channels mediating inward and outward currents, I normalized peak inward and outward current values produced at each test potential by the maximum inward or outward current value for each cell. Here, I found no significant difference between inward and outward current profiles (Figure 4.9f) of RGCs cultured on laminin or graphene-integrated laminin platforms, suggesting the reduced number of voltage-gated sodium and potassium channels in RGCs plated on graphene does not influence the biophysical interaction between voltage-gated sodium and potassium channels governing action potential initiation and membrane repolarization.

These studies address one critical issue for neurobiological applications of graphene, that is, how graphene influences the behavior of living neurons, which is still not well understood despite the general acceptance that graphene is biocompatible.[105-112] Through systematic studies, I examine the effect of graphene through comparing the outcomes of viability, vitality and electrophysiological function in primary cultures of RGCs on each of three common substrates (glass, laminin and PDL) with and without graphene overlay. Our results confirm that culture substrate influences the health of primary neurons in culture. When all outcomes are considered, laminin substrate yielded the most robust RGC cultures, as anticipated. Based on anecdotal evidence, I expected PDL matrix to yield more robust RGC cultures than bare glass. However, our data suggest that the efficacy of bare glass and PDL matrix as substrates for RGC cultures depends on the outcome examined. For three of the four outcomes I examined, the bare glass platform yielded more robust RGC cultures than the PDL matrix platform, which suggests that interactions between RGCs and PDL matrix could negatively influence RGC viability, vitality and function.

For all viability and vitality indices examined, graphene-integrated platforms exhibited the same pattern of RGC phenotypes as the substrate-only platforms. This indicates that direct contact between RGCs and graphene does not impede interactions between RGCs and underlying substrate matrix, such that the positive or negative effects of culture substrates are retained. I suspect that as a monolayer atomic structure, graphene reproduced local surface properties (mechanical or charge distribution) of underneath matrix to influence the cultured RGCs on top of it.

Interestingly, I did observe that graphene enhances cation channel activity, as illustrated by an increase in the magnitude of thallium influx. Other studies examining the physiology of neurons cultured on graphene have found a potentiation of neurotransmission through increased presynaptic vesicle number, release probability, and turnover rate.[136] Graphene producing an increase in presynaptic neurotransmission could lead to increased postsynaptic cation channel activity, which is consistent with our thallium flux results on graphene-integrated platforms.

Electrophysiological recordings showed reduced inward and outward currents for RGCs cultured on graphene-integrated platforms, which indicates a decrease in the number of functional voltage-gated sodium and potassium channels. This reduction in cation channel expression could arise from a myriad of alterations, including transcription, translation, protein trafficking and membrane structure.[136] Despite differences in ion channel representation, analysis of overall inward and outward current profiles revealed no significant difference between RGCs cultured on substrate-only or graphene-integrated platforms, indicating that graphene overlay does not alter the overall biophysical properties of RGCs. This is supported by previous studies showing that neurons cultured on graphene substrates do not show significantly altered electrophysiological properties, compared to neurons cultured on traditional culture substrates.[108] Increased cation channel activity, like that noted in our thallium flux assay, could serve as compensatory mechanism to maintain the biophysical properties of RGCs, despite graphene-mediated reductions in the number of functional voltage-gated sodium and potassium channels.

4.3 Graphene probes and devices design

Graphene transistors were fabricated as described in chapter 2. As shown in Figure 4.10b, the 2D peak has a symmetric shape and 2D-to-G intensity ratio is about 2, indicating that the graphene has a monolayer structure.[57] A cylinder was placed on top of graphene transistors and filled with 1X phosphate-buffered saline (PBS) solution. A gold wire was inserted into the cylinder and used as an electrolyte-gate to modulate the electrochemical environment of graphene. Gate-dependent conductance measurement of a typical graphene transistor exhibits the ambipolar behavior of a typical graphene transistor with the Dirac point close to 0.7 V (Figure 4.10c), displaying p-type characteristics at zero gate bias.

After fabricating graphene transistors on a thin coverslip, I placed a slice of agar gel at the bottom of a glass cylinder, which serves as a supporting substrate to hold the retina in place as well as a porous pad that allows fresh media to slowly perfuse through to supply nutrients to the retina from the cylinder (Figure 4.10a). Live retina was dissected and mounted on top of the agar gel. The cylinder was then inverted and inserted into the large hole of the PDMS ring, such that the retina came in contact with graphene transistors. Serum-free culture media containing neurotrophic factors was then added to the glass cylinder to maintain the retina health.[25] Moreover, the media weight on top of the agar gel helps to hold the cylinder in place on top of the retina to restrict curling. Three days prior to enucleation and retina dissection, mice received an intravitreal injection of fluorophore-conjugated cholera toxin subunit B (CTB). CTB is an active uptake and active transport neural tracer that is preferentially endocytosed by RGCs and anterogradely transported along their axons to the axon terminal in the brain. I utilized the tracer to visualize RGCs and the unmyelinated segment of their axons in the retina and ONH during photocurrent recording.[137] As demonstrated in Figure 4.10d, a CTB-labeled (red) whole retina was placed on top of graphene transistors, where the dark regions are opaque gold electrode arrays. The fluorescence image presents the structure of RGCs layer. All the axons of RGCs from different parts of the retina extend from cell soma, group into bundles, and coalesce at the ONH in the center of the retina to exit the globe of the eye.

4.4 Probing the neural activity in retina

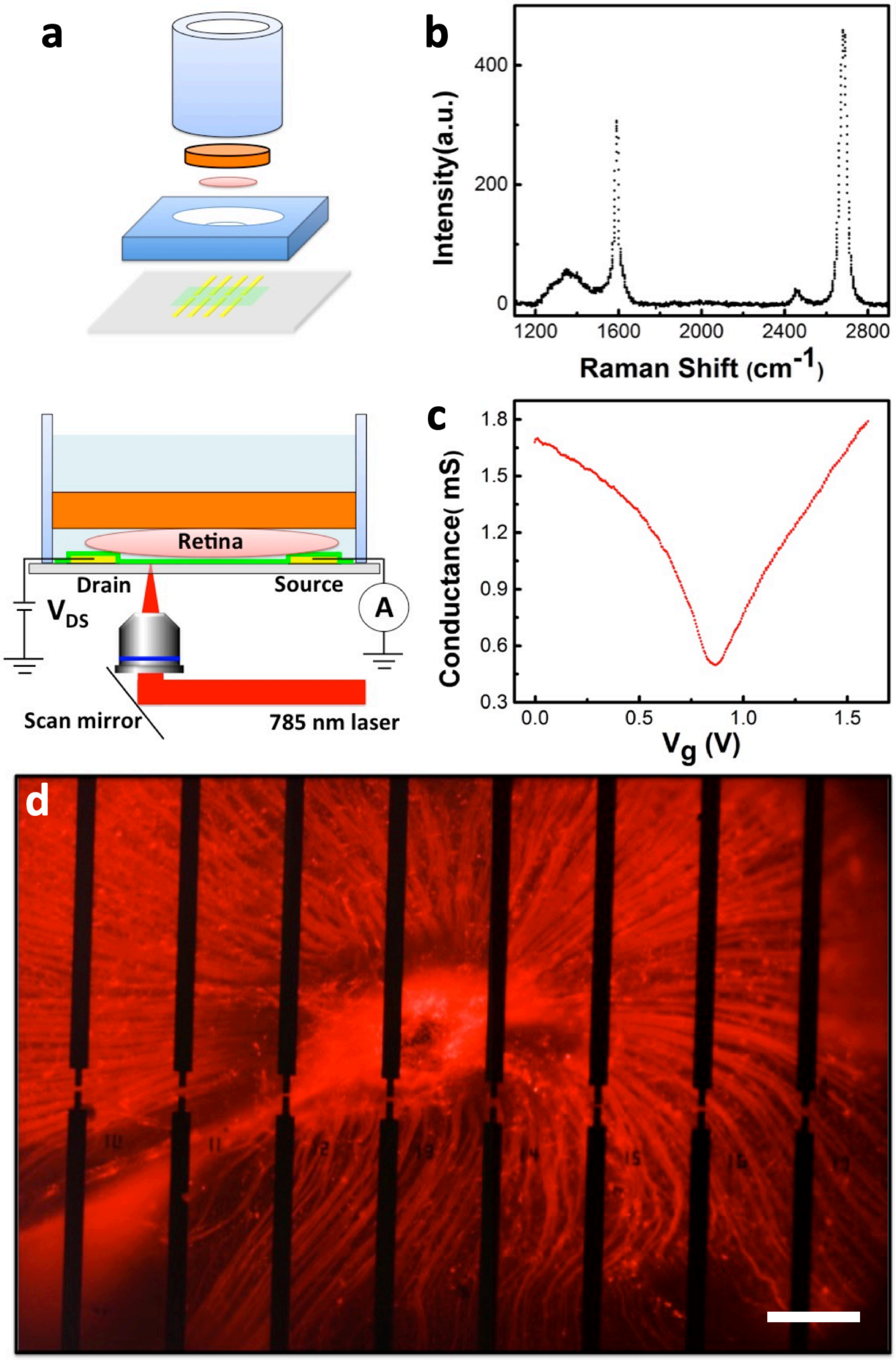

Figure 4.10 Overview of the experimental design. (a) Top: Exploded view of a graphene-integrated microfluidic platform. The orange plate is a slice of agar gel. The pink disk represents

a retina. The green plane indicates a graphene film. The yellow bars represent Au electrodes. Bottom: Schematic diagram of scanning photocurrent measurements. A one-micron diameter diffraction-limited laser spot goes through a transparent coverslip to scan over graphene transistors underneath a retinal tissue in a microfluidic platform. (b) Raman spectrum of graphene on a coverslip. (c) Electrolyte gate response of a typical graphene transistor. (d) Fluorescence image of a CTB-labeled retina on top of graphene transistors. The electrodes array has 27 pairs of electrodes with 220 μm center-to-center distance in horizontal direction. The edge-to-edge distances between upper and lower electrodes are 20 μm, 40 μm and 60 μm in cycles. Here, I show 8 pairs of electrodes near ONH. Scale bar is 200 μm.

To explore electrical activity in retina, I performed spatially-resolved photocurrent measurements through a graphene-integrated microfluidic platform. A continuous-wave laser source with a wave length of 785 nm was selected to prevent the retina from responding to the laser based on the negligible spectral sensitivity of mouse retina to the light of wavelength above 700 nm.[138] The laser beam was deflected by a nanometer-resolution scanning mirror and then focused by a 40× objective (N.A. = 0.6) into a diffraction-limited spot (∼1 μm) on graphene transistors (Bottom panel of Figure 4.10a). The photocurrent signals were collected using a preamplifier and the corresponding reflection image was recorded by a silicon detector. By overlapping the reflection image with the photocurrent image, the corresponding position of the photoresponse on the sample could be located.

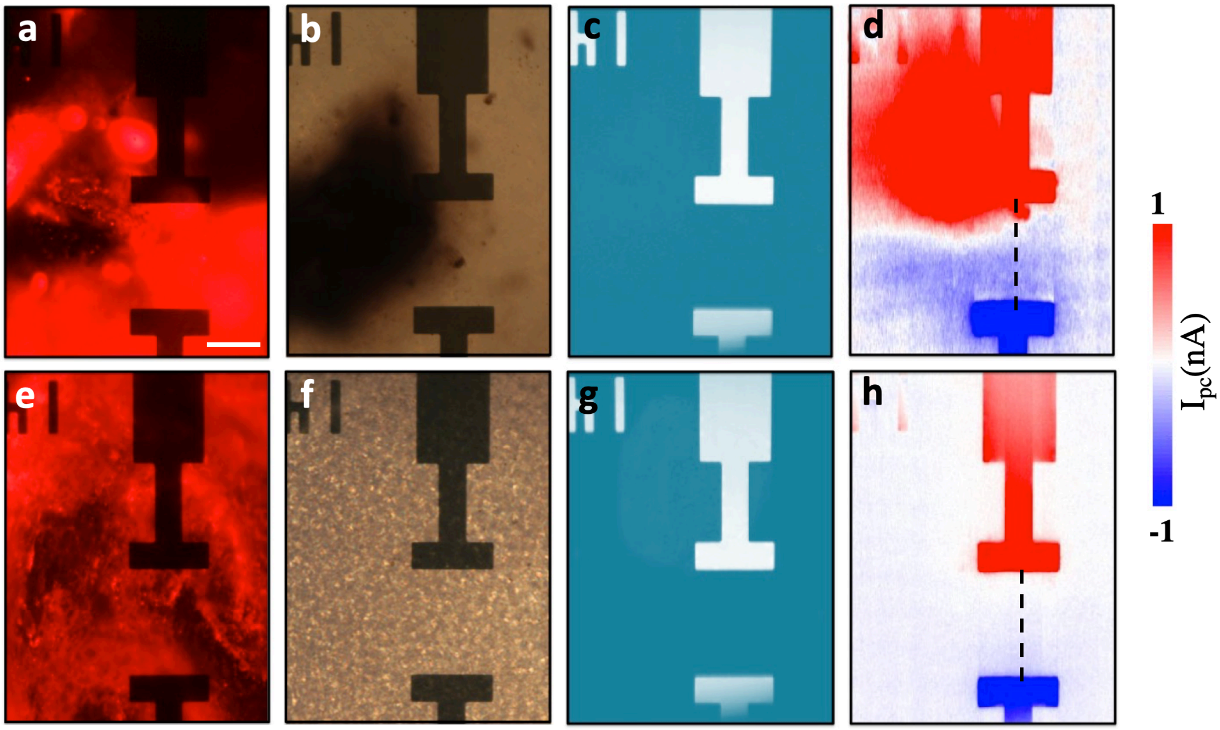

Figure 4.11 Retina on graphene probe. (a) Fluorescence, (b) optical, (c) reflection and (d) scanning photocurrent images of a fresh excised, CTB-labeled retina on top of a graphene transistor in the ONH region, respectively. (e) Fluorescence, (f) optical, (g) reflection and (h) scanning photocurrent images of the retina/graphene at the same location after it is dehydrated at room temperature for 24 hours, respectively. Source and drain electrodes are 45 µm×15 µm. Edge-to-edge distance is 60 µm. Scale bar is 30 µm. The inverted '14' near the upper electrode is a metal marker for location.

Figures 4.11a-d show the fluorescence, optical, reflection, and photocurrent images of a living retina in a graphene-integrated microfluidic platform, respectively. Pronounced photocurrent responses were observed at graphene-metal junction areas with opposite polarity for drain and source electrodes, because the Schottky-like barriers between metals and graphene can efficiently separate photo-excited EHPs (Detailed photocurrent generation mechanisms will be discussed later). More importantly, remarkable photocurrent signals were detected in the ONH region of the living retinal tissue (Figure 4.11d), indicating that the electrical activity of the ONH can module the carrier concentration of graphene and induce photocurrent signals. The photocurrent responses around the bottom electrode are much weaker than those around the upper electrode, which is likely due to the electrical double layer formed between the retina and graphene that can screen the electrical signals from the retina and reduce the photocurrent responses in graphene. As shown in Figure 4.11a, the fluorescence image at the region close to the bottom electrode is out-of-focus, suggesting that the ONH did not contact the graphene substrate around the bottom electrode region well. This mainly results from the naturally curved shape of retina, which is not ideally compatible with the planar nature of graphene-integrated microfluidic platforms. If I can fabricate graphene transistors on flexible substrates (such as PDMS membranes), this issue is likely to be addressed. I also investigated electrical signals in the retina after it was dehydrated for 24 hours. During dehydration, the retinal tissue shrunk, slid, and made a good contact with the graphene substrate (Figure 4.11e and f). However, the electrical properties associated with living retina were eradicated. No significant photocurrent response was observed from the entire dehydrated retina, except the graphene-metal junction areas. As shown in Figure 4.11h, the strong photocurrent signals induced by the living ONH shown in Figure 4.11d disappeared when the ONH was dehydrated and moved away from its previous location, confirming that the photocurrent responses underneath the living ONH were induced by its electrical activity.

To further validate our result, I studied the electrical signals in a paraformaldehyde-fixed retina through scanning photocurrent measurements. Note that release cuts extending to the ONH in the retina was necessary to relieve the stiffness after fixation and successfully flatten the retina for contact with the graphene (Figure 4.12a). During the fixation process, the tissue structure was preserved but biochemical reactions were terminated. As I expected, there is no electrical activity in the fixed retina and thus no photocurrent signal was detected in the ONH region (Figure 4.12b-d). Comparing the photocurrent results from a living retina with those from dehydrated and fixed retina, I verify that our graphene-based scanning photocurrent microscopy is a promising tool to detect electrical signals in living retina.

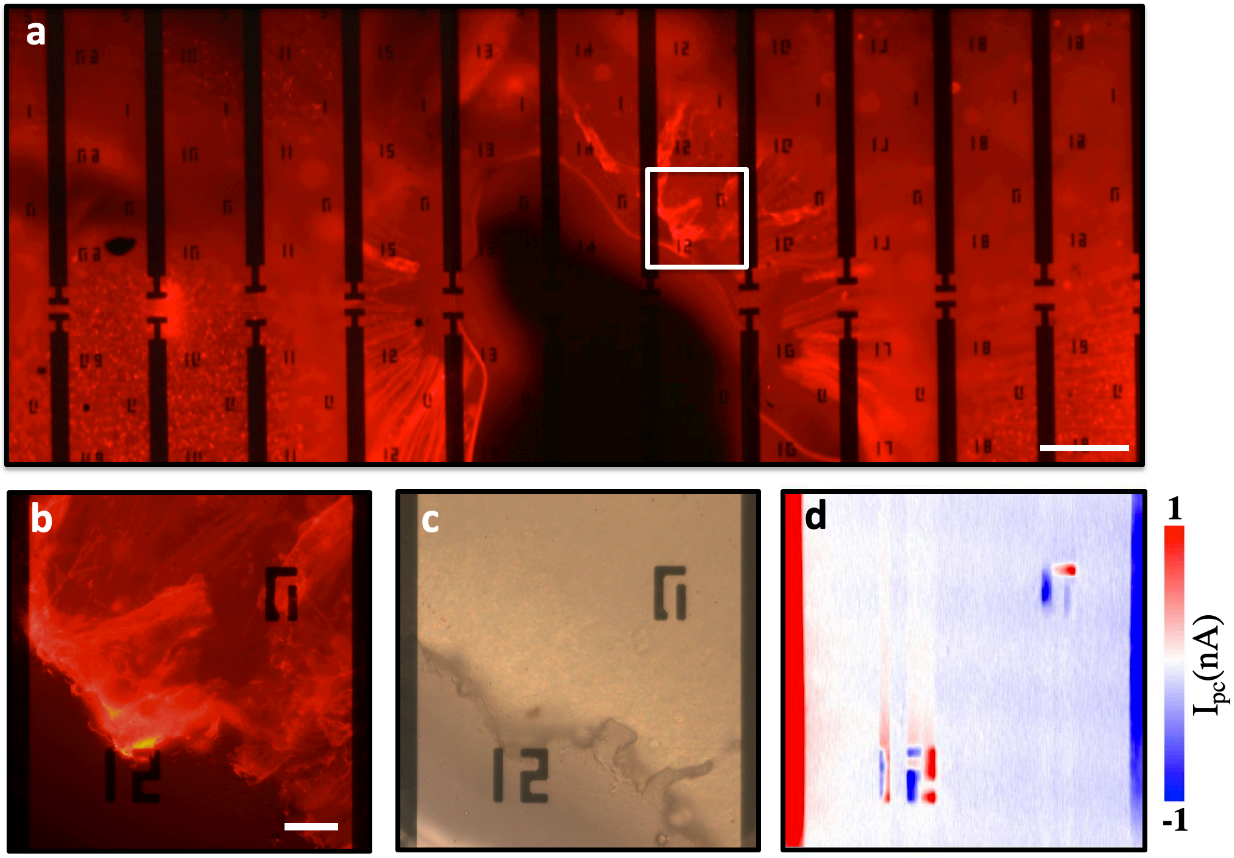

Figure 4.12 Fixed retina for comparison. (a) Fluorescence image of a fixed retina. Scale bar is 200 µm. (b) Enlarged fluorescence, (c) optical, and (d) scanning photocurrent images of the retina in the ONH region, respectively. Source and drain electrodes are 40 µm in width. Edge-to-edge distance is 180 µm. Scale bar is 30 µm in B-D. ’12’ and ’0’ near electrodes are metal markers for location.

4.5 Photocurrent generation mechanism

For better understanding of the photocurrent generation mechanisms in graphene transistors underneath living retina, relative potential profiles across graphene transistors were extracted by numerical integration of the scanning photocurrent profiles along the dashed lines in Figure 4.11d and 4.11h.[139] The results in Figure 4.13a reveal that for the case with dehydrated retina, potential gradients of graphene only exist near the gold electrodes, which are induced by two back-to-back Schottky-like barriers at graphene-metal junction areas. These local electric fields can efficiently separate photo-excited EHPs and lead to strong photocurrent signals at the graphene-metal junction areas as shown in Figure 4.11h. The polarity of photocurrent responses depends on the direction in which the band bends. When the laser is scanning near the left electrode, separated electrons and holes will travel to the left and right electrodes, respectively. However, they will travel to opposite directions if the laser is scanning near right electrodes. Thus, the opposite signs of potential gradients determine the polarity of photocurrent response. A flat band region is formed in the middle of graphene between two electrodes, where the photo-excited EHPs quickly recombine and thus no strong photocurrent response is detected. In contrast, when a living retina is placed on top of a graphene transistor, the cell bodies of RGCs that have initiated action potentials along their axons can change the local electrochemical environments of the underneath graphene. As a result, the band structure of the graphene will be bent in the areas with neural activities since charged molecules and local potentials can modulate the carrier concentration of graphene and induce local potential gradients (the curved potential between the two electrodes in Figure 4.13b), which can promote separation of photo-excited EHPs and thus photocurrent generation. Different polarities of photocurrent signals are directly related to the bending directions of local potential. Moreover, the existence of the electrical double layer between graphene and the retina may shield the charged molecules when the layer thickness is beyond the Debye screening length.[140] Therefore, only the electrical activity in the regions (such as the ONH), which directly contact or are extremely close to the graphene transistors, can induce strong photocurrent signals in graphene.

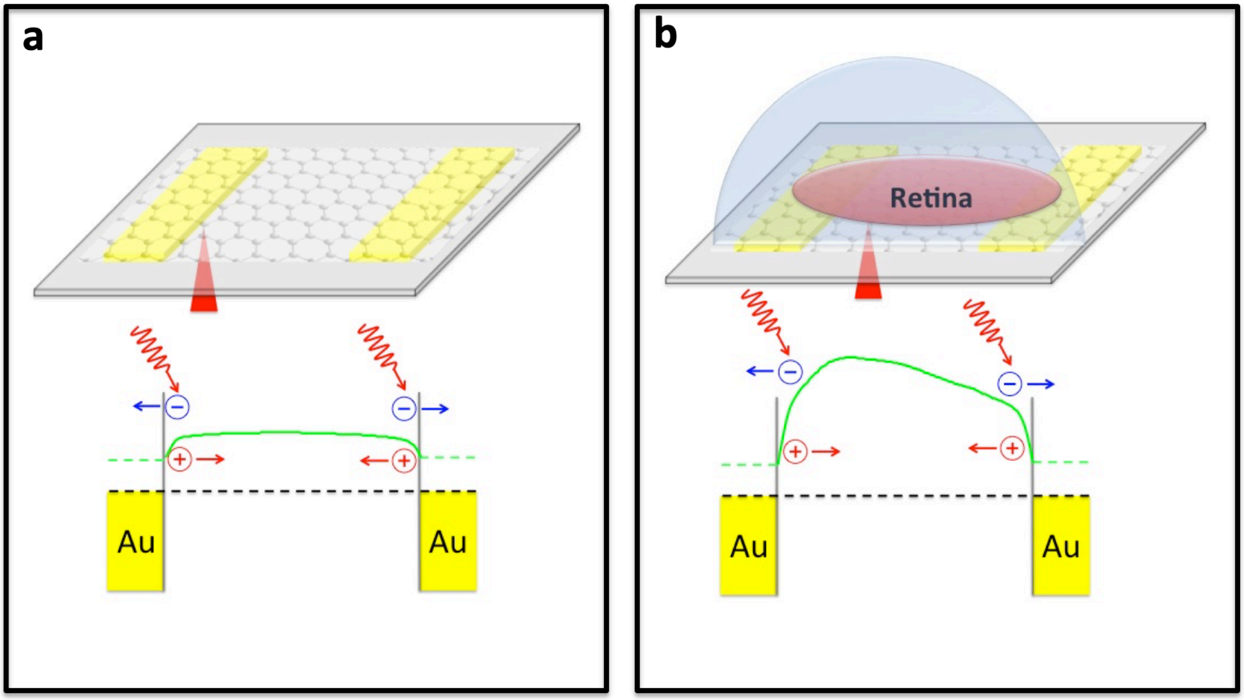

Figure 4.13 Schematic diagrams of band structures of a graphene transistor. (a) Photocurrent signals generate at graphene-metal junction areas due to the band structure bending. (b) A retina can modulate the carrier concentration of graphene underneath it. Green solid lines show potential profiles. Black dashed lines denote the Fermi levels. Note that in (a) and (b), the potential profiles are obtained through numerical integration of the scanning photocurrent profiles along the dashed lines in Figure 4.11h and d, respectively.

4.6 Conclusion

I examined the effect of graphene substrate for cell culture through comparing the outcomes of viability, vitality and electrophysiological function in primary cultures of RGCs on each of three common substrates (glass, laminin and PDL) with and without graphene overlay. I suspect that as a monolayer atomic structure, graphene reproduced local surface properties (mechanical or charge distribution) of underneath matrix to influence the cultured RGCs on top of it. Overall, our data suggest that while graphene does not alter the biophysical phenotype of RGCs, it does alter the way in which this phenotype is achieved. Although further studies are required to elucidate the cause of changes in ion channel expression and the underlying mechanism for increased cation channel activity, the identification of these graphene-dependent changes is important for interpretation of electrophysiological assays utilizing graphene as the biosensor. Our data indicates that, when the proper baselines are established, graphene is a promising biosensing material for *in vitro* applications in neuroscience, such as electrophysiological assays.

I further designed a graphene-integrated microfluidic platform to investigate the electrical activity in mouse retinal tissues through spatially-resolved scanning photocurrent measurements. Remarkable photocurrent signals are detected in the ONH, suggesting that the electrical activity of RGC axons in the ONH can module the carrier concentration, induce local potential gradients, and thus produce photocurrent signals in the graphene transistors. Importantly, as control experiments, I find that no significant photocurrent response is observed in graphene underneath both dehydrated and fixed retinal tissues, which further confirms that graphene-based scanning photocurrent microscopy is a promising technique to investigate electrical processes in living retina. This method also opens the door for investigating cellular interactions in other neural networks and biological systems.

Chapter 5 Flexible Graphene Probes for *in vitro* and *in vivo* Biological System Measurement

5.1 Introduction

The brain, as the center of the nervous system in all vertebrate animals, has the most complex structure in a body. The human brain contains more than 100 billion neurons, each of them is connected to thousands of other neurons via synapses.[141] The connectivity and network of such amounts of cells cooperate is still need to be elucidated. Acute brain slices are widely used to investigate the central nervous system because of relatively simple and efficient for preparation.[142] With easy access to the slices, the media can be precisely adjusted as desired and drugs can be perfused through the tissue.

Typically, researchers use the patch-clamp technique to study neurons in mouse brain slices, which cannot show the connectivity between cells in the slices. Thus, various types of MEA were developed, which are devices that contain arrays of plates or shanks as microelectrodes, provide interfaces to detect the neural activities of neurons/muscle cells, and study the signal propagation and connectivity.[143-145] From the application, MEA can be classified as *in intro*, which is for cell cultures, retina, and acute tissue slices, and *in vivo*, which are implantable devices, which are all based on microwire, silicon, or flexible polymer.[146-148] The flexible MEA outstands other groups because of their closer mechanical match to the tissue and non-invasive to the brain.[149, 150]

For *in vivo* microelectrode arrays (MEA), traditionally, three groups were developed, including microwire, silicon, and flexible arrays.[151-154] The materials for the first two groups are all rigid, which is difficult to have a close mechanical match with tissue and will also induce more inflammation than flexible sensors.[155] The cerebral cortex, as the largest site of neural integration in the central nervous system, acts a critical role in various functions such as perception, memory, thought, and attention.[156] The flexible MEA sensors can be attached to the surface of the cortex, and provide consistent recording for months. Based on the recording, with the potential for long-term in-plants as brain-computer interfaces, the device can be applied to explore the solutions for nervous system disorders, disorders of consciousness, motor recovery, and virtual reality, which are of great importance for future application.

Flexible electronics have attracted extensive interest for various applications, which have been extended to be stretchable and healable.[157] Various challenges should be considered to choose materials based on application. For many circumstances, substrates may be required to have a high bending radius, Young's modulus, chemical stability, compatible with the device fabrication process. Commercialized polymers that are commonly used to develop flexible devices include PDMS, parylene, polyethylene terephthalate (PET), polyimide (PI), and silicone. For example, researchers designed and fabricated neural implants to help restore locomotion of spinal cord injured rats based on silicone, which has similar mechanical properties with relative tissue (Figure 5.1a).[158] Electronic skin based on flexible strain, temperature, pressure, sensors, and MEA shows a unique opportunity for prostheses and peripheral nervous interface technologies (Figure 5.1b).[159] In addition, researchers developed biomimetic soft actuators are capable with various transformation, such as grippers with dielectric elastomer actuators (DEA) can control flexible, fragile and flat objects with interdigitated electrode geometry (Figure 5.1c).[160] Recent studies also show the potential of ionic hydrogel and ionic fluids as electrodes for DEAs, which have potentials in transparent soft swimming robots (Figure 5.1c).[161]

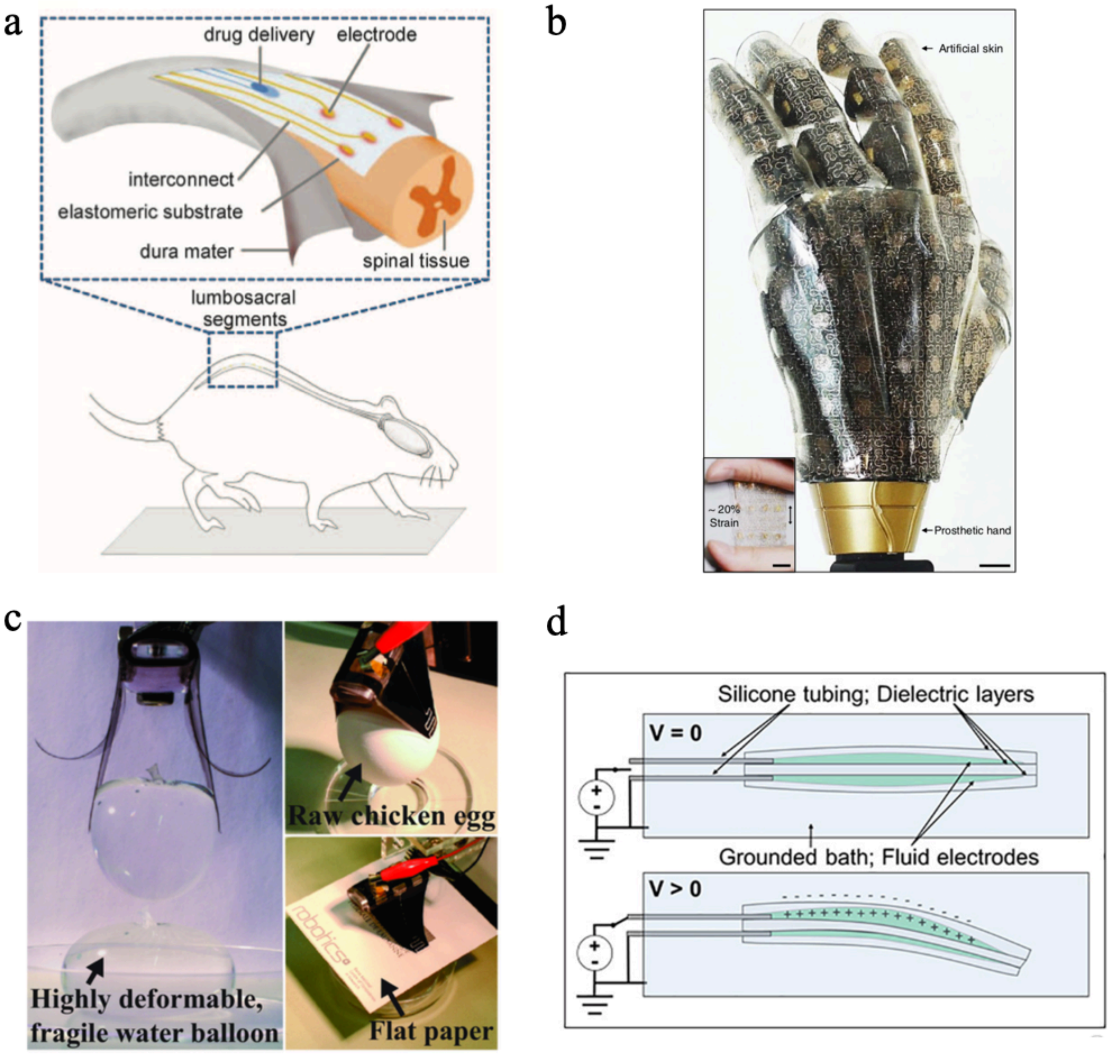

Figure 5.1 Flexible electronics in various applications. (a) Illustration of the e-dura implant inserted in the spinal subdural space of rats.[158] (b) Photograph of a representative smart artificial skin with integrated stretchable sensors and actuators covering the entire surface area of a prosthetic hand. Scale bar, 1 cm. The inset shows the artificial skin stretched ~20%. Scale bar, 1 cm.[159] (c) Soft grippers with a sandwich-like DEA structure can manipulate deformable, fragile, and even flat objects by employing a compliant interdigitated electrode geometry.[160] (d) Working principle of FEDEA bimorph module (not to scale): For bidirectional actuators, I make two DEAs from three layers of an acrylic elastomer adhesive. I created the active areas of the actuators by

selectively passivating the surfaces of the adhesive with a powder, which allowed the conductive fluid to enter from the tubing and cover the active area. I connected the actuator to the high voltage lead of the power supply through the silicone tubing. Application of a voltage in one of the fluid chambers with respect to the external fluid-induced Maxwell stress in the dielectric, inducing a bending motion away from the actuated side.[161]

Here, I demonstrate flexible perforated graphene probes for achieving close mechanical contact with optimized hole distribution. Graphene, with all the surfaces exposed to the environment, is expected to have higher sensitivity than traditional noble metal electrode arrays. Graphene probing fluid platform was designed to keep the tissue active and close mechanical contact to graphene probes, which has one inlet for medium supply, two outlets: one from the bottom for hold tissues contact with probes and one from the top for preventing overflood. The perfusion system and measurement setup have been tested with various perforated patterned devices for better contact between tissue and sensor region, which indicates uniformly distributed holes with around 20% through the area would be sufficient to provide a close contact.

Flexible graphene probes can also be applied for *in vivo* neural activity recording. Graphene, shows better performance comparing to gold electrodes, which also has been proved biocompatible after a long time implant.[148] Graphene transistors also feature less noise from intrinsic amplification of voltage-to-current, wide electrochemical window, high sensitivity because of extraordinary surface-to-volume ratio, and transparent nature, which can be combined with advanced microscopy techniques, such as scanning photocurrent microscopy, two-photon microscopy.[162-164]

5.2 Flexible graphene probing platform design

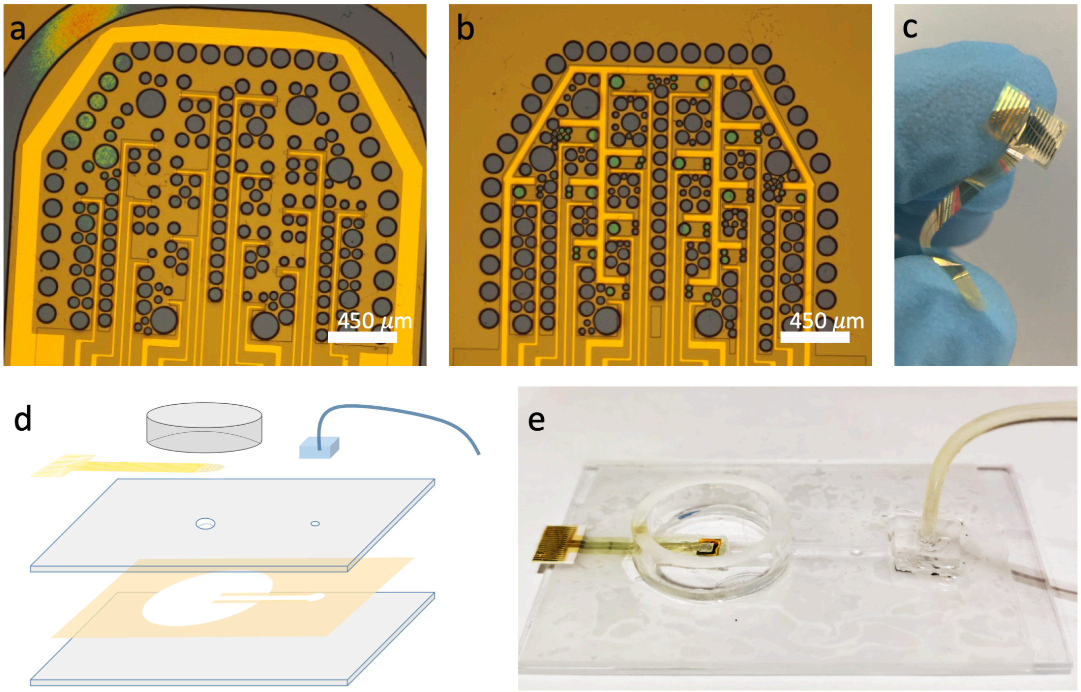

Figure 5.2 Design of flexible graphene probes. Optical micrographs of fabricated flexible graphene probes on Si/SiO$_2$ wafer with arrays of (a) electrode design and (b) transistor design. (c) Picture of a flexible graphene probe peeled off from a wafer. (d) Schematic graph of the exploded view of the probing platform. (e) Picture of an assembled probing platform.

Different probes are designed as arrays of electrode and transistor configurations. Arrays of 16 electrodes with 8 gold electrodes on the left and 8 graphene electrodes on the right (Figure 5.2a), as well as arrays of 16 graphene transistors (Figure 5.2b). Evenly distributed holes are around 23% area of the detection region, which help to achieve close mechanical contact and media perfusion of tissue. As a gentle vacuum pump providing negative pressure from the backside of sensors, media can perfuse through the tissue, which can hold the tissue in contact with electrodes and the chemical stimulus can reach the bottom surface touching the electrodes or transistors.

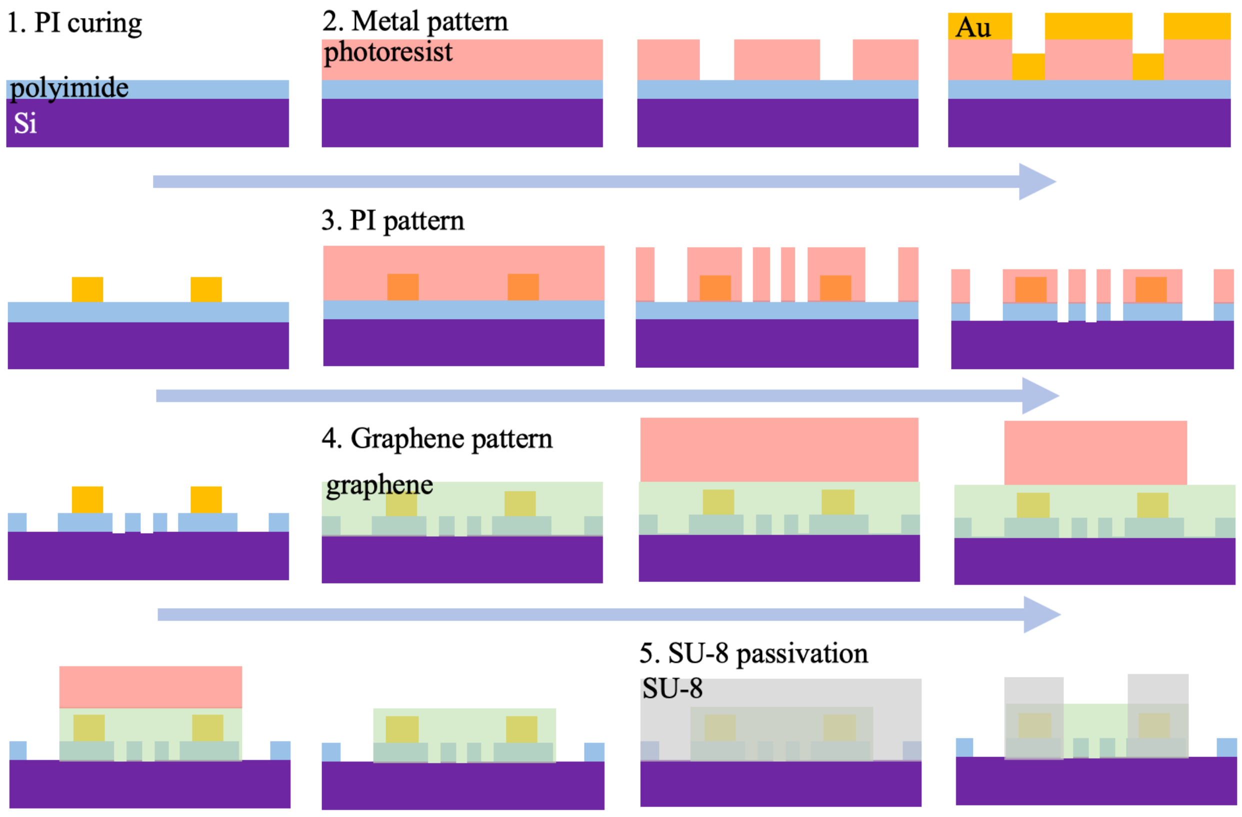

Figure 5.3 Fabrication process of flexible graphene probes.

The probing platform, consisting of two glass slides, parafilm, sensor film, PDMS tubing support, and glass ring, is shown in Figure 5.2d&e. To form a vacuum chamber, two holes were drilled on one of the glass slides and sandwiched a piece of parafilm to form a channel with another glass slide. The sensor film was then glued on the center hole region while the PDMS tubing support bonded to another hole. Finally, the glass ring was glued on the sensor film. Sensors film was fabricated as the following steps (Figure 5.3). First, I spin-coated 5 μm thick polyimide (PI-2611, HD Microsystems) on four-inch wafers and finished curing at 300° C. Electrodes were then defined via photolithography with a negative resist NR9-1000PY followed by e-beam deposition of the metal layer (Ti/Au, 10/100 nm). The polyimide film and holes were structured in a dry etching process via Trion Phantom II (O_2 94 sccm, CF_4 6 sccm, Pressure 200 mtorr) with patterned 10 μm thick SPR220-7.0 photoresist via photolithography as an etching mask. Graphene sheets, synthesized as previously described, were transferred to the desired areas. After removing the PMMA layer, I can continue the graphene transfer to guaranty optimal coverage. To achieve high-quality transfer, I applied an electrolysis method for separating PMMA-graphene from copper.[56] Typically, PMMA-graphene-copper is used as a cathode of an electrolytic cell with 0.25 M NaOH in deionized water and a platinum wire used as the anode. Supplying a small voltage of around 3.3V, the current will be a few milliamperes for a gentle separation. Gradually dipping the PMMA-graphene-copper deeper into the solution, PMMA-graphene will be easily detached from copper foil. This method brings a few advantages compared to using the copper etchant. Without the need for an overnight etching, it saves around 24 h process time for graphene transfer. The produced graphene can be cleaner compare to the copper etchant method and avoid the puzzling contamination on graphene from the copper etchant. In addition, the chemical used is easy to clean and environmental-friendly. The graphene active areas were then defined with O_2 plasma etching with S1805 photoresist as an etching mask. Finally, SU-8 2002 applied to passivate the device. The polyimide film can be easily peeled off from the wafer without any sacrifice layer. For the connection interfacing, a flexible flat cable (FFC) used as a substrate to support the connection area of the sensor film was clamped to a zero-insertion-force connector, which is on a lab-made printed circuit board for connecting to a 16-channel amplifier (RHD2132, Intan Technologies).

The assembled platform was then connected to a perfusion system, which has one inlet for providing media with an in-line heater controlling the temperate and two outlets for holding the tissue and preventing overflood. After the whole system was perfused with carbogen bubbled media for 1 hour at 2.0 mL/min with a peristaltic pump controlling the flow, then retina or recovered brain slices can be transferred in the well. The bottom outlet was started as 0.1 mL/min to hold the tissue. Neural data were recorded at a 20 kHz sampling rate from 16 channels simultaneously with Intan Recording System. Fresh artificial cerebrospinal fluid (ACSF) (NaCl 126 mM, KCl 2.5 mM, NaH_2PO_4 1.25 mM, $CaCl_2$ 2 mM, $MgCl_2$ 2 mM, $NaHCO_3$ 26 mM, glucose 10 mM) was made before each brain slices experiment with chemical stimuli: 30 mM K^+ ACSF (NaCl 98.5 mM, KCl 30 mM, NaH_2PO_4 1.25 mM, $CaCl_2$ 2 mM, $MgCl_2$ 2 mM, $NaHCO_3$ 26 mM, glucose 10 mM) and low Mg^{2+} ACSF (NaCl 126 mM, KCl 4.5 mM, NaH_2PO_4 1.25 mM, $CaCl_2$ 2 mM, $NaHCO_3$ 26 mM, glucose 10 mM). After bubbling with carbogen (95% O_2 / 5% CO_2) for 15 min, the media can be used for slice storage and measurement.

5.3 Flexible graphene transistors

After the device fabrication, I first tested the transfer curve and scanning photocurrent imaging of the graphene transistor devices. As shown in Figure 5.4a, a typical ambipolar transfer curve of graphene has a charge-neutrality point (CNP) ~0V, and the on-off ratio is ~2.6. The conductance shows a gradual decrease with the applied gated voltage increasing from -600 mV to CNP, and increase after that. The scanning photocurrent measurement was performed with 785 nm laser excitation. The laser beam was deflected by a nanometer-resolution scanning mirror and then focused by a 40× objective (N.A. = 0.6) into a diffraction-limited spot (∼1 μm) on graphene transistors. The photocurrent signals were collected using a preamplifier and the corresponding reflection image was recorded by a silicon detector. Strong scanning photocurrent signals were detected at the Metal/graphene contact area, as the Schottky-like barriers can efficiently separate the photo-excited electron-hole pairs and generate photocurrent. I can also collect photocurrent-induced voltage images via the Intan voltage amplifier.

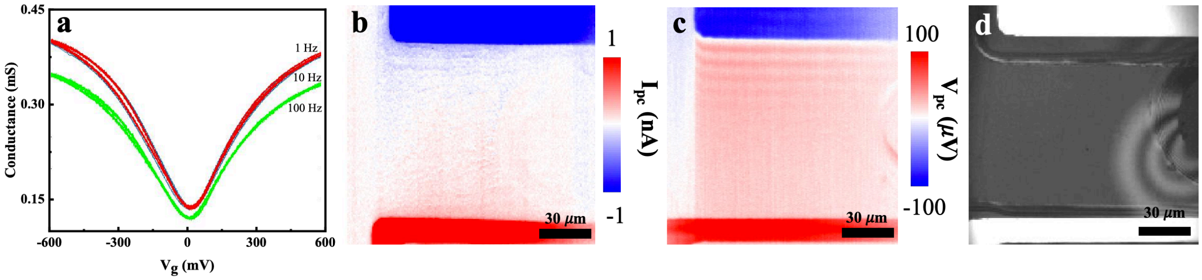

Figure 5.4 Characterization of flexible graphene transistor. (a) Transfer curve of an electrolyte gated flexible graphene transistor. Applied I_{sd} has various frequencies: 1 Hz and 10 Hz curves overlapped. (b) Scanning photocurrent image, (c) photocurrent induced voltage image, and (d) reflection image of a flexible graphene transistor.

5.4 Flexible graphene probes for *in vitro* recording

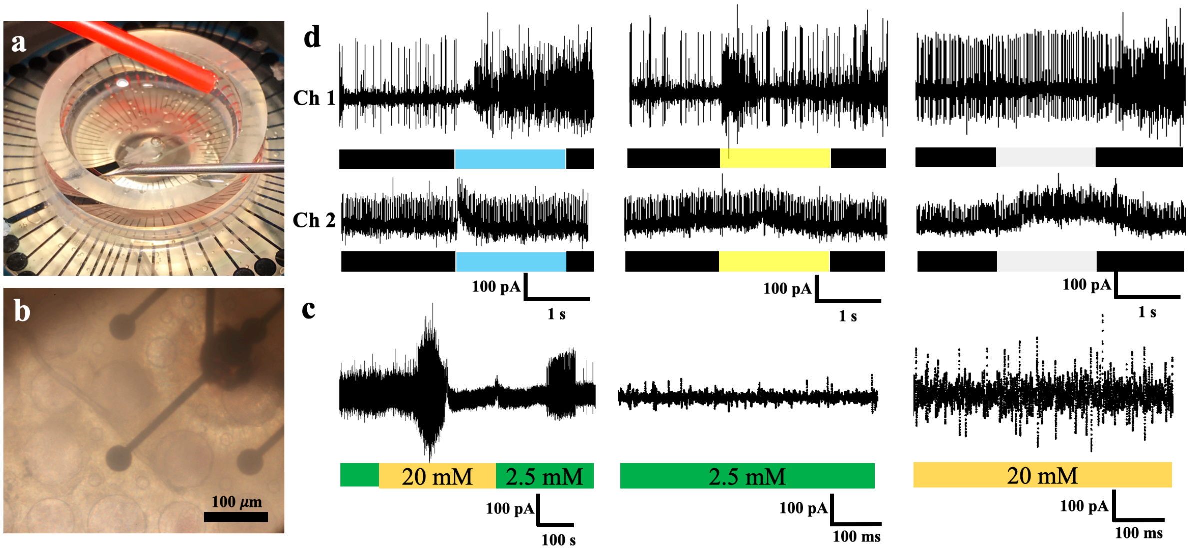

Figure 5.5 Measurement results of a retina. (a) Picture of a retina with a commercial MEA. (b) Optical image of a retina on top of a commercial MEA. 30 μm diameter dark circles with traces are arrays of electrode and an 80μm diameter dark circle in the top right corner is optical nerve head. (c) K^+ stimulation result shows frequency and amplitude difference between normal and high K^+ medium from the retina. The color bars show the perfusion time of the medium with different

K^+ concentrations. (d) Light stimulation results from two channels show typical responses under blue, yellow, and white light. The color bars show the on/off time of light with wavelength: blue, yellow, and white.

I first measured mice retina with a commercial MEA (60pMEA200/30iR-Ti, Multichannel Systems). As shown in Figure 5.5, a retina was placed at the center sensor region of the chamber, with a red tubbing for medium supply and a stainless-steel needle outlet for preventing overflood. A retina has continuous spontaneous spikes, which will increase the firing rate and amplitude with high potassium (K^+) concentration medium stimulation. The light stimulation was also performed to explore the responses from the retina with blue, yellow, and white illumination. The different cells in the retina respond to light show different patterns as ON-, OFF-cells for different wavelength and total brightness.[165, 166] Acute brain slices were also tested on commercial MEA, which show few spontaneous spikes without stimulation. As the high K^+ medium is delivered into the chamber, spikes can be detected.

Our flexible graphene probes were applied to measure the neural activity of brain slices. In figure 5.6, a piece of acute brain slice was placed on top of the sensor region, which has arrays of graphene and gold electrodes. Under the high K^+ stimulation, I detected a series of spikes from multiple electrodes. Especially, the graphene electrodes show higher amplitude than gold electrodes, because of the lower impedance of the probes compared to e-beam deposited gold electrodes, which demonstrates the performance of the flexible graphene probes.

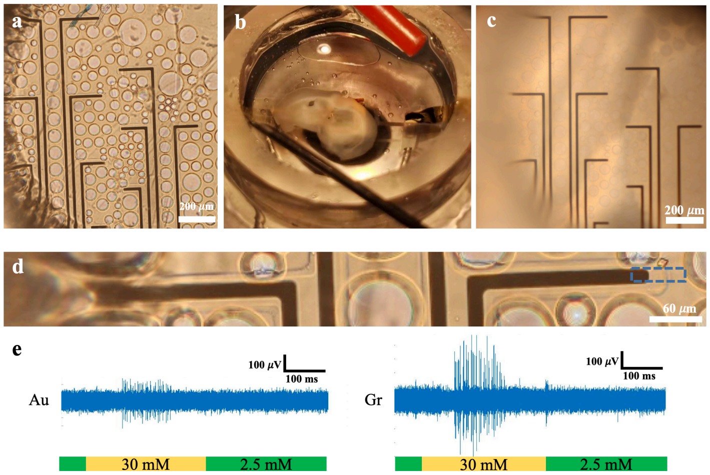

Figure 5.6 Flexible graphene probes for brain slices recording. (a) Optical image of a graphene probe with medium only. (b) Picture of a piece of brain slice in an assembled probing chamber. (c) Optical image of a piece of brain slice on the graphene probe. (d) Zoomed-in image of the graphene probe shows the detail of graphene electrode as the blue dashed line region. (e) K^+ stimulation results show the higher amplitude spikes detected from graphene electrode than gold. The color bar shows the perfusion time of the medium with different K^+ concentrations.

5.5 *In vivo* device implantation

After flexible graphene probes are fabricated, I can directly apply them as *in vivo* probes. Adult mice, used in our study, were anesthetized with diethyl ether, as shown in Figure 5.7. Once the animals were ready for the surgery, they were transferred on a thermal blanket to maintain at 37^o C with a stereotaxic frame, with ocular lubricant to the mouse's eyes for preventing dryness under anesthesia. A craniotomy was performed over the cortex for epicortical recordings. Using flexible flat cable (FFC) as a substrate to support the polyimide film, I can sterilize them together in ethanol before surgery. The flexible devices placed on the cortex surface will attach to the brain by themselves. The dental cement was applied to cover the FFC and part of the device, which will harden and secure the device on the skull. Mice were allowed to recover from anesthetized and recover for a week before the following recording. Lab-made printed-circuit boards will be connected for signal interfacing with a 16-channel amplifier (RHD2132, Intan Technologies) when mice are ready for recording.

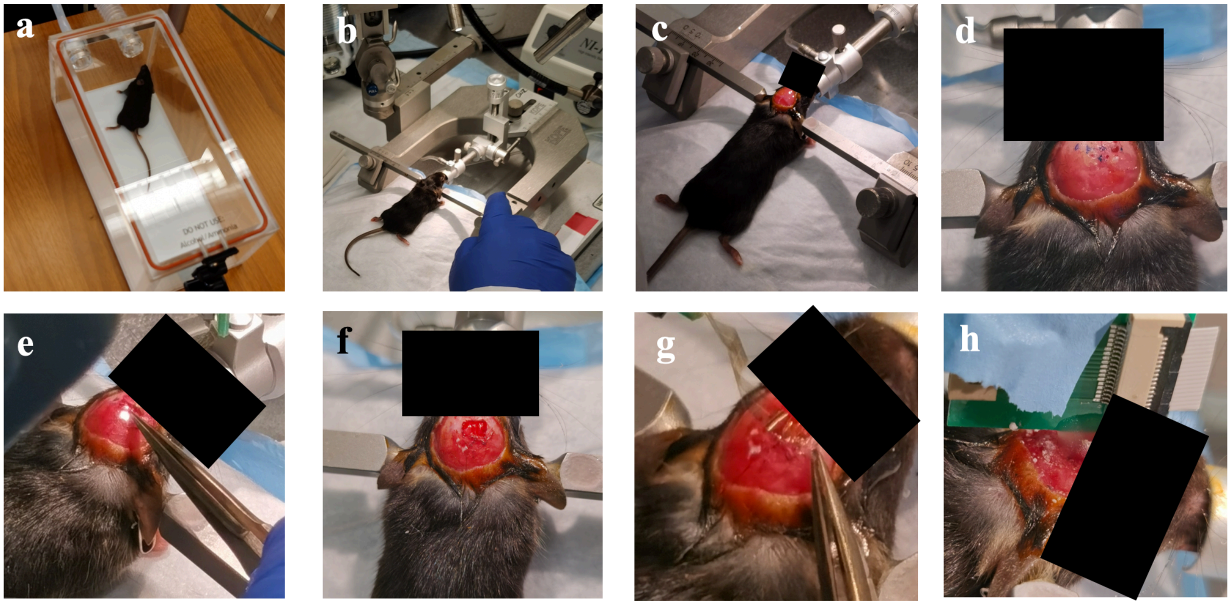

[redacted] [redacted] [redacted] [redacted] [redacted] [redacted]

Figure 5.7 Pictures of the implant surgery steps. (a) Anesthetize a mouse in a chamber with diethyl ether. (b) Mount the mouse on a stereotaxic frame with a thermal blanket underneath. (c, d) Remove fur and skin on the skull. (e, f) Open a 3 mm^2 hole on the skull. (g, h) Attach a graphene probe to the brain, and fix it to the skull with dental cement.

5.5 Conclusion

In this chapter, I demonstrated the process of flexible graphene probe fabrication, which can be applied for detecting neural activities *in vitro* and *in vivo*. Perforated graphene probes were fabricated on flexible polyimide substrates and integrated into a perfusion chamber for *in vitro* recording. I tested devices with different hole configurations and found that uniformly distributed holes with 20% area with a gentle flow can hold the tissue at the sensor area for achieving better mechanical contact than a rigid flat surface. Graphene electrodes show higher amplitude for detecting neural activities than gold electrode, which may because of the lower impedance of graphene electrodes than the e-beam deposited gold electrodes. *In vivo* neural activity detection is of great importance for future application on nervous system disorder, disorder of consciousness, motor recovery, and virtual reality. Our flexible graphene probes featured with the high sensitivity, biocompatibility, and close mechanical match are promising probes for a reliable long-term implant for *in vivo* experiments. The potential functionality can be further improved with graphene transistor configuration. Especially, combining with scanning photocurrent microscopy can help to achieve high spatiotemporal resolution.

Chapter 6 Summary and Outlook

6.1 Summary

From the groundbreaking discovery of graphene, 2D materials have attracted extensive researchers to explore their unique properties and potential applications. From the extraordinary mobility of graphene to superconducting twisted bilayer graphene, researchers are continuing to dive deep to study the basic properties of these materials as well as the industrial potentials. Thanks to the development of various techniques, I have seen a great opportunity for the application of 2D materials into the real world.

In the first chapter, I introduced the electronic, mechanical, and optoelectronic properties of graphene and TMDs. Various synthesis methods help researchers to study materials from different aspects and for diverse applications. From the general introduction about the application, 2D materials show great potential in electronics, optoelectronics, energy, environment, and biomedical fields. Chapter 2 shows the details in materials synthesis, basic device fabrication, and characterization. Micro-mechanical exfoliation is widely used to fabricate for proof of concept high-quality 2D devices. CVD and liquid phase exfoliation are high yield approaches for study various applications. Graphene transistors are fabricated via photolithography and characterized with Raman spectroscopy, electrical and scanning photocurrent measurements. I also introduced the fabrication of WSe_2 transistors via EBL and basic characterization with Raman spectroscopy. I discussed the WSe_2 devices in detail about anisotropic photocurrent response with systematic measurement and theoretical studies in chapter 3, which help to understand the basic property of TMDs.

From chapter 4, I started to explore the application of graphene in biomedical fields, especially biosensors for neural activity detection. Retina, with organized structure and light-sensitive, is an ideal target to study. I first accessed the effect of graphene as a culture substrate for primary RGCs growth, which shows the biocompatibility for cell culture and potential for biosensing. Then, a unique graphene probe is developed to detect retina activity. Strong photocurrent signals are detected at ONH, which indicated the electrical activity at ONH can modulate local graphene band structure, which can efficiently separate photoexcited electron-hole pairs. To improve the mechanical contact between tissue, in chapter 5, I discussed how to fabricate flexible graphene probes for *in vitro* detections as well as *in vivo* implants. The perforated graphene probes show promising results for neural activity recording.

6.2 Outlook

I have seen the success of graphene in biomedical applications. However, it can be further improved to achieve high spatiotemporal resolution for both *in vitro* and *in vivo* recording with a graphene transistor configuration. With well-developed graphene biosensors, combining with scanning photocurrent microscopy, I can investigate the complex network of retina and brain in detail, which may change the traditional electrophysiology approaches in studying various diseases and drug development.

I can also explore the non-invasive graphene techniques for neural activity detection or stimulation, which can be of great importance for future brain-computer interfaces, which can be applied for motor or consciousness recovery. Beyond graphene, many other 2D materials with potential for flexible device application can be integrated together to form multifunction optoelectronic probes. Current studies have shown the potential of 2D materials in all kinds of applications. With the development of nanotechnology and the synthesis of materials, 2D materials devices have the potential to achieve industrial production and are utilized in assorted applications.

APPENDIX

A.1 Recipe of CVD Graphene Growth

1. Make sure flammable gases are ready to use.

2. Cut a piece of Cu foil.

3. Put the foil in a 5% nitric acid bath for 10 min, and three deionized water baths for 5 min each.

4. Gently dry the cleaned foil with nitrogen gun in a clean dish.

5. Load the dry foil into a cleaned loading boat, and insert into tube furnace.

6. Connect the tube furnace with upstream gas line and exhaust. Make sure a good sealing with vacuum gun.

7. Start the vacuum pump. Normally, It will reach target vaccum level in 30 min.

8. Record the starting pressure and humidity. Start flow 0.2 slm Ar for 5 min and start 200 sccm H_2 flow.

9. Turn off Ar flow, close the furnace and turn it on. Set the temperature to 950^o C for 1 h.

10. After 1 h annealing, reduce the flow rate of H_2 to 100 sccm, and start flow 30 sccm CH_4.

11. After 30 min, remove the boar out of the hot zone with a magnetic bar, turn off furnace, start 0.2 slm Ar flow and stop CH_4 flow.

12. Open the furnace with a small disk for cooling down the furnace. Completely open the furnace after temperate below 400^o C.

13. Turn off pump when the temperate is below 200^o C. Loose the cap at the downstream.

14. Stop Ar flow when the pressure push the cap out.

15. Take the boat out and put the graphene/Cu in a clean petri-dish.

16. Take Raman spectroscopy to make sure the graphene growth quality.

A.2 Estimation of Local Potential Changes via Photocurrent Measurement

As photocurrent signals are proportional to the local potential gradients, I can extract band diagrams ($E_F - E_{Dirac}$) of graphene through numerical integration of photocurrent profiles.[58, 59] Based on a simple capacitor model, I obtained an expression for the energetic difference $\Delta E = E_F - E_{Dirac} \approx \hbar v_F \sqrt{\pi n} = \hbar v_F \sqrt{\pi \frac{C}{e} \left| V_g - V_{Dirac} \right|}$, where $v_F \approx 10^6\ m/s$ is the Fermi velocity, n is the charge carrier concentration, and C is the combination of the electrostatic capacitance between a graphene and a synapse/spine and the quantum capacitance of the graphene.[60] The minimum quantum capacitance $C_{Q,min}$is about 6.5 $\mu F/cm^2$,[167] and the double layer capacitance of the electrolyte C_i is approximately $20\ \mu F/cm^2$.[168] Thus, the total capacitance C is ~ 4.9 $\mu F/cm^2$.

As described in chapter 2, from electrical transport measurement and scanning photocurrent measurement, I can estimate the constant energetic offset at the graphene-electrode contacts: $\phi_{FB} = \Delta E\left(V_g = V_{FB}\right) \approx 0.1067\ eV$.

On the other hand, I can extract the band diagrams by numerical integration from the photocurrent profiles across the drain and source electrodes (Figure A1 A&B). The integrated difference across the drain and source is $\Delta\phi_{PC}^{Global} \approx 2.4880$, corresponding to the energetic difference $\Delta E\left(V_g = V_g^{Global} = 0\right) \approx 0.4864\ eV$. Based on this relationship, I can calculate the local energetic difference induced by neurons. Figure A1 D&F show the photocurrent measurements of a typical graphene-synapse junction (blue circle in figure A1H) at rest (4 mM K$^+$) and during depolarization (60 mM K$^+$), respectively. As illustrated in Fig. A1F (G), the local integrated difference of the graphene-synapse at rest (during depolarization) is $\Delta\phi_{PC}^{4\ mM} \approx 0.0460$ ($\Delta\phi_{PC}^{60\ mM} \approx$ 0.0430), corresponding to an energetic difference of $\Delta E^{4\ mM} \approx 0.4954\ eV$

($\Delta E^{60\ mM} \approx 0.4948\ eV$). I then calculate the local carrier concentration $n = \left(\frac{\Delta E}{\hbar v_F}\right)^2/\pi$ and derive a local carrier concentration change of $\sim 6.7 \times 10^{10}\ cm^{-2}$, corresponding to a local potential change of $\sim 2\ mV$.

Similarly, I can estimate the local potential change from the temporal photocurrent measurements, where I assume the integrated difference is proportional to the photocurrent intensity, which is illustrated in our spatial photocurrent measurements (Figure A1).

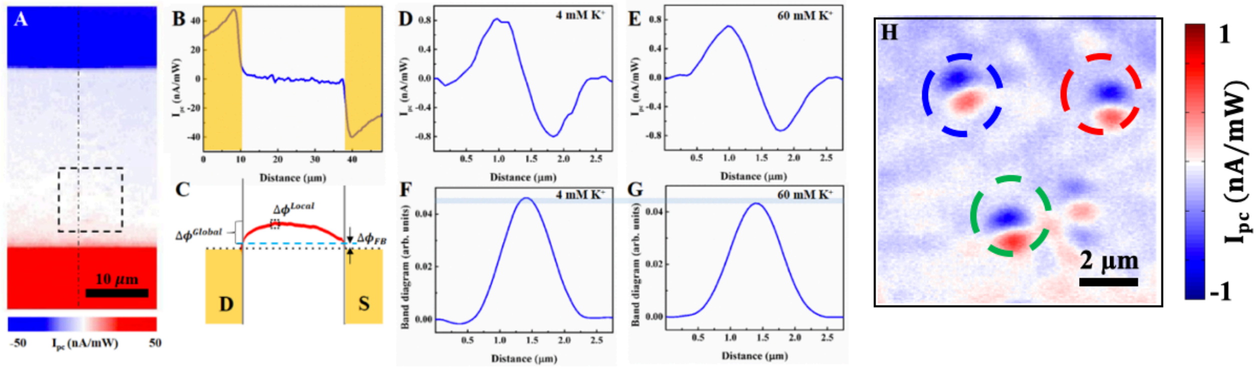

Figure A1 Estimation of local potential change. (A) Photocurrent image of a graphene transistor underneath neurons. (B) Photocurrent profile and (C) integrated difference along the dashed line in (A). The yellow shaded regions indicate Au electrodes. Photocurrent profiles and integrated difference in 4 mM K$^+$ (D, F) and 60 mM K$^+$ media (E, G) of a graphene-synapse junction circled by a black line in (C) and a blue line in (E). (H) Scanning photocurrent image of neurons on top of a graphene transistor.

A.3 Flexible Device fabrication

1. Clean a wafer with Acetone bath and IPA rinse for 30s.

2. Spin coat 5 μm polyimide (PI-2611, HD Microsystems) on the clean four-inch wafers.

3. Start the curing process from 70° C on hot plate, and slowly increase to 160° C. Then take the wafer to an oven to continue curing, gradually increase the temperature from 160° C to 300° C. Hold at 300° C for 30 min and turn off oven, gradually cool down the wafer.

4. Metal contact pattern is defined via photolithography with a negative resist NR9-1000PY. You may treat the surface with O_2 plasma before spin-coating.

5. After develop the pattern, and nitrogen dry the wafer. Hold the wafer at 200° C oven until the following steps.

6. E-beam deposit a layer metal (Ti/Au, 10/100 nm). Lift-off with Acetone, then IPA rinse, Nitrogen dry.

7. Spin coat 10 μm thick SPR220-7.0 photoresist via photolithography as an etching mask. You may treat the surface via HMDS process. Make sure waiting for enough time during the relax process.

8. The polyimide film and holes were structured via a dry etching process via Trion Phantom II (O_2 94 sccm, CF_4 6 sccm, Pressure 200 mtorr)

9. Graphene sheets, synthesized as previously described, were transferred on the desired areas. After removing the PMMA layer, continue the graphene transfer to guaranty an optimal coverage for around 4 layers

10. Spin coat ~500 nm thick S1805 photoresist as etching mask for graphene pattern. After photolithography, graphene active areas were then defined with O_2 plasma etching

11. Spin coat 2 μm thick SU-8 2002. Passivate the device via photolithography.

12. The polyimide film can be easily peeled off from the wafer with a pair of fine tweezers.

REFERENCES

1. Geim, A. K.; Novoselov, K. S., The rise of graphene. *Nature Materials* **2007,** *6* (3), 183-191.

2. Ling, X.; Wang, H.; Huang, S.; Xia, F.; Dresselhaus, M. S., The renaissance of black phosphorus. *Proceedings of the National Academy of Sciences* **2015,** *112* (15), 4523-4530.

3. Lee, C.; Wei, X.; Kysar, J. W.; Hone, J., Measurement of the Elastic Properties and Intrinsic Strength of Monolayer Graphene. *Science* **2008,** *321* (5887), 385-388.

4. Ni, Z. H.; Yu, T.; Lu, Y. H.; Wang, Y. Y.; Feng, Y. P.; Shen, Z. X., Uniaxial strain on graphene: Raman spectroscopy study and band-gap opening. *ACS nano* **2008,** *2* (11), 2301-2305.

5. Balog, R.; Jørgensen, B.; Nilsson, L.; Andersen, M.; Rienks, E.; Bianchi, M.; Fanetti, M.; Lægsgaard, E.; Baraldi, A.; Lizzit, S., Bandgap opening in graphene induced by patterned hydrogen adsorption. *Nature Materials* **2010,** *9* (4), 315-319.

6. Cao, Y.; Fatemi, V.; Fang, S.; Watanabe, K.; Taniguchi, T.; Kaxiras, E.; Jarillo-Herrero, P., Unconventional superconductivity in magic-angle graphene superlattices. *Nature* **2018,** *556* (7699), 43-50.

7. Schwierz, F., Graphene transistors. *Nat Nano* **2010,** *5* (7), 487-496.

8. Liao, L.; Lin, Y.-C.; Bao, M.; Cheng, R.; Bai, J.; Liu, Y.; Qu, Y.; Wang, K. L.; Huang, Y.; Duan, X., High-speed graphene transistors with a self-aligned nanowire gate. *Nature* **2010,** *467* (7313), 305-308.

9. Britnell, L.; Gorbachev, R. V.; Geim, A. K.; Ponomarenko, L. A.; Mishchenko, A.; Greenaway, M. T.; Fromhold, T. M.; Novoselov, K. S.; Eaves, L., Resonant tunnelling and negative differential conductance in graphene transistors. **2013,** *4*, 1794.

10. Zhang, B. Y.; Liu, T.; Meng, B.; Li, X.; Liang, G.; Hu, X.; Wang, Q. J., Broadband high photoresponse from pure monolayer graphene photodetector. **2013,** *4*, 1811.

11. Xia, F.; Mueller, T.; Lin, Y.-m.; Valdes-Garcia, A.; Avouris, P., Ultrafast graphene photodetector. *Nat Nano* **2009,** *4* (12), 839-843.

12. Bonaccorso, F.; Sun, Z.; Hasan, T.; Ferrari, A. C., Graphene photonics and optoelectronics. *Nat Photon* **2010,** *4* (9), 611-622.

13. Mak, K. F.; Shan, J., Photonics and optoelectronics of 2D semiconductor transition metal dichalcogenides. *Nat Photon* **2016,** *10* (4), 216-226.

14. Wang, Q. H.; Kalantar-Zadeh, K.; Kis, A.; Coleman, J. N.; Strano, M. S., Electronics and optoelectronics of two-dimensional transition metal dichalcogenides. *Nat Nano* **2012,** *7* (11), 699-712.

15. Zhang, Y.; Chang, T.-R.; Zhou, B.; Cui, Y.-T.; Yan, H.; Liu, Z.; Schmitt, F.; Lee, J.; Moore, R.; Chen, Y.; Lin, H.; Jeng, H.-T.; Mo, S.-K.; Hussain, Z.; Bansil, A.; Shen, Z.-X., Direct observation of the transition from indirect to direct bandgap in atomically thin epitaxial MoSe2. *Nature Nanotechnology* **2013,** *9*, 111-115.

16. Zhao, W.; Ribeiro, R. M.; Toh, M.; Carvalho, A.; Kloc, C.; Castro Neto, A. H.; Eda, G., Origin of Indirect Optical Transitions in Few-Layer MoS2, WS2, and WSe2. *Nano Letters* **2013,** *13* (11), 5627-5634.

17. Gusakova, J.; Wang, X.; Shiau, L. L.; Krivosheeva, A.; Shaposhnikov, V.; Borisenko, V.; Gusakov, V.; Tay, B. K., Electronic Properties of Bulk and Monolayer TMDs: Theoretical Study Within DFT Framework (GVJ-2e Method). *physica status solidi (a)* **2017,** *214* (12), 1700218.

18. Ye, Y.; Xiao, J.; Wang, H.; Ye, Z.; Zhu, H.; Zhao, M.; Wang, Y.; Zhao, J.; Yin, X.; Zhang, X., Electrical generation and control of the valley carriers in a monolayer transition metal dichalcogenide. *Nature Nanotechnology* **2016,** *11* (7), 598-602.

19. Plechinger, G.; Nagler, P.; Arora, A.; Schmidt, R.; Chernikov, A.; Del Águila, A. G.; Christianen, P. C.; Bratschitsch, R.; Schüller, C.; Korn, T., Trion fine structure and coupled spin–valley dynamics in monolayer tungsten disulfide. *Nature Communications* **2016,** *7*, 12715.

20. Kim, J.; Jin, C.; Chen, B.; Cai, H.; Zhao, T.; Lee, P.; Kahn, S.; Watanabe, K.; Taniguchi, T.; Tongay, S., Observation of ultralong valley lifetime in WSe2/MoS2 heterostructures. *Science advances* **2017,** *3* (7), e1700518.

21. Klein, J.; Wierzbowski, J.; Regler, A.; Becker, J.; Heimbach, F.; Müller, K.; Kaniber, M.; Finley, J. J., Stark effect spectroscopy of mono-and few-layer MoS2. *Nano Letters* **2016,** *16* (3), 1554-1559.

22. Roch, J. G.; Leisgang, N.; Froehlicher, G.; Makk, P.; Watanabe, K.; Taniguchi, T.; Schönenberger, C.; Warburton, R. J., Quantum-Confined Stark Effect in a MoS2 Monolayer van der Waals Heterostructure. *Nano Letters* **2018,** *18* (2), 1070-1074.

23. Massicotte, M.; Vialla, F.; Schmidt, P.; Lundeberg, M. B.; Latini, S.; Haastrup, S.; Danovich, M.; Davydovskaya, D.; Watanabe, K.; Taniguchi, T., Dissociation of two-dimensional excitons in monolayer WSe 2. *Nature Communications* **2018,** *9* (1), 1633.

24. Miller, D. A.; Chemla, D.; Damen, T.; Gossard, A.; Wiegmann, W.; Wood, T.; Burrus, C., Band-edge electroabsorption in quantum well structures: The quantum-confined Stark effect. *Physical Review Letters* **1984,** *53* (22), 2173.

25. Takao, Y.; Asahina, H.; Morita, A., Electronic structure of black phosphorus in tight binding approach. *Journal of the Physical Society of Japan* **1981,** *50* (10), 3362-3369.

26. Yi, M.; Shen, Z., A review on mechanical exfoliation for the scalable production of graphene. *Journal of Materials Chemistry A* **2015,** *3* (22), 11700-11715.

27. Hernandez, Y.; Nicolosi, V.; Lotya, M.; Blighe, F. M.; Sun, Z.; De, S.; McGovern, I.; Holland, B.; Byrne, M.; Gun'Ko, Y. K., High-yield production of graphene by liquid-phase exfoliation of graphite. *Nature Nanotechnology* **2008,** *3* (9), 563.

28. Murugan, C.; Sharma, V.; Murugan, R. K.; Malaimegu, G.; Sundaramurthy, A., Two-dimensional cancer theranostic nanomaterials: Synthesis, surface functionalization and applications in photothermal therapy. *Journal of Controlled Release* **2019,** *299*, 1-20.

29. Whittingham, M. S.; Gamble, F. R., The lithium intercalates of the transition metal dichalcogenides. *Materials Research Bulletin* **1975,** *10* (5), 363-371.

30. Wu, X., *Influence of Particle Beam Irradiation on the Structure and Properties of Graphene*. Springer: 2017.

31. Tian, H.; Ren, T.-L.; Xie, D.; Wang, Y.-F.; Zhou, C.-J.; Feng, T.-T.; Fu, D.; Yang, Y.; Peng, P.-G.; Wang, L.-G., Graphene-on-paper sound source devices. *ACS nano* **2011,** *5* (6), 4878-4885.

32. Smith, A.; Niklaus, F.; Paussa, A.; Vaziri, S.; Fischer, A. C.; Sterner, M.; Forsberg, F.; Delin, A.; Esseni, D.; Palestri, P., Electromechanical piezoresistive sensing in suspended graphene membranes. *Nano letters* **2013,** *13* (7), 3237-3242.

33. Hosseinzadegan, H.; Todd, C.; Lal, A.; Pandey, M.; Levendorf, M.; Park, J. In *Graphene has ultra high piezoresistive gauge factor*, 2012 IEEE 25th international conference on micro electro mechanical systems (MEMS), IEEE: 2012; pp 611-614.

34. Cohen-Tanugi, D.; Grossman, J. C., Water desalination across nanoporous graphene. *Nano letters* **2012,** *12* (7), 3602-3608.

35. Jiang, D.-e.; Cooper, V. R.; Dai, S., Porous graphene as the ultimate membrane for gas separation. *Nano letters* **2009,** *9* (12), 4019-4024.

36. O'Hern, S. C.; Boutilier, M. S.; Idrobo, J.-C.; Song, Y.; Kong, J.; Laoui, T.; Atieh, M.; Karnik, R., Selective ionic transport through tunable subnanometer pores in single-layer graphene membranes. *Nano letters* **2014,** *14* (3), 1234-1241.

37. Bell, D. C.; Lemme, M. C.; Stern, L. A.; Williams, J. R.; Marcus, C. M., Precision cutting and patterning of graphene with helium ions. *Nanotechnology* **2009,** *20* (45), 455301.

38. Fischbein, M. D.; Drndić, M., Electron beam nanosculpting of suspended graphene sheets. *Applied Physics Letters* **2008,** *93* (11), 113107.

39. Chen, J.-H.; Jang, C.; Xiao, S.; Ishigami, M.; Fuhrer, M. S., Intrinsic and extrinsic performance limits of graphene devices on SiO2. *Nature Nanotechnology* **2008,** *3* (4), 206-209.

40. Liu, Z.; Robinson, J. T.; Tabakman, S. M.; Yang, K.; Dai, H., Carbon materials for drug delivery & cancer therapy. *Materials today* **2011,** *14* (7-8), 316-323.

41. Dong, X.; Shi, Y.; Huang, W.; Chen, P.; Li, L.-J., Electrical Detection of DNA Hybridization with Single-Base Specificity Using Transistors Based on CVD-Grown Graphene Sheets. *Advanced Materials* **2010,** *22* (14), 1649-1653.

42. Stine, R.; Robinson, J. T.; Sheehan, P. E.; Tamanaha, C. R., Real-Time DNA Detection Using Reduced Graphene Oxide Field Effect Transistors. *Advanced Materials* **2010,** *22* (46), 5297-5300.

43. Fan, H.; Wang, L.; Zhao, K.; Li, N.; Shi, Z.; Ge, Z.; Jin, Z., Fabrication, Mechanical Properties, and Biocompatibility of Graphene-Reinforced Chitosan Composites. *Biomacromolecules* **2010,** *11* (9), 2345-2351.

44. Choi, W.; Choudhary, N.; Han, G. H.; Park, J.; Akinwande, D.; Lee, Y. H., Recent development of two-dimensional transition metal dichalcogenides and their applications. *Materials today* **2017,** *20* (3), 116-130.

45. Radisavljevic, B.; Radenovic, A.; Brivio, J.; Giacometti, V.; Kis, A., Single-layer MoS2 transistors. *Nature Nanotechnology* **2011,** *6* (3), 147-150.

46. Yin, Z.; Li, H.; Li, H.; Jiang, L.; Shi, Y.; Sun, Y.; Lu, G.; Zhang, Q.; Chen, X.; Zhang, H., Single-Layer MoS2 Phototransistors. *ACS nano* **2012,** *6* (1), 74-80.

47. Kim, S.-S.; Lee, J.-W.; Yun, J.-M.; Na, S.-I., 2-Dimensional MoS2 nanosheets as transparent and highly electrocatalytic counter electrode in dye-sensitized solar cells: Effect of thermal treatments. *Journal of Industrial and Engineering Chemistry* **2015,** *29*, 71-77.

48. Tang, H.; Wang, J.; Yin, H.; Zhao, H.; Wang, D.; Tang, Z., Growth of Polypyrrole Ultrathin Films on MoS2 Monolayers as High-Performance Supercapacitor Electrodes. *Advanced Materials* **2015,** *27* (6), 1117-1123.

49. Zhu, H.; Wang, Y.; Xiao, J.; Liu, M.; Xiong, S.; Wong, Z. J.; Ye, Z.; Ye, Y.; Yin, X.; Zhang, X., Observation of piezoelectricity in free-standing monolayer MoS2. *Nature Nanotechnology* **2015,** *10* (2), 151-155.

50. Yin, W.; Yan, L.; Yu, J.; Tian, G.; Zhou, L.; Zheng, X.; Zhang, X.; Yong, Y.; Li, J.; Gu, Z.; Zhao, Y., High-Throughput Synthesis of Single-Layer MoS2 Nanosheets as a Near-Infrared Photothermal-Triggered Drug Delivery for Effective Cancer Therapy. *ACS nano* **2014,** *8* (7), 6922-6933.

51. Sheng, Z.; Song, L.; Zheng, J.; Hu, D.; He, M.; Zheng, M.; Gao, G.; Gong, P.; Zhang, P.; Ma, Y.; Cai, L., Protein-assisted fabrication of nano-reduced graphene oxide for combined in vivo photoacoustic imaging and photothermal therapy. *Biomaterials* **2013,** *34* (21), 5236-5243.

52. Cheng, L.; Liu, J.; Gu, X.; Gong, H.; Shi, X.; Liu, T.; Wang, C.; Wang, X.; Liu, G.; Xing, H.; Bu, W.; Sun, B.; Liu, Z., PEGylated WS2 Nanosheets as a Multifunctional Theranostic Agent for in vivo Dual-Modal CT/Photoacoustic Imaging Guided Photothermal Therapy. *Advanced Materials* **2014,** *26* (12), 1886-1893.

53. Zhu, C.; Zeng, Z.; Li, H.; Li, F.; Fan, C.; Zhang, H., Single-Layer MoS2-Based Nanoprobes for Homogeneous Detection of Biomolecules. *Journal of the American Chemical Society* **2013,** *135* (16), 5998-6001.

54. Wang, L.; Wang, Y.; Wong, J. I.; Palacios, T.; Kong, J.; Yang, H. Y., Functionalized MoS2 Nanosheet-Based Field-Effect Biosensor for Label-Free Sensitive Detection of Cancer Marker Proteins in Solution. *Small* **2014,** *10* (6), 1101-1105.

55. Li, X. S.; Cai, W. W.; An, J. H.; Kim, S.; Nah, J.; Yang, D. X.; Piner, R.; Velamakanni, A.; Jung, I.; Tutuc, E.; Banerjee, S. K.; Colombo, L.; Ruoff, R. S., Large-Area Synthesis of High-Quality and Uniform Graphene Films on Copper Foils. *Science* **2009,** *324* (5932), 1312-1314.

56. Rosa, C. J. L. d. l.; Sun, J.; Lindvall, N.; Cole, M. T.; Nam, Y.; Löffler, M.; Olsson, E.; Teo, K. B. K.; Yurgens, A., Frame assisted H2O electrolysis induced H2 bubbling transfer of large area graphene grown by chemical vapor deposition on Cu. *Applied Physics Letters* **2013,** *102* (2), 022101.

57. Ferrari, A. C.; Basko, D. M., Raman spectroscopy as a versatile tool for studying the properties of graphene. *Nature Nanotechnology* **2013,** *8* (4), 235-246.

58. Mueller, T.; Xia, F.; Freitag, M.; Tsang, J.; Avouris, P., Role of contacts in graphene transistors: A scanning photocurrent study. *Physical Review B* **2009,** *79* (24).

59. Zhang, Y.; Dodson, K. H.; Fischer, R.; Wang, R.; Li, D.; Sappington, R. M.; Xu, Y.-Q., Probing electrical signals in the retina via graphene-integrated microfluidic platforms. *Nanoscale* **2016**.

60. Das Sarma, S.; Adam, S.; Hwang, E. H.; Rossi, E., Electronic transport in two-dimensional graphene. *Reviews of Modern Physics* **2011,** *83* (2), 407-470.

61. Tonndorf, P.; Schmidt, R.; Böttger, P.; Zhang, X.; Börner, J.; Liebig, A.; Albrecht, M.; Kloc, C.; Gordan, O.; Zahn, D. R. T.; Michaelis de Vasconcellos, S.; Bratschitsch, R., Photoluminescence emission and Raman response of monolayer MoS2, MoSe2, and WSe2. *Optics Express* **2013,** *21* (4), 4908-4916.

62. Xiao, D.; Liu, G.-B.; Feng, W.; Xu, X.; Yao, W., Coupled spin and valley physics in monolayers of MoS 2 and other group-VI dichalcogenides. *Physical review letters* **2012,** *108* (19), 196802.

63. Zakharchenya, B. P.; Mirlin, D. N.; Perel', V.; Reshina, I., Spectrum and polarization of hot-electron photoluminescence in semiconductors. *Physics-Uspekhi* **1982,** *25* (3), 143-166.

64. Peng, X. Y.; Zhang, Q.; Shen, B.; Shi, J. R.; Yin, C. M.; He, X. W.; Xu, F. J.; Wang, X. Q.; Tang, N.; Jiang, C. Y.; Chen, Y. H.; Chang, K., Anomalous linear photogalvanic effect observed in a GaN-based two-dimensional electron gas. *Physical Review B* **2011,** *84* (7), 075341.

65. Zhang, Y.; Xu, Y.-Q., Optical Momentum Alignment Effect in WSe2 Phototransistor. *Advanced Optical Materials 2021*, 2002243.

66. Zhao, W. J.; Ghorannevis, Z.; Chu, L. Q.; Toh, M. L.; Kloc, C.; Tan, P. H.; Eda, G., Evolution of Electronic Structure in Atomically Thin Sheets of WS2 and WSe2. *Acs Nano* **2013,** *7* (1), 791-797.

67. Saroka, V.; Hartmann, R.; Portnoi, M., Momentum alignment and the optical valley Hall effect in low-dimensional Dirac materials. *arXiv preprint arXiv:1811.00987* **2018**.

68. Hong, T.; Chamlagain, B.; Hu, S.; Weiss, S. M.; Zhou, Z.; Xu, Y.-Q., Plasmonic hot electron induced photocurrent response at MoS2–metal junctions. *ACS nano* **2015,** *9* (5), 5357-5363.

69. Zhang, W.; Huang, J. K.; Chen, C. H.; Chang, Y. H.; Cheng, Y. J.; Li, L. J., High-gain phototransistors based on a CVD MoS2 monolayer. *Advanced materials* **2013,** *25* (25), 3456-3461.

70. González-Posada, F.; Songmuang, R.; Den Hertog, M.; Monroy, E., Room-temperature photodetection dynamics of single GaN nanowires. *Nano Letters* **2011,** *12* (1), 172-176.

71. Mohite, A. D.; Gopinath, P.; Shah, H. M.; Alphenaar, B. W., Exciton dissociation and stark effect in the carbon nanotube photocurrent spectrum. *Nano Letters* **2008,** *8* (1), 142-146.

72. Li, Y.; Chernikov, A.; Zhang, X.; Rigosi, A.; Hill, H. M.; van der Zande, A. M.; Chenet, D. A.; Shih, E.-M.; Hone, J.; Heinz, T. F., Measurement of the optical dielectric function of monolayer transition-metal dichalcogenides: MoS 2, Mo S e 2, WS 2, and WS e 2. *Physical Review B* **2014,** *90* (20), 205422.

73. Rosenblatt, S.; Yaish, Y.; Park, J.; Gore, J.; Sazonova, V.; McEuen, P. L., High performance electrolyte gated carbon nanotube transistors. *Nano letters* **2002,** *2* (8), 869-872.

74. Ahn, Y.; Dunning, J.; Park, J., Scanning photocurrent imaging and electronic band studies in silicon nanowire field effect transistors. *Nano letters* **2005,** *5* (7), 1367-1370.

75. Freitag, M.; Tsang, J. C.; Bol, A.; Yuan, D.; Liu, J.; Avouris, P., Imaging of the Schottky barriers and charge depletion in carbon nanotube transistors. *Nano Letters* **2007,** *7* (7), 2037-2042.

76. Rhoderick, E. H., Metal-semiconductor contacts. *IEE Proceedings I-Solid-State and Electron Devices* **1982,** *129* (1), 1-14.

77. Nipane, A.; Jayanti, S.; Borah, A.; Teherani, J. T., Electrostatics of lateral pn junctions in atomically thin materials. *Journal of Applied Physics* **2017,** *122* (19), 194501.

78. Xu, X.; Yao, W.; Xiao, D.; Heinz, T. F., Spin and pseudospins in layered transition metal dichalcogenides. *Nature Physics* **2014,** *10* (5), 343.

79. Arora, A.; Koperski, M.; Nogajewski, K.; Marcus, J.; Faugeras, C.; Potemski, M., Excitonic resonances in thin films of WSe 2: from monolayer to bulk material. *Nanoscale* **2015,** *7* (23), 10421-10429.

80. Huang, J.; Hoang, T. B.; Mikkelsen, M. H., Probing the origin of excitonic states in monolayer WSe2. *Scientific reports* **2016,** *6*, 22414.

81. Lodish H, B. A., Zipursky SL, et al, *Molecular Cell Biology*. 4th edition ed.; 2000; Vol. Overview of Neuron Structure and Function; Section 21.1.

82. J. Gordon Betts, P. D., Eddie Johnson, Jody E. Johnson, Oksana Korol, Anatomy and Physiology. In *The Action Potential* [Online] OpenStax. https://opentextbc.ca/anatomyandphysiology/chapter/12-4-the-action-potential/.

83. Abrey, L. E.; Batchelor, T. T.; Ferreri, A. J.; Gospodarowicz, M.; Pulczynski, E. J.; Zucca, E.; Smith, J. R.; Korfel, A.; Soussain, C.; DeAngelis, L. M., Report of an international workshop to standardize baseline evaluation and response criteria for primary CNS lymphoma. *Journal of clinical oncology* **2005,** *23* (22), 5034-5043.

84. Iseri, P. K.; Altinas, Ö.; Tokay, T.; Yüksel, N., Relationship between cognitive impairment and retinal morphological and visual functional abnormalities in Alzheimer disease. *Journal of neuro-ophthalmology* **2006,** *26* (1), 18-24.

85. Imamura, Y.; Fujiwara, T.; Margolis, R.; Spaide, R. F., Enhanced depth imaging optical coherence tomography of the choroid in central serous chorioretinopathy. *Retina* **2009,** *29* (10), 1469-1473.

86. London, A.; Benhar, I.; Schwartz, M., The retina as a window to the brain—from eye research to CNS disorders. *Nature Reviews Neurology* **2013,** *9* (1), 44-53.

87. Fu, X.; Huu, V. A. N.; Duan, Y.; Kermany, D. S.; Valentim, C. C. S.; Zhang, R.; Zhu, J.; Zhang, C. L.; Sun, X.; Zhang, K., Clinical applications of retinal gene therapies. *Precision Clinical Medicine* **2018,** *1* (1), 5-20.

88. Wang, Y. V.; Weick, M.; Demb, J. B., Spectral and temporal sensitivity of cone-mediated responses in mouse retinal ganglion cells. *J Neurosci* **2011,** *31* (21), 7670-81.

89. Arman, A. C.; Sampath, A. P., Patch clamp recordings from mouse retinal neurons in a dark-adapted slice preparation. *J Vis Exp* **2010,** *43*, 2107.

90. Sucher, N. J.; Aizenman, E.; Lipton, S. A., N-methyl-D-aspartate antagonists prevent kainate neurotoxicity in rat retinal ganglion cells in vitro. *The Journal of Neuroscience* **1991,** *11* (4), 966-971.

91. Kitamura, K.; Judkewitz, B.; Kano, M.; Denk, W.; Häusser, M., Targeted patch-clamp recordings and single-cell electroporation of unlabeled neurons in vivo. *Nature methods* **2008,** *5* (1), 61-67.

92. Kim, S. A.; Jun, S. B., In-vivo Optical Measurement of Neural Activity in the Brain. *Exp Neurobiol* **2013,** *22* (3), 158-66.

93. Denk, W.; Detwiler, P. B., Optical recording of light-evoked calcium signals in the functionally intact retina. *Proceedings of the National Academy of Sciences* **1999,** *96* (12), 7035-7040.

94. Scanziani, M.; Häusser, M., Electrophysiology in the age of light. *Nature* **2009,** *461* (7266), 930-939.

95. Obien, M. E.; Deligkaris, K.; Bullmann, T.; Bakkum, D. J.; Frey, U., Revealing neuronal function through microelectrode array recordings. *Front Neurosci* **2014,** *8*, 423.

96. Hughes, S.; Rodgers, J.; Hickey, D.; Foster, R. G.; Peirson, S. N.; Hankins, M. W., Characterisation of light responses in the retina of mice lacking principle components of rod, cone and melanopsin phototransduction signalling pathways. *Scientific reports* **2016,** *6*, 28086.

97. Bertotti, G.; Dodel, N.; Keil, S.; Wolansky, D.; Tillak, B.; Schreiter, M.; Eickenscheidt, M.; Zeck, G.; Stett, A.; Möller, A. In *A capacitively-coupled CMOS-MEA with 4225 recording sites and 1024 stimulation sites*, Proc. of the 9th Int. Meeting on Substrate-Integrated Microelectrodes, Reutlingen, Germany, 2014.

98. Lee, S.; Jung, S. W.; Ahn, J.; Yoo, H. J.; Oh, S. J., Microelectrode array with integrated nanowire FET switches for high-resolution retinal prosthetic systems. *Journal of Micromechanics and Microengineering* **2014,** *24* (7), 075018.

99. Spira, M. E.; Hai, A., Multi-electrode array technologies for neuroscience and cardiology. *Nature Nanotechnology* **2013,** *8* (2), 83-94.

100. Dodson, K. H.; Echevarria, F. D.; Li, D.; Sappington, R. M.; Edd, J. F., Retina-on-a-chip: a microfluidic platform for point access signaling studies. *Biomedical microdevices* **2015,** *17* (6), 1-10.

101. Liu, Q.; Guo, B.; Rao, Z.; Zhang, B.; Gong, J. R., Strong two-photon-induced fluorescence from photostable, biocompatible nitrogen-doped graphene quantum dots for cellular and deep-tissue imaging. *Nano Lett* **2013,** *13* (6), 2436-41.

102. Cohen-Karni, T.; Qing, Q.; Li, Q.; Fang, Y.; Lieber, C. M., Graphene and nanowire transistors for cellular interfaces and electrical recording. *Nano Lett* **2010,** *10* (3), 1098-102.

103. Weaver, C. L.; LaRosa, J. M.; Luo, X.; Cui, X. T., Electrically controlled drug delivery from graphene oxide nanocomposite films. *ACS Nano* **2014,** *8* (2), 1834-43.

104. Sayyar, S.; Murray, E.; Thompson, B.; Chung, J.; Officer, D. L., Processable conducting graphene-chitosan hydrogels for tissue engineering. *Journal of Materials Chemistry* **2015,** *3* (3), 481-490.

105. Veliev, F.; Briancon-Marjollet, A.; Bouchiat, V.; Delacour, C., Impact of crystalline quality on neuronal affinity of pristine graphene. *Biomaterials* **2016,** *86*, 33-41.

106. He, Z.; Zhang, S.; Song, Q.; Li, W.; Liu, D.; Li, H.; Tang, M.; Chai, R., The structural development of primary cultured hippocampal neurons on a graphene substrate. *Colloids Surf B Biointerfaces* **2016,** *146*, 442-51.

107. Lee, J. S.; Lipatov, A.; Ha, L.; Shekhirev, M.; Andalib, M. N.; Sinitskii, A.; Lim, J. Y., Graphene substrate for inducing neurite outgrowth. *Biochem Biophys Res Commun* **2015,** *460* (2), 267-73.

108. Fabbro, A.; Scaini, D.; Leon, V.; Vazquez, E.; Cellot, G.; Privitera, G.; Lombardi, L.; Torrisi, F.; Tomarchio, F.; Bonaccorso, F.; Bosi, S.; Ferrari, A. C.; Ballerini, L.; Prato, M., Graphene-Based Interfaces Do Not Alter Target Nerve Cells. *ACS Nano* **2016,** *10* (1), 615-23.

109. Bendali, A.; Hess, L. H.; Seifert, M.; Forster, V.; Stephan, A. F.; Garrido, J. A.; Picaud, S., Purified neurons can survive on peptide-free graphene layers. *Adv Healthc Mater* **2013,** *2* (7), 929-33.

110. Sahni, D.; Jea, A.; Mata, J. A.; Marcano, D. C.; Sivaganesan, A.; Berlin, J. M.; Tatsui, C. E.; Sun, Z.; Luerssen, T. G.; Meng, S.; Kent, T. A.; Tour, J. M., Biocompatibility of pristine graphene for neuronal interface. *J Neurosurg Pediatr* **2013,** *11* (5), 575-83.

111. Park, H.-B., Effect of Graphene on Growth of Neuroblastoma Cells. *Journal of Microbiology and Biotechnology* **2013,** *23* (2), 274-277.

112. Li, N.; Zhang, X.; Song, Q.; Su, R.; Zhang, Q.; Kong, T.; Liu, L.; Jin, G.; Tang, M.; Cheng, G., The promotion of neurite sprouting and outgrowth of mouse hippocampal cells in culture by graphene substrates. *Biomaterials* **2011,** *32* (35), 9374-82.

113. Park, D. W.; Brodnick, S. K.; Ness, J. P.; Atry, F.; Krugner-Higby, L.; Sandberg, A.; Mikael, S.; Richner, T. J.; Novello, J.; Kim, H.; Baek, D. H.; Bong, J.; Frye, S. T.; Thongpang, S.; Swanson, K. I.; Lake, W.; Pashaie, R.; Williams, J. C.; Ma, Z., Fabrication and utility of a transparent graphene neural electrode array for electrophysiology, in vivo imaging, and optogenetics. *Nat Protoc* **2016,** *11* (11), 2201-2222.

114. Sappington, R. M.; Sidorova, T.; Ward, N. J.; Chakravarthy, R.; Ho, K. W.; Calkins, D. J., Activation of transient receptor potential vanilloid-1 (TRPV1) influences how retinal ganglion cell neurons respond to pressure-related stress. *Channels (Austin)* **2015,** *9* (2), 102-13.

115. Lee, S. J.; Duncan, D. S.; Echevarria, F. D.; McLaughlin, W. M.; Hatcher, J. B.; Sappington, R. M., Pressure-Induced Alterations in PEDF and PEDF-R Expression: Implications for Neuroprotective Signaling in Glaucoma. *J Clin Exp Ophthalmol* **2015,** *6* (5).

116. Sappington, R. M.; Calkins, D. J., Pressure-Induced Regulation of IL-6 in Retinal Glial Cells: Involvement of the Ubiquitin/Proteasome Pathway and NF B. *IOVS* **2006,** *47* (9), 3860-3869.

117. Sappington, R. M.; Sidorova, T.; Long, D. J.; Calkins, D. J., TRPV1: contribution to retinal ganglion cell apoptosis and increased intracellular Ca2+ with exposure to hydrostatic pressure. *Invest Ophthalmol Vis Sci* **2009,** *50* (2), 717-28.

118. Meyer-Franke, A.; Kaplan, M. R.; Pfreiger, F. W.; Barres, B. A., Characterization of the Signaling Interactions That Promote the Survival and Growth of Developing Retinal Ganglion Cells in Culture. *Neuron* **1995,** *15*, 805-819.

119. Chen, Q.; Kinch, M. S.; Lin, T. H.; Burridge, K.; Juliano, R. L., Integrin-mediated Cell Adhesion Activates Mitogen-activated Protein Kinases. *The Journal of Biological Chemistry* **1994,** *269* (43), 26602-26605.

120. Kuhn, T. B.; Brown, M. D.; Bamburg, J. R., Rac1-dependent actin filament organization in growth cones is necessary for ?1-integrin-mediated advance but not for growth on poly-D-lysine. *Journal of Neurobiology* **1998,** *37* (4), 524-540.

121. Smalheiser, N. R.; Crain, S. M.; Reid, L. M., Laminin as a substrate for retinal axons in vitro. *Developmental Brain Reserach* **1984,** *12*, 136-140.

122. Cohen, J.; Burne, J. F.; McKinlay, C.; Winter, J., The Role of Laminin and the Laminin/Fibronectin Receptor Complex in the Outgrowth of Retinal Ganglion Cell Axons. *Developmental Biology* **1987,** *122*, 407-418.

123. Cohen, J.; Johnson, A. R., Differential effects of laminin and merosin on neurite outgrowth by developing retinal ganglion cells. *Journal of Cell Science* **1991,** *15*, 1-7.

124. Sappington, R. M.; Chan, M.; Calkins, D. J., Interleukin-6 protects retinal ganglion cells from pressure-induced death. *Invest Ophthalmol Vis Sci* **2006,** *47* (7), 2932-42.

125. Legrand, O.; Simonin, G.; Perrot, J.-Y.; Zittoun, R.; Marie, J.-P., Pgp and MRP Activities Using Calcein-AM Are Prognostic Factors in Adult Acute Myeloid Leukemia Patients. *Blood* **1998,** *91* (12), 4480-4488.

126. Poole, C. A.; Brookes, N. H.; Gilbert, R. T.; Beaumont, B. W.; Crowther, A.; Scott, L.; Merrilees, M. J., Detection of Viable and Non-Viable Cells in Connective Tissue Explants Using the Fixable Fluoroprobes 5-Chloromethylfluorescein Diacetate and Ethidium Homodimer-1. *Connective Tissue Research* **2009,** *33* (4), 233-241.

127. Chen, S.; Nilsen, J.; Brinton, R. D., Dose and temporal pattern of estrogen exposure determines neuroprotective outcome in hippocampal neurons: therapeutic implications. *Endocrinology* **2006,** *147* (11), 5303-13.

128. Grieshaber, P.; Lagreze, W. A.; Noack, C.; Boehringer, D.; Biermann, J., Staining of fluorogold-prelabeled retinal ganglion cells with calcein-AM: A new method for assessing cell vitality. *J Neurosci Methods* **2010,** *192* (2), 233-9.

129. Crish, S. D.; Calkins, D. J., Neurodegeneration in glaucoma: progression and calcium-dependent intracellular mechanisms. *Neuroscience* **2011,** *176*, 1-11.

130. Formichella, C. R.; Abella, S. K.; Sims, S. M.; Cathcart, H. M.; Sappington, R. M., Astrocyte Reactivity: A Biomarker for Retinal Ganglion Cell Health in Retinal Neurodegeneration. *J Clin Cell Immunol* **2014,** *5* (1).

131. Crish, S. D.; Dapper, J. D.; MacNamee, S. E.; Balaram, P.; Sidorova, T. N.; Lambert, W. S.; Calkins, D. J., Failure of axonal transport induces a spatially coincident increase in astrocyte BDNF prior to synapse loss in a central target. *Neuroscience* **2013,** *229*, 55-70.

132. Crish, S. D.; Sappington, R. M.; Inman, D. M.; Horner, P. J.; Calkins, D. J., Distal axonopathy with structural persistence in glaucomatous neurodegeneration. *PNAS* **2010,** *107*, 5196-5201.

133. Echevarria, F. D.; Walker, C. C.; Abella, S. K.; Won, M.; Sappington, R. M., Stressor-dependent Alterations in Glycoprotein 130: Implications for Glial Cell Reactivity, Cytokine Signaling and Ganglion Cell Health in Glaucoma. *J Clin Exp Ophthalmol* **2013,** *4* (3).

134. Kalil, K.; Dent, E. W., Branch management: mechanisms of axon branching in the developing vertebrate CNS. *Nat Rev Neurosci* **2014,** *15* (1), 7-18.

135. Weaver, C. D.; Harden, D.; Dworetzky, S. I.; Robertson, B.; Knox, R. J., A thallium-sensitive, fluorescence-based assay for detecting and characterizing potassium channel modulators in mammalian cells. *J Biomol Screen* **2004,** *9* (8), 671-7.

136. Kitko, K. E.; Hong, T.; Lazarenko, R. M.; Ying, D.; Xu, Y.-Q.; Zhang, Q., Membrane cholesterol mediates the cellular effects of monolayer graphene substrates. *Nature Communications* **2018,** *9* (1), 796.

137. Abrahamson, E. E.; Moore, R. Y., Suprachiasmatic nucleus in the mouse: retinal innervation, intrinsic organization and efferent projections. *Brain research* **2001,** *916* (1), 172-191.

138. Govardovskii, V. I.; FYHRQUIST, N.; Reuter, T.; KUZMIN, D. G.; DONNER, K., In search of the visual pigment template. *Visual neuroscience* **2000,** *17* (04), 509-528.

139. Mueller, T.; Xia, F.; Freitag, M.; Tsang, J.; Avouris, P., Role of contacts in graphene transistors: A scanning photocurrent study. *Physical Review B* **2009,** *79* (24), 245430.

140. Largeot, C.; Portet, C.; Chmiola, J.; Taberna, P.-L.; Gogotsi, Y.; Simon, P., Relation between the ion size and pore size for an electric double-layer capacitor. *Journal of the American Chemical Society* **2008,** *130* (9), 2730-2731.

141. von Bartheld, C. S.; Bahney, J.; Herculano-Houzel, S., The search for true numbers of neurons and glial cells in the human brain: A review of 150 years of cell counting. *Journal of Comparative Neurology* **2016,** *524* (18), 3865-3895.

142. Papouin, T.; Haydon, P. G., Obtaining Acute Brain Slices. *Bio-protocol* **2018,** *8* (2), e2699.

143. Miller, S. J.; Philips, T.; Kim, N.; Dastgheyb, R.; Chen, Z.; Hsieh, Y.-C.; Daigle, J. G.; Datta, M.; Chew, J.; Vidensky, S.; Pham, J. T.; Hughes, E. G.; Robinson, M. B.; Sattler, R.; Tomer, R.; Suk, J. S.; Bergles, D. E.; Haughey, N.; Pletnikov, M.; Hanes, J.; Rothstein, J. D., Molecularly defined cortical astroglia subpopulation modulates neurons via secretion of Norrin. *Nature Neuroscience* **2019,** *22* (5), 741-752.

144. Styr, B.; Gonen, N.; Zarhin, D.; Ruggiero, A.; Atsmon, R.; Gazit, N.; Braun, G.; Frere, S.; Vertkin, I.; Shapira, I.; Harel, M.; Heim, L. R.; Katsenelson, M.; Rechnitz, O.; Fadila, S.; Derdikman, D.; Rubinstein, M.; Geiger, T.; Ruppin, E.; Slutsky, I., Mitochondrial Regulation of the Hippocampal Firing Rate Set Point and Seizure Susceptibility. *Neuron* **2019,** *102* (5), 1009-1024.e8.

145. Negahbani, E.; Schmidt, S. L.; Mishal, N.; Fröhlich, F., Neuromodulation-dependent effect of gated high-frequency, LFMS-like electric field stimulation in mouse cortical slices. *European Journal of Neuroscience* **2019,** *49* (10), 1288-1297.

146. Soscia, D. A.; Lam, D.; Tooker, A. C.; Enright, H. A.; Triplett, M.; Karande, P.; Peters, S. K. G.; Sales, A. P.; Wheeler, E. K.; Fischer, N. O., A flexible 3-dimensional microelectrode array for in vitro brain models. *Lab on a Chip* **2020,** *20* (5), 901-911.

147. Ito, D.; Komatsu, T.; Gohara, K., Measurement of saturation processes in glutamatergic and GABAergic synapse densities during long-term development of cultured rat cortical networks. *Brain research* **2013,** *1534*, 22-32.

148. Park, D.-W.; Schendel, A. A.; Mikael, S.; Brodnick, S. K.; Richner, T. J.; Ness, J. P.; Hayat, M. R.; Atry, F.; Frye, S. T.; Pashaie, R.; Thongpang, S.; Ma, Z.; Williams, J. C., Graphene-based carbon-layered electrode array technology for neural imaging and optogenetic applications. *Nature Communications* **2014,** *5* (1), 5258.

149. Metallo, C.; White, R. D.; Trimmer, B. A., Flexible parylene-based microelectrode arrays for high resolution EMG recordings in freely moving small animals. *Journal of neuroscience methods* **2011,** *195* (2), 176-184.

150. Rousche, P. J.; Pellinen, D. S.; Pivin, D. P.; Williams, J. C.; Vetter, R. J.; Kipke, D. R., Flexible polyimide-based intracortical electrode arrays with bioactive capability. *IEEE transactions on biomedical engineering* **2001,** *48* (3), 361-371.

151. Buzsáki, G., Large-scale recording of neuronal ensembles. *Nature Neuroscience* **2004,** *7* (5), 446-451.

152. Wise, K. D.; Angell, J. B., A Low-Capacitance Multielectrode Probe for Use in Extracellular Neurophysiology. *IEEE transactions on biomedical engineering* **1975,** *BME-22* (3), 212-219.

153. Suner, S.; Fellows, M. R.; Vargas-Irwin, C.; Nakata, G. K.; Donoghue, J. P., Reliability of signals from a chronically implanted, silicon-based electrode array in non-human primate primary motor cortex. *IEEE Transactions on Neural Systems and Rehabilitation Engineering* **2005,** *13* (4), 524-541.

154. Stieglitz, T.; Schuetter, M.; Koch, K. P., Implantable biomedical microsystems for neural prostheses. *IEEE Engineering in Medicine and Biology Magazine* **2005,** *24* (5), 58-65.

155. Cheung, K. C., Implantable microscale neural interfaces. *Biomedical Microdevices* **2007,** *9* (6), 923-938.

156. Abeles, M., *Corticonics: Neural circuits of the cerebral cortex*. Cambridge University Press: 1991.

157. Kang, J.; Son, D.; Wang, G.-J. N.; Liu, Y.; Lopez, J.; Kim, Y.; Oh, J. Y.; Katsumata, T.; Mun, J.; Lee, Y.; Jin, L.; Tok, J. B.-H.; Bao, Z., Tough and Water-Insensitive Self-Healing Elastomer for Robust Electronic Skin. *Advanced Materials* **2018,** *30* (13), 1706846.

158. Minev, I. R.; Musienko, P.; Hirsch, A.; Barraud, Q.; Wenger, N.; Moraud, E. M.; Gandar, J.; Capogrosso, M.; Milekovic, T.; Asboth, L.; Torres, R. F.; Vachicouras, N.; Liu, Q.; Pavlova, N.; Duis, S.; Larmagnac, A.; Vörös, J.; Micera, S.; Suo, Z.; Courtine, G.; Lacour, S. P., Electronic dura mater for long-term multimodal neural interfaces. *Science* **2015,** *347* (6218), 159-163.

159. Kim, J.; Lee, M.; Shim, H. J.; Ghaffari, R.; Cho, H. R.; Son, D.; Jung, Y. H.; Soh, M.; Choi, C.; Jung, S.; Chu, K.; Jeon, D.; Lee, S.-T.; Kim, J. H.; Choi, S. H.; Hyeon, T.; Kim, D.-H., Stretchable silicon nanoribbon electronics for skin prosthesis. *Nature Communications* **2014,** *5* (1), 5747.

160. Shintake, J.; Rosset, S.; Schubert, B.; Floreano, D.; Shea, H., Versatile Soft Grippers with Intrinsic Electroadhesion Based on Multifunctional Polymer Actuators. *Advanced Materials* **2016,** *28* (2), 231-238.

161. Christianson, C.; Goldberg, N. N.; Deheyn, D. D.; Cai, S.; Tolley, M. T., Translucent soft robots driven by frameless fluid electrode dielectric elastomer actuators. *Science Robotics* **2018,** *3* (17), eaat1893.

162. Fang, H.; Yu, K. J.; Gloschat, C.; Yang, Z.; Song, E.; Chiang, C.-H.; Zhao, J.; Won, S. M.; Xu, S.; Trumpis, M.; Zhong, Y.; Han, S. W.; Xue, Y.; Xu, D.; Choi, S. W.; Cauwenberghs, G.; Kay, M.; Huang, Y.; Viventi, J.; Efimov, I. R.; Rogers, J. A., Capacitively coupled arrays of multiplexed flexible silicon transistors for long-term cardiac electrophysiology. *Nature Biomedical Engineering* **2017,** *1* (3), 0038.

163. Hess, L. H.; Seifert, M.; Garrido, J. A., Graphene Transistors for Bioelectronics. *Proceedings of the IEEE* **2013,** *101* (7), 1780-1792.

164. Kostarelos, K.; Vincent, M.; Hebert, C.; Garrido, J. A., Graphene in the Design and Engineering of Next-Generation Neural Interfaces. *Advanced Materials* **2017,** *29* (42), 1700909.

165. Rountree, C. M.; Inayat, S.; Troy, J. B.; Saggere, L., Differential stimulation of the retina with subretinally injected exogenous neurotransmitter: A biomimetic alternative to electrical stimulation. *Scientific Reports* **2016,** *6* (1), 38505.

166. Tengölics, Á. J.; Szarka, G.; Ganczer, A.; Szabó-Meleg, E.; Nyitrai, M.; Kovács-Öller, T.; Völgyi, B., Response Latency Tuning by Retinal Circuits Modulates Signal Efficiency. *Scientific Reports* **2019,** *9* (1), 15110.

167. Xia, J. L.; Chen, F.; Li, J. H.; Tao, N. J., Measurement of the quantum capacitance of graphene. *Nature Nanotechnology* **2009,** *4* (8), 505-509.

168. Randin, J. P.; Yeager, E., Differential Capacitance Study of Stress/Annealed Pyrolytic Graphite Electrodes. *Journal of the Electrochemical Society* **1971,** *118* (5), 711-&.